Satellite cloud property retrievals for climate studies
using synergistic AATSR and MERIS measurements

Cintia Carbajal Henken

Satellite cloud property retrievals for climate studies

using synergistic AATSR and MERIS measurements

Freie Universität Berlin

vorgelegt von

Cintia Karin Carbajal Henken

Berlin, Januar 2015

Cover: MERIS observations (channel 10) of clouds for 20 June 2008.

Satellite cloud property retrievals for climate studies

using synergistic AATSR and MERIS measurements

Cintia Karin Carbajal Henken

Erstgutachter: Prof. Dr. Jürgen Fischer (Freie Universität Berlin)

Zweitgutachter: Prof. Dr. Ralf Bennartz (Vanderbilt University)

Tag der Disputation: 10 Februar 2015

Selbstständigkeitserklärung

Hiermit erkläre ich an Eides Statt, das ich die vorliegende Arbeit selbständig und ohne fremde Hilfe angefertigt, keine anderen als die angegebenen Quellen und Hilfsmittel benutzt und die den benutzen Quellen wörtlich oder inhaltlich entnommenen Stellen als solche kenntlich gemacht habe. Diese Arbeit hat in gleicher oder ähnlicher Form noch keiner Prüfungsbehörde vorgelegen.

Berlin, 10.01.2015

Las nubes gordas de un gris de rata
y de un púrpura encrespado,
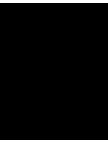*hacían rizos en el cielo*
en forma de lemniscata.

Noel Carbajal

For my family

Contents

xii

CHAPTER **1**

Introduction

Weather affects human activities on a daily basis. Climate, the prevailing weather over time for a specific region, has enduring effects on human civilizations. There are a number of indications that climate change has and will have serious implications on aspects such as accessibility of water and food, global health and safety, and diversity of eco-systems. If one cares about at least one of these topics, then understanding and monitoring climate change and its implications are of crucial importance. A genuine curiosity in understanding the world we live in, our Earth and its atmosphere, is a good start.

1.1 The role of clouds in the energy balance of the Earth

On average, about 70% of the Earth's surface is covered by clouds (Stubenrauch et al., 2012). Clouds affect the Earth's energy balance by inducing changes to the shortwave and longwave radiation. On the one hand, they can reflect a significant amount of the incoming shortwave radiation back to space, decreasing the amount of shortwave radiation absorbed by the earth-atmosphere system. On the other hand, they emit longwave radiation to space and modulate the longwave radiation emitted by the earth-atmosphere system.

A recent estimate of the global annual mean energy budget of the Earth for the time period 2000-2010, is shown in Fig. 1.1. The top-of-atmosphere (TOA) fluxes are mainly compiled from observations of the Clouds and the Earth's Radiant Energy System (CERES) space-born broad scanning radiometers (Wielicki et al., 1996). The global mean net flux at TOA is estimated at
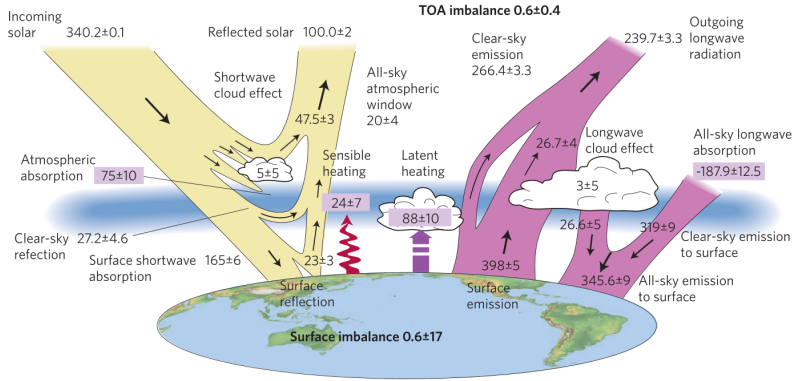
Figure 1.1: The Earth's energy balance in light of the latest global observations (Stephens at al., 2012)

0.6 W/m^2, with an uncertainty of ±0.4 W/m^2 when constrained by the best estimate of ocean heat content observations. The uncertainty on the net TOA flux determined from CERES is 4 W/m^2, arising mostly from instrument calibration errors. From Fig. 1.1 it can be seen that clouds enhance the reflected incoming solar radiation by approximately 47.5 ±3 W/m^2. This is the so called cloud albedo effect. Clouds reduce the outgoing longwave radiation by approximately 26.7 ±4 W/m^2 , with respect to clear-sky conditions. The thermal radiation emitted by the Earth is absorbed by clouds and re-emitted at colder temperatures, reducing the outgoing longwave flux. This is the so called greenhouse effect of clouds. Combined, the shortwave and longwave cloud effects result in a net negative radiative flux at the top-of-atmosphere due to clouds of approximately 21.1 ±5 W/m^2. Thus, the overall impact of clouds on the Earth's energy balance is to cool the earth-atmosphere system. The main contributor to this cooling effect are the clouds in the mid-latitude summer hemisphere that reflect large amounts of incident solar radiation (Harrison et al., 1990).

The effect of clouds on the Earth's energy balance is referred to as the cloud radiative forcing (CRF) or cloud radiative effect (CRE), which is defined as the difference between all-sky and clear-sky radiative fluxes. This quantity is used in many studies to estimate the radiative impact of clouds. Ramanathan et al. (1989) made quantitative estimates of global distributions of the cloud radiative forcing at TOA using observations from the space-born Earth Radiation Budget Experiment (ERBE), launched in 1984, the precursor to the CERES instruments. In Loeb et al. (2009) the global mean net CRE computed from various satellite-based data products and methods is

compared and the values vary within a range from -16.7 to -24.5 W/m^2.

The spatial and temporal variation of (TOA) net cloud radiative forcing is related to large-scale meteorological conditions, which is closely coupled to the occurrence of clouds, i.e., cloud fraction, but also depends on the cloud type. The sign of the net radiative forcing in a cloudy atmosphere is dominated by the vertical distribution of the clouds (Mace et al., 2006). Low-level clouds (optically thick boundary clouds) tend to be relatively warm, the temperature of the cloud droplet is similar to the temperature of the Earth's surface, and therefore hardly affecting the outgoing longwave flux. However, these clouds tend to have large albedos, which results in a cooling effect in the lower troposphere. High-level clouds are much colder than the Earth's surface and lower troposphere, therefore reducing the outgoing longwave flux. In addition, they are often optically thin, thus not reflecting much of the incident solar radiation. Therefore, they tend to heat the upper troposphere.

1.2 The role of clouds in a changing climate

In 2013, the Intergovernmental Panel on Climate Change (IPCC) Fifth Assessment Report (AR5) was published. The *Summary for policy makers* lists the certainty of key findings in the assessment. In section (B) *Observed Changes in the Climate System* it is stated:

> Warming of the climate system is unequivocal, and since the 1950s, many of the observed changes are unprecedented over decades to millennia. The atmosphere and ocean have warmed, the amounts of snow and ice have diminished, sea level has risen, and the concentrations of greenhouse gases have increased.

The global warming, mainly due to an increase of CO_2 concentrations in the atmosphere, is expected to change the spatial and temporal distribution of clouds and the type of clouds. Global changes in cloud amount or in the distribution of cloud types could have large effects on the Earth's energy balance and thus climate. The question is how clouds change in a changing climate, i.e., what are the cloud-climate feedbacks, and what is the sign of the overall feedback; negative, reducing global warming, or positive, enhancing global warming. Cloud radiative feedback is defined as the impact on the TOA net downward radiative flux per degree of global surface temperature increase (IPCC). Here, positive values are assigned to positive feedbacks.

Clouds are closely coupled to the large-scale meteorology and play an important role in the hydrological cycle. Therefore, also changes in the amount and distribution of water vapor will affect the formation of clouds and their properties. In section (D) *Understanding the Climate System and its Recent Changes* of the *Summary for policy makers* it is stated:

> The net feedback from the combined effect of changes in water vapor, and differences between atmospheric and surface warming is extremely likely positive and therefore amplifies changes in climate. The net radiative feedback due to all cloud types combined is likely positive. Uncertainty in the sign and magnitude of the cloud feedback is due primarily to continuing uncertainty in the impact of warming on low clouds.

The large amount of reflected solar radiation by low-level clouds is of particular interest in understanding cloud-climate feedbacks. From combined use of observations and climate models, Clement et al. (2009) found that low-level stratiform clouds over the northeast Pacific Ocean appear to dissipate as the ocean warms. As these large cloud fields strongly reflect the solar radiation, dissipation of these clouds could enhance the warming of the Earth, which in turn could lead to even more dissipation of the clouds. This behavior was not reproduced by most global climate models. Other examples of positive feedback, though with large uncertainties, found in model simulations in both cloud resolving models (Harrop and Hartmann, 2012) as well as general circulation models (Zelinka and Hartmann, 2010) and satellite observations (Eitzen et al., 2009), are due to an increase in altitude of high clouds accompanied with just small increases in cloud top temperature, which trap more infrared radiation. Also, a shift of cloudy storm tracks towards the poles was found, which decreases the amount of reflected solar radiation, and also observed from satellite observations (Bender et al., 2012).

Dessler (2010) estimated the overall short-term cloud feedback from a ten year period of satellite observations likely to be positive. From climate models, taking into consideration additional uncertainties that were not accounted for in the models, the cloud feedback from all cloud types is estimated to be within a range of -0.2 to +2.0 W/m^2/C° (Boucher et al., 2013).

Figure 1.2, taken from section (C) *Drivers of Climate Change* of the *Summary for policy makers*, shows the radiative forcing estimates in 2011 relative to 1750 for emitted atmospheric constituents or processes that result in the main drivers of climate change. In this section it is stated:

The RF of the total aerosol effect in the atmosphere, which includes cloud adjustments due to aerosols, is –0.9 [–1.9 to –0.1] W m^{-2} (medium confidence), and results from a negative forcing from most aerosols and a positive contribution from black carbon absorption of solar radiation. There is high confidence that aerosols and their interactions with clouds have offset a substantial portion of global mean forcing from well-mixed greenhouse gases. They continue to contribute the largest uncertainty to the total RF estimate.

Emissions of anthropogenic aerosols induce changes to the cloud properties due to aerosol-cloud interactions. Aerosols serve as cloud condensation nuclei. An increased number of aerosols can adjust the cloud droplet distribution by decreasing the size of the droplets and increasing the number of the droplets. This will change the radiative properties of a cloud. An increase in the cloud albedo is called the indirect effect (Twomey, 1977). Second indirect effects are an increase in the cloud amount (Pincus and Baker, 1994), mostly described in terms of development of precipitation, cloud liquid water path and cloud life time.

1.3 Clouds in climate models

The horizontal resolution of climate models is in the order of 100 km, while the vertical resolution is in the order of 100 m. Within these horizontal scales, clouds can show large variabilities in their properties due to variabilities in the state of the atmosphere (e.g. temperature and water vapor profiles). The cloud process in the models are sub-grid processes an thus not resolved. The cloud processes are parameterized in terms of predicted model variables such as temperature and humidity.

In section (D) *Understanding the Climate System and its Recent Changes* of the *Summary for policy makers* it is stated:

Climate models now include more cloud and aerosol processes, and their interactions, than at the time of the AR4, but there remains low confidence in the representation and quantification of these processes in models.

Since decades it is known that the representation of cloud processes in climate models form a dominant source of uncertainty in understanding and modeling climate change (Arakawa, 1975; Randall et al., 2003).
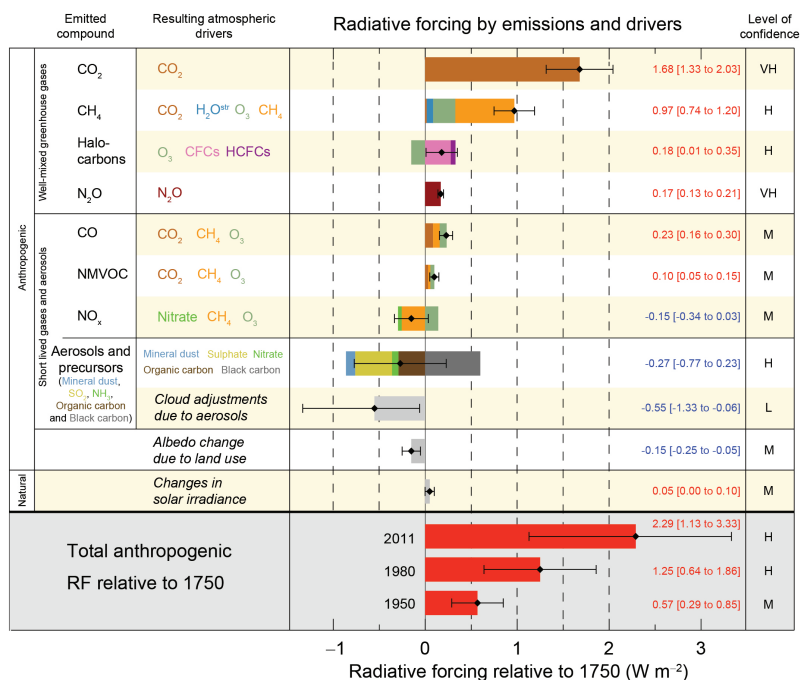
Figure 1.2: IPCC radiative forcing table from AR5 (2012): Radiative forcing estimates in 2011 relative to 1750 and their uncertainties for the main drives of climate change.

A number of studies have been conducted comparing cloud radiative forcing at the top-of-atmosphere from atmospheric general circulation models models with ERBE observations (e.g. Cess et al., 1997). Potter and Cess (2004) found that agreements between regionally averaged cloud radiative forcing from a set of atmospheric general circulation models and ERBE observations is partly the result of compensating errors in cloud vertical structure, cloud optical thickness or cloud fraction.

Most climate models show a positive cloud feedback. However, the differences in cloud feedbacks in the models still is the main source of the spread between climate model projections (IPCC). A review on the reasons of the lack of understanding of cloud-climate feedbacks is given in Stephens (2005). It is stated that one of the reasons is the parameterization of cloud process in climate models and their limited evaluation. Among the reasons to expect progress in the near-future is mentioned the availability of improved global data sets from satellite observations for evaluation of cloud

parameterizations.

For accurate estimations of the cloud radiative forcing and changes in the cloud radiative forcing due to climate change, the climate models should be able to reproduce the observed characteristics and distribution of clouds and their associated radiative fluxes (Webb et al., 2001), as well as their diurnal, seasonal and inter-annual variations.

1.4   Satellite remote sensing of clouds

To improve our understanding of cloud-climate interactions as well as for climate monitoring and data assimilation in climate models and numerical weather prediction models, accurate observations of clouds on a global scale are required. Observations from remote sensing instruments on polar orbiting satellites can provide a global coverage within several days and with the same instrument. This also allows for measurements in remote areas with low temporal and spatial coverage by ground-based observations or in-situ measurements. Further, a number of satellite missions provide long-term cloud observations, allowing for the development of consistent climate records of cloud properties, cloud climatologies, necessary to observe any climate trends occurring in the cloud properties.

Since the launch of the first meteorological satellite Television Infrared Observation Satellite (TIROS-1) in 1960 and beginning of operation in 1962, continuous observations of clouds from space have been made. Clapp (1964) used TIROS IV to VI photographs through TIROS nephanalyses to produce manually estimated cloud amounts, with the intention to assist in climate modeling. It was acknowledged by Clapp that the manual classification of cloud photographs will be replaced by automatic interpretation of radiation measurements in several instrument channels. Arking (1964) proposed a method to automatically derive latitudinal distribution cloud cover through the analysis of TIROS III photographs. The estimations of the global cloud cover and the TIROS III radiation measurements in the thermal infrared were used by Rasool (1964) to estimate the daytime latitudinal distribution of cloud heights for several months in the year 1961. Follow-up satellite missions of TIROS, carrying the Advanced Very High Resolution Radiometer (AVHRR) with 4 channels, are the TIROS Next-generation National Oceanic and Atmospheric Administration (TIROS-N/NOAA) and MetOp.

In the light of the increasing quality of satellite measurements as well as improved cloud property retrievals from measured radiances the following couple of decades, the International Satellite Cloud Climatology Project (ISCCP) was established in 1982 as the first project of the World Climate

Research Program (WCRP) (Rossow and Schiffer, 1991). The aim of the project is to collect and analyze global and uniformly calibrated satellite radiances to infer global distributions of cloud properties, such as cloud amount, cloud optical thickness, cloud top temperature and cloud top pressure, in order to improve the modeling of cloud effects on climate. The first cloud data products were released in 1988 (Rossow and Schiffer, 1991). It now provides the longest record of cloud properties from satellite measurements on a global scale, gridded, and with diurnal, seasonal and interannual variations. The data was collected from two polar orbiting satellites and five geostationary satellites.

Many of the satellites that have been launched in the last decades carry multi-spectral imaging radiometers, which measure the reflected, scattered and emitted radiation from clouds as well as the Earth's surface and the atmosphere. Imaging radiometers on polar orbiting satellites that are used for cloud property retrievals are, e.g., the Polarization and Directionality of the Earth's Reflectance (POLDER) (Deschamps et al., 1994), with the advantage of measuring radiances in the visible for nine different views, and the Moderate Resolution Imaging Spectroradiometer (MODIS) (Justice et al., 1998) with more than 30 channels ranging from the visible to the thermal infrared. The first American geostationary satellite was launched in 1966, the Applications Technology Satellite (ATS), with follow-up mission Geostationary Operational Environmental Satellite (GOES), and the European MeteoSat series (Schmetz et al., 2002), carrying the Spinning Enhanced Visible and Infrared Imager (SEVIRI). In contrast to observations of polar orbiting satellites, the geostationary satellites provide for observations with a high temporal resolution, allowing to resolve the daily cycle of cloud properties, though they only observe a part of the globe and mostly at lower spatial resolutions.

To retrieve cloud properties from satellite observations, the measured radiances need to be related to cloud properties, which often starts with a cloud detection method on a pixel basis. In the visible part of the spectrum, clouds often appear bright and white, thus showing a higher reflectance than the underlying surface. In the thermal infrared part of the spectrum clouds often appear colder than the underlying surface due to the emission of radiation at lower temperatures, see Fig. 1.3. These relations are complicated in many situations, e.g., snow and ice surfaces which are highly reflecting and cold. Cloud detection methods are sensitive to instrument characteristics, such as the spectral channels, signal-to-noise ratio, and the spatial resolution. Next, inversion techniques are used to relate the measured radiances for pixels identified as cloudy to a set of cloud properties. The main cloud properties retrieved from satellite measurements and their
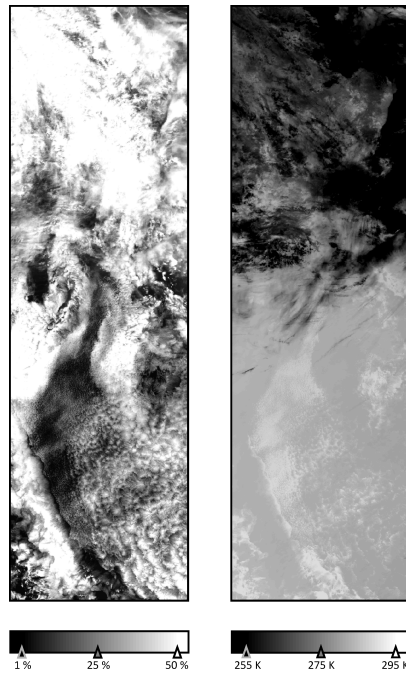
Figure 1.3: AATSR cloud observations for 20 June 2008. *Left:* Reflectances measured in channel 0.67 μm. *Right:* Brightness temperatures measured in channel 10.8 μm

definitions are:

- cloud cover

- cloud top height/temperature/pressure

- cloud thermodynamic phase

- cloud water path

- cloud optical thickness

- cloud effective radius

In the past decade the first space-born aerosol and cloud radar and lidar instruments, the Cloud Profiling Radar (CPR) CloudSat (Stephens et al.,

2002) and CALIOP (Cloud-Aerosol Lidar with Orthogonal Polarization) on-board CALIPSO (Cloud-Aerosol Lidar and Infrared Pathfinder Satellite Observations) (Winker et al., 2003), both satellite missions are part of the Afternoon Train (A-train) satellite constellation, have complemented the established observations by providing observations on the vertical structure of clouds (as well as aerosols and precipitation).

1.5 Thesis outline

The main aim of this thesis is to develop and evaluate a method for the retrieval of daytime cloud macro-physical, optical and micro-physical properties from synergistic AATSR and MERIS observations for the use of climate studies: the *FAME-C* (Freie Universität Berlin AATSR MERIS Cloud) algorithm. AATSR and MERIS are two multi-spectral imaging radiometers on-board the Environmental Satellite (Envisat). The measurements from the morning overpasses of Envisat are used in the retrieval to create a 10-year day-time cloud climatology. The work was partly done within the frame of the ESA (European Space Agency) Climate Change Initiative (CCI) Cloud project, which aims to generate consistent and accurate long-term cloud climatologies for climate studies (Hollmann et al., 2013).

Although AATSR and MERIS are primarily designed for the remote sensing of sea surface temperature and ocean color, respectively, the use of combined information of both instruments allows for the retrieval of a set of cloud properties. The synergistic approach comprises collocating AATSR and MERIS observations, and a cloud detection method and cloud property retrieval which exploit measurements from both instruments.

From AATSR reflectances at non-absorbing visible and at moderately absorbing near-infrared wavelengths, the cloud optical thickness and effective radius are retrieved based on (Nakajima and King, 1990). The implementation of this method in FAME-C largely follows the approach of Walther and Heidinger (2012). In addition, AATSR brightness temperatures at thermal infrared wavelengths are used to retrieve cloud top temperature. The main additional value of the MERIS instrument in this work lies in the use of measurements in the oxygen-A absorption band. Due to its sensitivity to the cloud top pressure, the ratio of the radiances at the oxygen-A absorption band and a near-by window channel allows for an additional and independent cloud height retrieval. Moreover, the use of the oxygen-A absorption channel in the cloud detection method and the high spectral and radiometric resolution of the MERIS channels allow for an increase in the cloud detection accuracy (Gómez-Chova et al., 2010). Compared to operational single-sensor cloud detection algorithms for MERIS and AATSR, the

synergistic cloud detection method has a higher accuracy and performs well for difficult cloudy scenes, such as snow and ice surfaces and sun-glint in the ocean. Both cloud height products can be converted to cloud top heights with the use of atmospheric profiles from numerical weather prediction data.

The gain of having two independent cloud height retrievals is presented in an evaluation study, which demonstrates the strengths and weaknesses of each method under different cloudy conditions. Further, the difference in sensitivity to the cloud vertical profile is studied with the use of both radiative transfer simulations and measurements.

With the newly developed algorithm a multi-annual dataset on a global scale was built and compared to cloud properties retrieved from other satellite instruments as well as ground-based observations. To get confidence in the retrieved cloud properties and derived cloud climatologies, and to learn and understand under which conditions the retrievals are problematic, comparisons were performed for selected regions as well as on a global scale.

Fundamental knowledge on radiative transfer in a cloudy atmosphere, as well as the data, models and techniques used in the retrievals, of relevance to this work, are presented in Chapter 2.

In Chapter 3, a sensitivity study of MERIS cloud top pressure retrieval to cloud vertical profile is performed using radiative transfer simulations. This is done by assuming homogeneous cloud vertical profiles as well as inhomogeneous cloud vertical profiles derived from one year of combined CloudSat and MODIS data. Further, two case studies are presented.

The FAME-C algorithm with its input and output data and assumptions is presented in Chapter 4.

In Chapter 5, both pixel-based retrievals and spatially gridded and temporally averaged products, i.e., cloud climatologies, are evaluated using independent satellite and ground-based observations from passive and active instruments.

The difference in sensitivity of the AATSR and MERIS cloud height retrievals to cloud vertical distribution is demonstrated in Chapter 6. Further, the potential of gaining additional information on cloud characteristics by combining products from independent measurements is shown.

Finally, this thesis concludes with a conclusion and outlook in Chapter 7.

Fundamentals

In satellite remote sensing, cloud properties are not measured directly, since the top-of-atmosphere measurements also include contributions from the atmosphere and the surface. To retrieve the cloud properties from a set of measurements, two main retrieval steps can be distinguished. First, a radiative transfer model is needed that describes the measurements as a function of the atmospheric state and the instrument. A model that computes the set of measurements from the quantities of interest is called a forward model. The radiative transfer models solve the radiative transfer equation for predefined cloud properties, atmospheric profiles and surface properties. Second, an inversion technique is used to estimate the cloud properties from a set of measurements, taking into account uncertainties in the measurements as well as in the forward model.

2.1 Satellite remote sensing and radiative transfer

In the Earth observation science, satellite remote sensing is the technology of acquiring information about the Earth-atmosphere system from measurements of electromagnetic radiation from downward looking sensors onboard space-born platforms. A number of passive multi-spectral imaging radiometers measure the backscattered solar radiation and thermal emission of the Earth-atmosphere system at the top of the atmosphere. Radiation incident on the atmosphere is modified by interaction with molecules and particles in the atmosphere. Information on the composition of the atmosphere can be deduced by comparing the modified radiation to the incident radiation in several spectral bands. In Fig 2.1 the sun-satellite viewing geometry is shown, where the directional relation between the incident so-
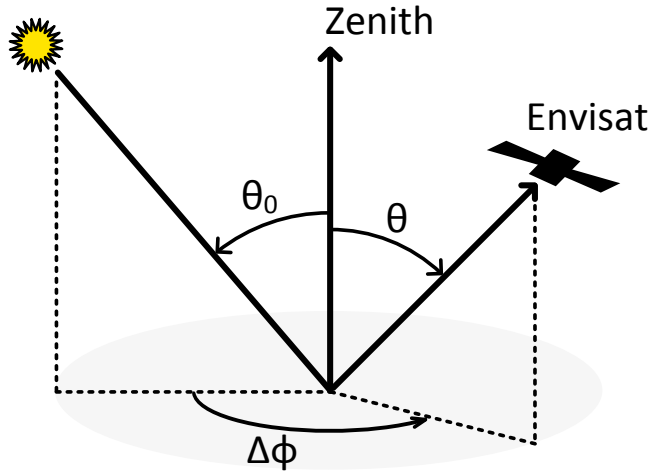
Figure 2.1: Satellite viewing geometry; θ_0 = solar zenith angle, θ = viewing zenith angle, $\Delta\phi$ = relative azimuth angle.

lar radiation and the measured back-scattered radiation is described with three angles: solar zenith angle θ_0; satellite viewing angle θ; relative azimuth angle $\Delta\phi$.

The incident radiation and the modified measured radiation at the satellite are linked through the radiative transfer equation. In many satellite remote sensing applications it is common practice to consider a 1D plane-parallel atmosphere, even in cloudy situations. The 1D assumption means that in radiative transfer computations, the atmospheric properties as well as the cloud properties are only allowed to vary with the vertical coordinate z. Furthermore, the curvature of the Earth-atmosphere system is neglected in a plane parallel representation, which is approximately true for not too large solar zenith angles (Petty, 2006). Though clouds are never homogeneous in their composition in any direction, the assumption of a 1D plane-parallel scattering medium in radiative transfer saves a lot of computation time.

The radiative transfer equation for radiation with wavelength λ, considering only the scalar intensity, so no polarization, and assuming a plane parallel atmosphere, looks as follows:

$$\frac{\mathrm{d}L_\lambda(\mu,\phi)}{\mathrm{d}z} = \frac{\beta_e}{\mu}(L_\lambda(\mu,\phi) - J_\lambda(\mu,\phi)) \tag{2.1}$$

where L_λ is the scalar intensity [W m^{-2} sr^{-1} μm], J_λ is the source function,

z is the path along the vertical, $\mu = \cos\theta$, where θ is the zenith angle, ϕ is the azimuth angle, and β_e is the volume extinction coefficient [m^{-1}]. The volume extinction coefficient is the sum of the absorption coefficient, β_a, and the scattering coefficient, β_s:

$$\beta_e = \beta_s + \beta_a \tag{2.2}$$

The values of β_a and β_s depend on the physical medium the radiation is passing through and the wavelength of the radiation. It is a measure of how strongly radiation is attenuated when traversing a medium over a distance $\mathrm{d}s = \mathrm{d}z/\mu$. Equation 2.1 describes how L_λ is decreased by $\frac{\beta_e}{\mu}L_\lambda$ and increased by $\frac{\beta_e}{\mu}J_\lambda$ along the vertical z. The zenith angle and azimuth angle describe the direction of propagation of the radiation of interest. The source function is given by:

$$J_\lambda(\mu,\phi) = (1-\omega_\lambda)B_\lambda + \frac{\omega_\lambda}{4\pi}\int_0^{2\pi}\int_{-1}^1 P_\lambda(\mu,\phi,;\mu',\phi')I_\lambda(\mu',\phi')\mathrm{d}\mu'\mathrm{d}\phi' \tag{2.3}$$

where ω_λ is the single scattering albedo, B_λ [W m^{-2} μm^{-1}sr^{-1}] is the black body radiation, and P_λ is the phase function. The single scatter albedo is defined as:

$$\omega = \frac{\beta_s}{\beta_e} \tag{2.4}$$

It ranges from zero, for a purely absorbing medium, to one for a purely scattering medium. The intensity of the radiation that is emitted by a black body is given by the Planck's Function:

$$B_\lambda(T) = \frac{2hc^2}{\lambda^5(e^{hc/k_B\lambda T}-1)} \tag{2.5}$$

where T is the temperature of the body, c is the speed of light [ms^{-1}], h is the Planck's constant, and k_B is the Boltzmann's constant. The scattering phase function can be regarded as a probability density. It describes the probability of radiation coming from the direction described by μ' and ϕ'

and being scattered into the direction described by μ and ϕ. For energy conversation, the phase function is normalized:

$$\frac{1}{4\pi} \int_0^{2\pi} \int_{-1}^{1} p_\lambda(\mu, \phi, ; \mu', \phi') I_\lambda(\mu', \phi') \mathrm{d}\mu' \mathrm{d}\phi' = 1 \qquad (2.6)$$

which means that in a purely scattering medium the radiation will be scattered in some direction in the 4π steradians of solid angle.

2.2 Physical and radiative cloud properties

A cloud is a collection of many liquid water cloud droplets and/or ice crystals suspended in the air. Liquid water cloud droplets can have diameters ranging from about 1 to 50 μm. Ice crystals can have equivalent diameters ranging from about 20 to 2000 μm and are observed having all kinds of shapes as shown in Fig. 2.2. The number of cloud particles per volume of air with a cloud droplet radius r, is given by the size distribution of the cloud particles $n(r)$. The total number of cloud droplets per volume of air, N [m^{-3}], is given by:

$$N = \int_0^\infty n(r) \, \mathrm{d}r \qquad (2.7)$$

The mass of cloud water per cubic meter is the cloud water content, CWC [kg/m^3]. For spherical particles it is given by:

$$CWC = \int_0^\infty n(r) \left[\rho_l \frac{4\pi}{3} r^3 \right] \mathrm{d}r \qquad (2.8)$$

The density of pure water, ρ_l, is about 1000 kg/m^3. Integrating the CWC around the total vertical cloud axis, from cloud base z_{base} to cloud top z_{top}, gives the total column cloud water and is called the cloud water path, CWP [kg/m^2].

$$CWP = \int_{z_{base}}^{z_{top}} CWC(z) \, \mathrm{d}z \qquad (2.9)$$

The amount of cloud water is generally controlled by the dynamics and thermodynamics of the air in which the cloud forms. How the condensed water is distributed, e.g., whether many small cloud droplets will form, or less larger cloud droplets, depends on the number of cloud condensation
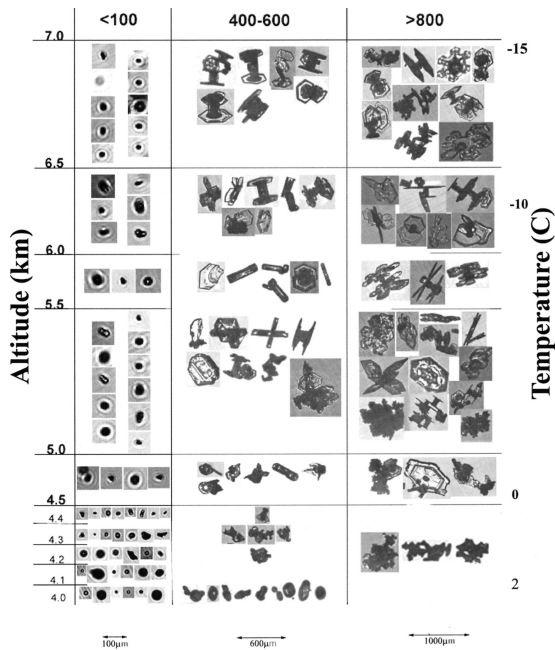
Figure 2.2: Examples of particles for three size ranges and several altitude and temperature ranges observed by a cloud particle imager prove. Image taken from Heymsfield et al. (2002).

nuclei (CCN) that will be activated when the cloud forms. Both natural and anthropogenis aerosols can serve as CCN.

A photon incident on the top of the cloud can interact with the cloud particles by being scattered or absorbed by the cloud particles. The fraction of incident radiation that is absorbed is called the cloud absorptance, a (following definitions and symbols as described in Petty (2006)). The photons that are scattered once or multiple scattered in the cloud can leave the cloud at the cloud top again. This fraction of incident radiation leaving the cloud top after being scattered at least once in the cloud is called the reflectance of the cloud, r. It may also pass the cloud without being scattered or absorbed. This is called the direct transmission. The fraction of incident radiation that passed through the cloud without being scattered or absorbed is called the direct transmittance, t_{dir}. The process of the photon being scattered, and still leaving the cloud at the cloud base, is called diffuse transmission, and the fraction of incident radiation undergoing at least one scatter event, and still leaving the cloud at the cloud base, is called diffuse

transmittance, t_{diff}. The sum of the direct and diffuse transmittance is the total transmittance, t, of the cloud. Together they should sum up to one.

$$t + r + a = 1 \tag{2.10}$$

The direct cloud transmittance can be determined using Beer-Bouguer-Lambert's law:

$$t_{dir}(s) = e^{-\beta_a s} \tag{2.11}$$

In the visible shortwave, clouds scatter strongly the incident radiation, but absorption is very weak. This is why clouds appear opaque and white. In the thermal infrared, radiation is absorbed within a few scattering events. The radiation that was not absorbed by cloud particles are mainly scattered in the forward direction, meaning that the radiative transfer at these wavelengths is dominated by absorption and emission.

The transmittance, reflectance and absorptance of a cloud depend on the total cloud optical thickness, τ , the single scatter albedo, ω, and the scattering phase function, $P(\Theta)$, of the cloud particles. Θ is the scattering angle between the incident radiation on the cloud particle and the scattered radiation. The single scattering albedo is zero when the cloud is purely absorbing and one when the cloud is purely scattering. For clouds it can vary strongly with wavelength, and with the size of the cloud droplets and cloud thermodynamic phase. At visible wavelengths the cloud single-scattering albedo is nearly one for both water and ice particles, while it is clearly lower at infrared wavelengths. Fig. 2.3 shows the single scattering albedo of water clouds for visible and near-infrared wavelengths. The total cloud optical thickness, which is the optical path length along the vertical z, in a plane parallel atmosphere, at wavelength λ, is defined as:

$$\tau = \int_{z_{base}}^{z_{top}} \beta_e(z) \, \mathrm{d}z \tag{2.12}$$

The local volume extinction coefficient, assuming spherical particles, are given by:

$$\beta_e = \int_0^\infty n(r) Q_e(r) \pi r^2 \, \mathrm{d}r \tag{2.13}$$

where Q_e is the extinction efficiency and is the extinction cross-section divided by the geometric cross-section $\pi * r^2$. For cloud particles at visible
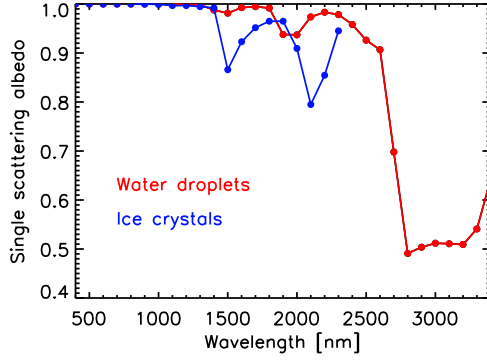
Figure 2.3: The single scattering albedo for cloud water droplets (r_{eff}=10μm) and ice crystals (r_{eff}=40μm) at visible and near-infrared wavelengths. The shortwave scattering properties taken from Baum et al. (2005) were available for wavelengths 0.4-2.2 μm.

wavelengths $Q_e \approx 2$. Eqs. 2.8 and 2.9 2.12, and 2.13 can be combined to give another expression for the total cloud optical thickness:

$$\tau \approx \frac{3LWP}{2\rho_l r_{eff}} \tag{2.14}$$

where r_{eff} is the effective radius and is defined as (Hansen and Hovenier, 1974):

$$r_{eff} = \frac{\int_0^\infty r^3 n(r)\,\mathrm{d}r}{\int_0^\infty r^2 n(r)\,\mathrm{d}r} \tag{2.15}$$

It is the third moment to the second moment and this parameter is often used to describe the radiative properties of a cloud droplet size distribution.

The scattering phase function $P(\Theta)$ describes the relationship between the amount of energy that is scattered at an angle to the direction of the incident radiation. If the cloud particles are spherical (water droplets) or randomly oriented (ice crystals), the scattering phase function can be described only as a function of the scattering angle, Θ, which is the angle between the direction of the scattered photon and the direction of the incident photon on the cloud particle. The relative proportion of the photons
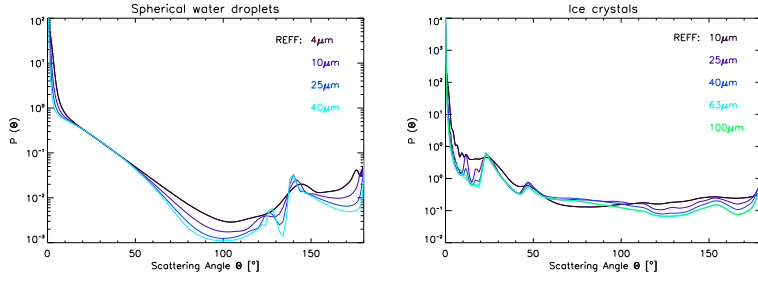
19

Figure 2.4: Scattering phase function for several effective radii (REFF). *Left:* for water clouds. *Right:* for ice clouds.

that are scattered in the forward direction compared to the backward direction is given by the scattering asymmetry factor, g:

$$g = \frac{1}{4\pi} \int_{4\pi} p(\cos\Theta) \, \cos\Theta \, d\omega \qquad (2.16)$$

When the size of the particles is comparable or larger than the wavelength of the radiation, which is true for cloud particles, the tendency is to strongly forward scatter, which means that g will be close to one. For isotropic scattering $g=0$, and if most photons are only scattered in the backward direction g goes to -1. Large cloud water droplets have an asymmetry factor in the order of 0.85 for visible radiation and usually a bit lower values ranging from 0.7 to 0.85 for ice crystals (Diedenhoven et al., 2012). For these conditions and spherical particles, Mie theory (Wiscombe, 1980; Mie, 1908) can be used to determine the scattering phase function. The scattering phase function depends then on the size parameter x, which is $2 \cdot \pi \cdot r / \lambda$, and the refractive index.

In Fig. 2.4 the scattering phase functions for water droplets and ice crystals are shown. For the droplet size distribution a modified Gamma-Hansen distribution (Hansen and Travis, 1974) was assumed with varying effective radius and an effective variance of 0.11. For the ice crystals the scattering phase functions from Baum et al. (2005) were taken. Main features of the scattering phase function consist of the forward and backward peaks at scattering angles 0° and 180°, respectively, and the cloud bow at around 140° for water clouds.

2.3 Imaging multi-spectral radiometers

Imaging radiometers are instruments that measures the natural reflected and emitted radiation from the Earth-atmosphere system within a number of spectral bands. A 2-dimensional array of pixels is obtained with a scanning mechanism. Both AATSR and MERIS, onboard Envisat, are imaging multi-spectral radiometers. Envisat is satellite of the ESA and flies in a sun-synchronous polar orbit at a mean altitude of 800 km and an inclination of 98.6°. Its repeat cycle is 35 days and the mean local solar time at descending node is 10.00 AM. Its measurements provide a global coverage, but can not be used to study the diurnal cycle of geophysical parameters. Envisat was launched in March 2002 and was in operation until April 2012, providing about ten years of data.

AATSR

AATSR was primarily designed for the remote sensing of sea surface temperature (Llewellyn-Jones et al., 2001). It has 7 spectral bands ranging from the visible to the thermal infrared part of the spectrum, see Table 2.1. The earth is scanned with a conical scanning method and for all spectral bands it has a dual-view, nadir and forward, of the earth. For the forward view the satellite zenith angle is about 55°. It has a horizontal resolution of 1 km at sub-satellite point and a swath width of 512 km. Its revisit time is about 3 days.

MERIS

MERIS was primarily desgined for the remote sensing of ocean color (Rast et al., 1999; Bezy et al., 2000). It has 15 spectral bands in the visible and near-infrared part of the spectrum (400 to 905 nm), see Table 2.2. The earth is scanned with a push-broom method with a horizontal resolution of just over 1 km at sub-satellite point in the reduced resolution mode (the regular operation mode). In the full resolution mode the horizontal resolution is about 300 m. The field of view of 68.5°, with a swath width of 1150 km, is covered with five optical cameras arranged in a fan shape configuration. The revisit time is about 3 days. MERIS has a high spectral and radiometric accuracy.

Table 2.1: AATSR spectral channels: cwvl=central wavelength, sst=sea surface temperature (Llewellyn-Jones et al., 2001).

Channel	CWVL [μm]	Width [μm]	Primary application
1	0.55	0.02	Chlorophyll
2	0.66	0.02	Vegetation Index
3	0.87	20	Vegetation Index
4	1.61	0.3	Cloud Clearing
5	3.70	0.3	SST
6	10.85	1.0	SST
7	12.00	1.0	SST

Table 2.2: MERIS spectral channels: cwvl=central wavelength (Rast et al., 1999).

Channel	CWVL [nm]	Width [nm]	Primary application
1	412.5	10	Yellow substance, turbidity
2	442.5	10	Chlorophyll
3	490	10	Clorophyll, pigment
4	510	10	Suspended matter, turbidity
5	560	10	Chlorophyll, suspended matter
6	620	10	Suspended matter
7	665	10	Chlorophyll
8	68125	7.5	Chlorophyll
9	708.25	10	Atmospheric correction, 'red edge'
10	753.75	7.5	COT, CTP reference
11	761.875	3.75	CTP
12	778	10	Aerosol, vegetation
13	865	20	Aerosol, atmospheric correction
14	885	10	Water vapour reference
15	900	10	Water vapour

2.4 Radiative transfer models

To retrieve cloud properties from space, accurate interpretations of the observed radiances are necessary. This is done using radiative transfer models as forward models, which can simulate top-of-atmosphere radiances for predefined atmospheric profiles, surface properties and micro- and macro-physical cloud properties.

In the sensitivity studies presented in this thesis and in the developed FAME-C algorithm, two radiative transfer models were used. First, the Matrix Operator Method (MOMO) (Fischer and Grassl, 1984; Fell and Fischer,

2001; Hollstein and Fischer, 2012) was used to simulate top-of-atmosphere radiances at visible and near-infrared wavelengths. Second, the Radiative Transfer for TOVS (RTTOV), a fast radiative transfer models, was used to simulate clear-sky radiances and clear-sky transmissions at a number of atmospheric levels at infrared wavelengths. Also, RTTOV was used to evaluate the newly developed extension of MOMO into the thermal infrared (Doppler et al., 2014a).

MOMO

MOMO is a 1D plane-parallel radiative transfer model. It can simulate radiative transfer in the atmosphere and ocean for any vertical resolution and optical thickness. In its latest version, radiative transfer simulations can be performed for the spectrum range 0.2 to 100 μm, thus covering the range of wavelengths of solar and terrestrial radiation (Doppler et al., 2014a).

The radiative transfer code is based on the matrix operator method (Plass et al., 1973), which in turn is based on the interaction principle, and combined with the doubling-adding method (Hansen and Hovenier, 1971; Van de Hulst, 1980). They are numerical approaches for computing the radiative transfer in a scattering medium monochromatically and have been used in a number of radiative transfer models (DAK: De Haan et al. (1987); RTMOM: Govaerts (2008)). The interaction principle relates outgoing radiation at the layer boundaries of the medium linearly to the incident radiation on the layer boundaries and the radiation that is generated inside the layer. The radiation field is split into upward and downward going radiation fields, and are described in terms of transmission, reflection and source operators. In the doubling-adding method, each predefined atmospheric layer is subdivided into 2^n identical elementary layers. The n is chosen such that the scattering optical depth $\Delta\tau$ of the elementary layer is small enough to assume single-scattering properties inside the layer: $\Delta\tau=\tau^{-2n} << 1$. The interaction principle is applied to the elementary sublayer. The radiation field is split into upward and downward going radiation fields, and described in terms of transmission (t), reflection (r) and source (j) matrix-operators for the elementary sub-layers and its boundaries. The matrices are $p \times p$ matrices with p the number of ingoing and outgoing directions from which easily the matrix-operators of two adjacent elementary layers (t_2,r_2,j_2)can be computed (double elementary layer). Then, the interaction principle is applied to this double elementary layer. After n steps of doubling, the description of the radiation field for the entire layer is obtained. With the adding method, two non-identical (with different radiative properties) layers are combined in a similar manner, until for all atmospheric layers the
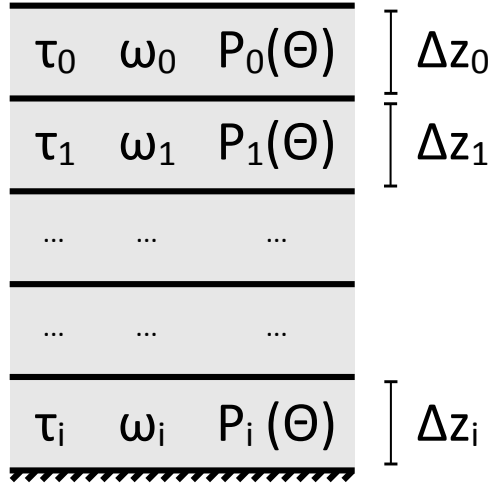
$$\tau_0 \quad \omega_0 \quad P_0(\Theta) \qquad \Delta z_0$$

$$\tau_1 \quad \omega_1 \quad P_1(\Theta) \qquad \Delta z_1$$

$$\ldots \qquad \ldots \qquad \ldots$$

$$\ldots \qquad \ldots \qquad \ldots$$

$$\tau_i \quad \omega_i \quad P_i(\Theta) \qquad \Delta z_i$$

Figure 2.5: The single scattering properties for each of the i pre-defined atmospheric layers in the radiative transfer simulation: τ = cloud optical thickness, ω = single scattering albedo, $P(\Theta)$ = scattering phase function as a function of scattering angle Θ, Δz = layer geometrical thickness.

reflection and transmission have been computed. In case of a vertically inhomogeneous plane parallel atmosphere, the atmosphere is divided into a number of homogeneous layers. This means that within one layer, the optical thickness, single scattering albedo, and the phase function are constant. Within such a layer, the division into the 2^n identical elementary layers is performed.

Thus, the radiative transfer model needs as input for each atmospheric layer the optical thickness and the single scattering properties, i.e., the single scattering albedo, normalized extinction coefficient and the phase function, see Fig. 2.5. In this work, the single scattering properties are computed using a Mie code based on the Mie theory for spherical water droplets or taken from a database Baum et al. (2005) for ice crystals. In the simulations for specific instrument channels performed in this work, the scattering properties at the center wavelength of the channel is used. It is assumed that the variation of the scattering properties within the spectral band of the channel is negligible.

To account for gas absorption within the spectral range of interest, defined by the spectral response function of the instrument channel, the spectroscopy code Coefficient of Gas Absorption (CGASA) (Doppler et al., 2014a) and k-distribution technique of the Institute for Space Sciences (KISS) (Ben-

nartz and Fischer, 2000; Doppler et al., 2014b) were applied for the user-defined atmospheric profiles of temperature and pressure and the vertical distribution of gas and particles. The lines of transmission are computed with a method similar to Line-By-Line Radiative Transfer Model (LBLRTM) (Clough et al., 1992, 2005); a Voigt profile for each absorption line is computed. The spectral information about the gas absorption lines, such as the position of the lines, the strength of the lines and the half-width of the lines, is taken from the High-resolution transmission molecular absorption (HITRAN) database (Rothman et al., 2009, 2013). The water vapor absorption continua are computed using the Mlawer-Tobin-Clough-Keizys-Davies (MT-CKD) coefficients (Mlawer et al., 2012). Due to the huge number of spectral lines of absorption, the spectroscopy codes need to be run at a high spectral resolution, which results in a huge number of spectral subintervals for a spectral band. A line-by-line approach would be to simulate the entire radiative transfer for each of this spectral subinterval. In order to reduce the computation time, KISS is applied to reduce the number of radiative transfer simulations. The k-distribution groups the spectral subintervals computed by CGASA into bins, for which the spectral subintervals have similar gas absorptions for each atmospheric layer. To each bin a gas absorption coefficient and relative weight is assigned and radiative transfer simulations are only performed for each bin. In spectral bands with many absorption lines, e.g., the oxygen-A absorption band (see Fig. 6.1), this will significantly reduce the computation time. It has to be noted that in earlier version of MOMO, that were used for RTM simulations for MERIS channels and AATSR visible and near-infrared channels, the absorption by the water vapour continuum was not taken into account yet. However, for these wavelengths it is negligible: in this spectral range, the foreign continuum of water vapor absorption has to be taken into account for the 800-900 nm spectral band only (Lindstrot et al., 2012). The self-continuum appears in the thermal infrared only (Petty, 2006; Doppler et al., 2014a).

Some limitations occur in MOMO, mainly due to computational efficiency considerations. The zenith and azimuth dependence of the RTE are separated. The zenith angles are defined at the Gauss quadrature points with Gauss Lobatto weights. A Fourier expansion with a finite number of terms is used for the azimuth angles. Further, a phase function truncation is performed to decrease the number of Fourier terms that is needed in the azimuthal radiative transfer computations, whereby forward scattered radiation for small scattering angles is treated as unscattered radiation.

The output of MOMO used in this work are upward directed radiance fields at the top of the atmosphere L as a function of predefined solar zenith angle, viewing angle and azimuth angle , as well as the upward directed ir-

radiances at each predefined atmospheric levels. From the radiances, the reflectance R is determined as follows:

$$R_\lambda = \frac{\pi * L_\lambda(\theta_0, \theta, \phi)}{cos(\theta_0) * F_{0,\lambda}}, \qquad (2.17)$$

where F_0 is the solar constant.

Last, the MOMO version mainly used in this work was first restricted to the shortwave (200-3600 nm), because thermal emission was not included in the simulations. RTTOV, amongst others, was used to evaluate the newly developed extension of MOMO into the thermal infrared. A short description of this work is given in Doppler et al. (2014a).

RTTOV

RTTOV is a very fast radiative transfer model originally created to simulate radiances measured by TOVS. It simulates cleark-sky and cloudy top-of-atmosphere radiances and transmittance profiles for nadir-viewing passive visible, infrared and microwave satellite radiometers (spectral range is 3-20 μm). For a number of channels from a list of instruments from polar orbiting and geostationary satellites, RTTOV computes the top-of-atmosphere upward radiance for user defined atmospheric profiles of temperature and water vapour concentrations, optionally also some other trace gases, and cloud and aerosol particle distributions , surface properties such as surface temperature and emissivity. The simulation of transmission is based on a linear regression method in optical depth using a set of predictors. The set of predictors are based on the input profiles and are defined relative to a reference profile. The regression coefficients are based on transmissions computed with Line-by-line models for a set of different atmospheric profiles that are chosen to represent the range of variations in temperature and gas concentrations found in the atmosphere. For gases that are not allowed to vary in RTTOV, climatological means are used in the LBL computations. The regression coefficients are instrument channel specific, i.e. the transmittances are convolved with the channel spectral response function. RTTOV can also simulate the gradient of the radiances with respect to the atmospheric state parameters at the predefined atmospheric levels.

Though RTTOV is a very fast radiative transfer model, it still is computationally too expensive for retrieving pixel-based cloud properties on a global scale and for a 10 year time period. In this work, RTTOV-7 predictors (Matricardi et al., 2001) were used to simulate the clear-sky transmission values at predefined atmospheric levels for the AATSR infrared channels. At-
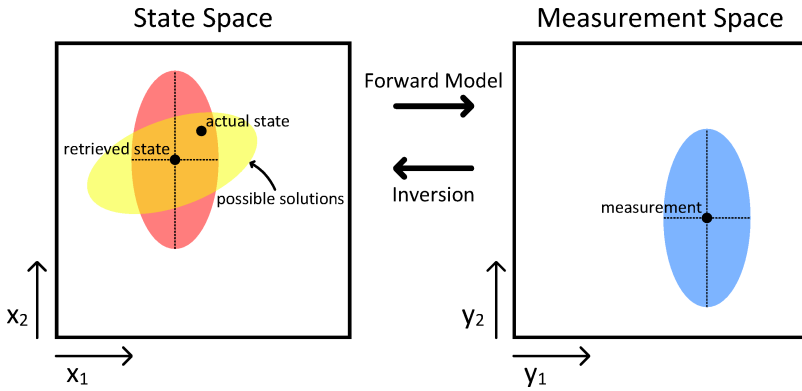
Figure 2.6: Schematic and simple view of the relations between the measurement in the measurement space and the retrieved state in the state space. Shown for a state vector $\vec{x}$ and measurement vector $\vec{x}$, each consisting of two elements. The ellipses represent the uncertainties in each state parameter and measurement.

mospheric profiles were taken from numerical weather prediction model re-analysis data on a much lower spatial resolution than the satellite pixels.

2.5 Inversion technique

Retrieval algorithms that estimate a set of parameter, e.g., cloud properties, from a set of measured quantities, e.g., TOA radiances, use inversion techniques. In many cases an iterative optimization of the forward model is performed to find the best fit between the set of observed measurements and the set of simulated measurements. Often it is computationally too expensive to let an RTM run for every satellite pixel for which cloud properties should be retrieved, especially if this is done globally and for a long time period, in order to create, e.g., global cloud climatologies. One way to deal with this issue is to store a large number of radiative transfer simulations performed for a range of varying conditions (e.g., atmospheric-, surface- and cloud properties, viewing geometry) into large tables, so called Look-Up Tables (LUTs). The interpolation applied to the LUTs to obtain simulated radiances is part of the forward model.

The relationship between a set of measurements assembled in the measurement vector $\vec{y}$ and a set of quantities to be retrieved assembled in the state vector $\vec{x}$ is given by:

$$\vec{y} = F(\vec{x}, \vec{b}) + \epsilon \tag{2.18}$$

27

where $F(\vec{x}, \vec{b})$ is the forward model, $\vec{b}$ is a set of known parameters needed in the forward model also called background state, and ϵ is the error vector. The error vector includes contributions from erros in the measurements, forward model and forward model parameters. Uncertainties in the measurements can, e.g., arise from instrument noise (example of random error) and calibration errors (example of systematic error). Errors in the forward model can arise from wrong assumptions in the model, such as assuming a plane-parallel atmosphere in the radiative transfer simulations. Forward model parameters, are parameters on which the forward model depends, but which are not retrieved, e.g., surface albedo. The total uncertainty between $\vec{y}$ and $F(\vec{x}, \vec{b})$ resulting from the error contributions is defined by the error covariance matrix $\mathbf{S}_\epsilon$ (Grainger, 2015):

$$\mathbf{S}_\epsilon = \left[\vec{y} - F(\vec{x}, \vec{b})\right]\left[\vec{y} - F(\vec{x}, \vec{b})\right]^T \tag{2.19}$$

Basically, the inversion is done by minimizing a least-square cost function with respect to $\vec{x}$. One way of performing such an inversion with the consideration of former mentioned uncertainties is the optimal estimation (OE) method (Rodgers, 2000). It enables error propagation of measurements, forward model and forward model parameters as well as the inclusion of a-priori knowledge to constrain possible solutions. The OE method uses Bayes' theorem and Gaussian statistics. Minimizing the cost function J, weighted by the uncertainties in the measurements, forward model (parameters) and a-priori values, is analogues to maximizing the probability of $\vec{x}$ under conditions of $\vec{y}$ and a priori information.

$$J(\vec{x}) = [\vec{y} - \mathbf{K}\vec{x}]^T \mathbf{S}_\epsilon^{-1} [\vec{y} - \mathbf{K}\vec{x}] + [\vec{x} - \vec{x}_a]^T \mathbf{S}_a^{-1} [\vec{x} - \vec{x}_a] \tag{2.20}$$

Here x_a is the a-priori state vector and S_a the a-priori error covariance matrix. Assuming local linearity around $\vec{x}$ than $F(\vec{x}, \vec{b})$ can be replaced by $\mathbf{K}\vec{x}$. The Jacobian or weighting function of the forward model $\mathbf{K}$ is given by:

$$\mathbf{K} = \frac{\partial F(\vec{x}, \vec{b})}{\partial \vec{x}} \tag{2.21}$$

It describes the sensitivity of the measurements to the state variables. It maps the state variables into the measurement space, see Fig. 2.6.

Error estimates for the retrieved state are computed by applying:

$$\mathbf{S}_\epsilon = \mathbf{S}_y + \mathbf{S}_{fm} + \mathbf{K}_B \mathbf{S}_B \mathbf{K}_B^T \tag{2.22}$$

where $\mathbf{S}_y$ is the error covariance matrix which describes the uncertainties in the measurements, $\mathbf{S}_{fm}$ is the error covariance matrix which describes the uncertainties in the forward model, $\mathbf{S}_B$ is the error covariance matrix which describes the uncertainties in the forward model parameters, and K_B is the weighting function which maps the forward model parameter uncertainties into measurement space.

The error covariance matrix $\mathbf{S}_x$ of the retrieved state, or the optimal estimate, is given by:

$$\mathbf{S}_x = \mathbf{S}_a + \left[\mathbf{K}^T \mathbf{S}_\epsilon^{-1} \mathbf{K}\right]^{-1} \tag{2.23}$$

The validity of the uncertainty of the retrieved state depends on accurate characterization of the uncertainties in the measurements, forward model and forward model parameters as well as the a priori state. Prior knowledge can come from (analytical) models, climatologies based on independent measurements, or just an educated guess. In this work, 'typical' values of the cloud properties for both water and ice clouds are used (see Sect. 4.4). However, the uncertainties are set to very high values, thus the solution is hardly constrained by the a priori state vector.

In several retrieval applications, the cost is used as a measure of consistency of the retrieved state with the measurements and a priori data (goodness-of-fit statistic) (e.g. Sayer et al., 2011). High values of the cost function for certain retrievals can help to identify scenes which might be poorly described by the forward model. These 'problematic' retrievals should then be treated with care in further applications.

For more details on inversion methods in retrieval theory the interested reader is referred to Rodgers (2000) and Grainger (2015).

CHAPTER

3

MERIS cloud top pressure retrievals assuming vertically inhomogeneous cloud profiles

Abstract A synergistic FAME-C (Freie Universität Berlin AATSR-MERIS Cloud Retrieval) algorithm is developed within the frame of the ESA CCI Cloud project. Within FAME-C the ratio of two MERIS measurements (the Oxygen-A absorption channel and a window channel) is used to retrieve cloud top pressure. In case of high, extended clouds the retrieved cloud top pressure is generally too high. This can be understood as an overestimation of extinction in upper cloud layers due to the assumption of vertical homogeneous clouds in the radiative transfer simulations. To include more realistic cloud vertical profiles, one year of data from the Cloud Profiling Radar (CPR) onboard CloudSat has been used to determine mean normalized cloud vertical extinction profiles with a fixed pressure thickness for nine cloud types. The nine cloud types are based on the ISCCP COT-CTP classification table. The retrieved cloud top pressure, now using CloudSat cloud profiles in the forward model, is compared to CPR reflectivities as well as the retrieved cloud top pressure using vertically homogeneous cloud profiles. In the first pair of cases under examination the overestimation of cloud top pressure, and therefore the bias, is reduced by a large amount when using CloudSat vertical cloud profiles. Another advantage is that no assumption about the cloud geometrical thickness has to be made in the new retrieval.

Section 3.2 and 3.5 of this chapter are based on Henken et al. (2013)

3.1   Introduction

As was described in Ch. 2, a photon passing through the atmosphere will
in the end either be absorbed by atmospheric constituents or at the Earth's
surface, or scattered back to space. In the visible and near-infrared wave-
lengths, where the source of radiation is the sun, the mean photon path
length between the sun and the satellite instrument depends primarily on
the sun-satellite viewing geometry, the scattering and absorption proper-
ties of atmospheric constituents and the surface albedo. In the presence of
clouds the mean photon path length is usually shortened, due to photons
being reflected back to space by cloud particles.

Hanel (1961) suggested that the cloud top height could be estimated from
satellite measurements of reflected solar radiation in an absorption band.
Yamamoto and Wark (1961) proposed to use the oxygen-A absorption band
centered at around 760 nm. The idea is based on the assumption that the
strength of the absorption of radiation by a well-mixed atmospheric gas like
oxygen can be directly related to the mean photon path length of the re-
flected radiation. In the presence of clouds, the mean photon path length is
mainly determined by the airmass above the cloud, thus the cloud top pres-
sure. In case of high clouds with low cloud top pressures, the mean photon
path length is shorter and the transmission is lower than in the case of low
clouds with high cloud top pressures. The transmission in the oxygen-A ab-
sorption band can be approximated by the ratio of measured radiances in
an absorbing channel in the oxygen-A band and in a near-by window chan-
nel (no significant absorption of radiation).

The feasibility of retrieving cloud top pressure by measuring the reflected
solar radiation in the oxygen-A band from satellites was already analyzed in
the 1960s by experimenting with hand-held spectrograph camera's (Saiedy
et al., 1965, 1967). The potential and accuracy of this cloud top height
retrieval method was analyzed further in a couple of aircraft validation
campaigns. Cloud top pressures were retrieved for low-level clouds (Stra-
tocumulus decks) from measurements of an spectrometer onboard a re-
search aircraft (Fischer et al., 1991). The accuracy of the retrieved cloud
top pressure was within 40 m when compared to simultaneously taken lidar
measurements. A validation of ESAs operational MERIS cloud-top pressure
product (Merheim-Kealy et al., 1999) was performed by comparison with
cloud top heights as observed with the Portable Lidar System (POLIS) on-
board a small aircraft (Lindstrot et al., 2006). Several validation flights were
performed in Germany during spring 2004. The validation exercise was fo-
cused on situations with low-level clouds (< 3000 m). It revealed a mean
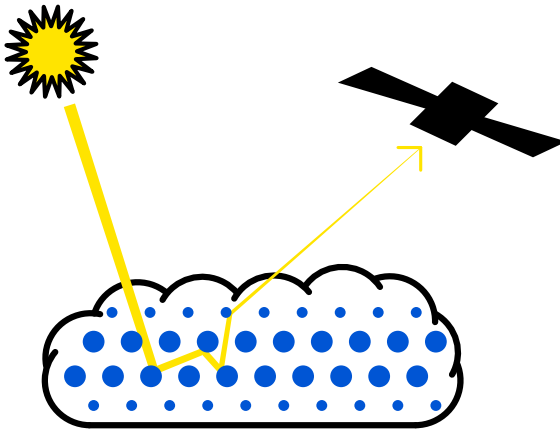bias of about -22 hPa and a root mean square error (RMSE) of about 24

Figure 3.1: Increase of photon path length due to multiple scattering in the cloud.

hPa. Buriez et al. (1997) developed for POLDER the first operational satellite based retrieval of cloud pressure, or the so called *apparent pressure*, using measurements in the oxygen-A absorption band. Vanbauce et al. (1998) found a bias of 170 hPa with respect to cloud top heights derived from cloud top temperatures retrieved from Meteosat measurements. Further, a large positive bias was found for the retrieved apparent cloud pressure, now taking surface reflection into account, when compared to ground-based lidar and radar observations (Vanbauce et al., 2003). The retrieved cloud pressures were close to pressure levels corresponding to the geometrical middle of the cloud.

Several validation exercises have shown that the cloud top pressure can be retrieved accurately (low bias) for single-layer, low-level and optically thick clouds. However, including also various cloud types such as vertically extended and multi-layer clouds, the bias increases significantly and retrieved cloud pressures correspond to pressure levels somewhere in the middle of the cloud rather than the cloud top. A large part of the overestimation of cloud top pressures can be attributed to multi-scattering in the cloud, which is not taken into account in many of the retrievals.

Due to multi-scattering in the cloud, the mean photon path length is increased, as shown schematically in Fig. 3.1. The larger the photon penetration depth in the cloud, the higher the probability that radiation in the oxygen-A band is absorbed. The radiances in a window channel primarily depend on the total cloud optical thickness, while for the radiances in the absorption channel, the vertical distribution of cloud optical thickness

and the cloud geometrical thickness, or combined the vertical extinction profile, can strongly influence the amount of absorption taking place due to an increase of mean photon path length. In terms of a physical cloud property the cloud vertical profile can be described by the vertical distribution of cloud water content. The sensitivity of cloud top pressure retrievals using measurements in the oxygen-A absorption band to in-cloud photon penetration depth was acknowledged in several theoretical and validation studies (Saiedy et al., 1965; Wu, 1985; Fischer and Grassl, 1991b).

In a sensitivity study performed by Preusker and Lindstrot (2009), the sensitivity of the ratio of the MERIS absorption channel 11 and window channel 10 to a set of varying cloud, atmospheric and surface parameters was studied: cloud top pressure, cloud optical thickness, cloud geometrical thickness, cloud fraction, atmospheric temperature profiles, surface albedo, surface pressure. It was shown that the sensitivity of the MERIS ratio to changes in cloud top pressure is significant except for a thin cloud above a highly reflecting surface. Furthermore, the sensitivities to changes in CTP and geometrical thickness are strongly correlated, making it difficult to disentangle them. Changes in cloud micro-physics and the temperature profile only have minor impacts with maximum errors of less then 10 and 20 hPa, respectively, and are considered small with regards to other error sources. The largest source of error in the CTP retrieval is the presence of multilayer clouds, in the study defined as thin cirrus over low-level water clouds. Multi-layer clouds represent an extreme case of inhomogeneous cloud vertical profiles.

In an accurate cloud top pressure retrieval using measurements in the oxygen-A absorption band from passive imagers, the knowledge on total COT, vertical extinction profile and surface albedo are of most importance in most cases, assuming that the instrument characteristics are well known. The surface albedo can be taken from independent measurements (considered as auxiliary data) and COT can often be easily estimated. Hence leaving the unknown vertical extinction profile as the main source of error in the retrieval.

In this study, the focus is on the impact of assumed cloud vertical extinction profiles on the simulated ratio of the MERIS channel 11 in the oxygen-A absorption band and the near-by window channel 10, see Fig. 3.2. Simulations are performed assuming homogeneous cloud vertical extinction profiles as well as inhomogeneous cloud vertical extinction profiles. For the purpose of deriving the latter type of profiles, observations from a spaceborn cloud radar were taken to create mean vertical extinction profiles for several cloud types. The profiles were then used in radiative transfer sim-
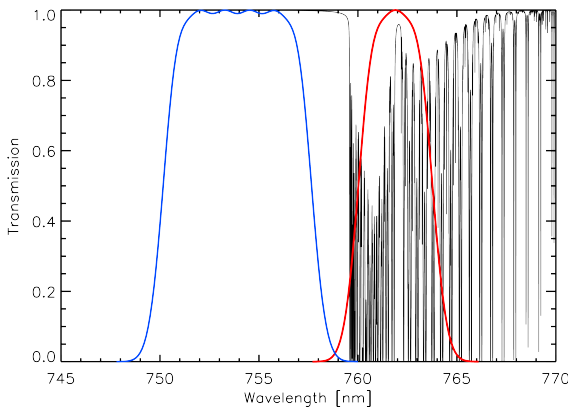
Figure 3.2: MERIS spectral response function for the window channel 10 (blue) and channel 11 in the oxygen-A absorption band (red). In black are shown the oxygen absorption lines.

ulations that served as a basis for the forward model in form of LUTs in the MERIS based cloud top pressure retrieval. The impact of the assumed vertical extinction profiles on the simulated ratios is shown. In addition, the retrieval was applied to two case studies and compared to cloud top heights as observed by CPR.

3.2 Cloud vertical extinction profiles

The active instrument CPR onboard CloudSat, which is part of the A-train constellation, provides valuable observations of cloud vertical profiles. The observations have shown the large variability in the vertical structure of clouds occurring in nature. Many of the profiles would not be well represented by homogeneous cloud vertical profiles. For example, CPR and CALIOP observations show that vertically extended clouds often appear to have maximum extinction values in lower cloud layers (e.g. Ham et al., 2013).

To derive cloud vertical extinction profiles, one year (2010) of the 2B-TAU product as provided by the CloudSat database (Polonsky et al., 2008) have been used. The layer COTs are derived from a combination of the CPR measurements, COTs retrieved from MODIS onboard Aqua, and analysis by European Centre for Medium-Range Weather Forecasts (ECMWF). The vertical extinction profile is determined by dividing the layer COT by the geometrical thickness of each cloud layer. Since different types of clouds
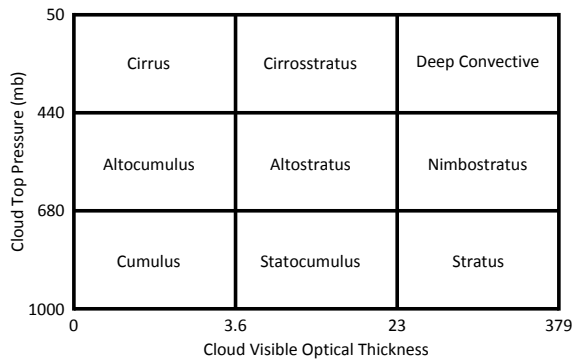
Figure 3.3: ISCCP cloud classification in terms of cloud top pressure and cloud optical
thickness (Rossow and Schiffer, 1999).

show different vertical extinction profiles it has been decided to determine
mean vertical extinction profiles for nine cloud types as given by the ISCCP
daytime cloud classification (Rossow and Schiffer, 1999). This cloud clas-
sification is based on cloud optical thickness and cloud top pressure and
identifies the following cloud types: Cirrus, Cirrostratus, Deep Convection,
Altocumulus, Altostratus, Nimbostratus, Cumulus, Stratocumulus and Stra-
tus, see Fig. 3.3. For each cloud type a 'typical' fixed number of cloud levels
has been chosen based on first analyses of the CloudSat data. Furthermore,
a set of data selection criteria has been used to derive the mean cloud ver-
tical extinction profiles. Only cloudy observations consisting of at least 2
range bins in the radar data are taken into account. Also, a maximum gap
of two range bins is allowed and a minimum total optical thickness of 0.5
is considered. The resulting averaged and normalized cloud vertical extinc-
tion profiles for each of the nine cloud types are shown in Fig. 3.4. For
most cloud types the lower cloud layers tend to have higher extinction val-
ues than upper cloud layers.

3.3 MOMO simulations

Radiative transfer simulations are performed using the MOMO radiative
transfer model. The atmosphere was divided into 50 atmospheric layers,
whereby the layers in the troposphere have a layer thickness of 20 hPa.
A US Standard Atmosphere was assumed in the simulations (McClatchey
et al., 1972). The surface is modeled as a Lambertian reflector. A Rayleigh
optical thickness of 0.026 is taken and no aerosols are included. To simulate
the absorption of atmospheric gases within a predefined accuracy, about
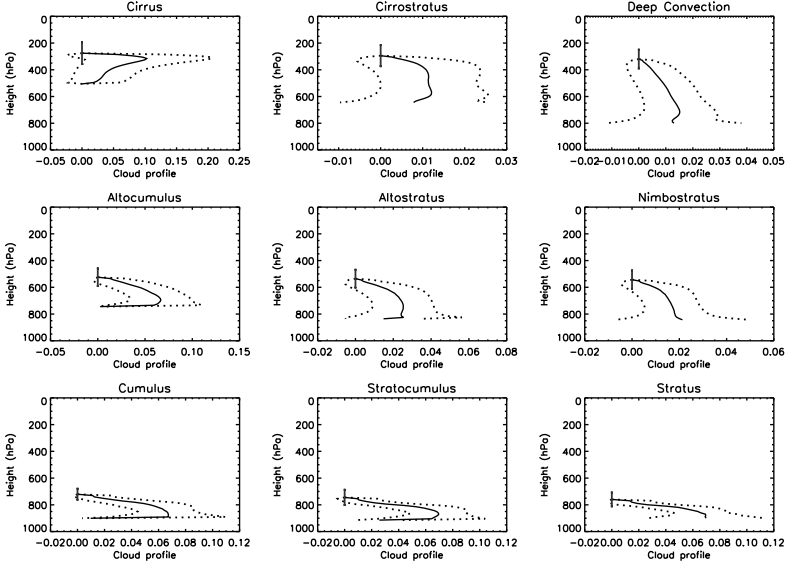
Figure 3.4: Normalized and averaged cloud vertical extinction profiles (solid lines) derived from CloudSat CPR data for nine cloud types as defined in Fig. 3.3. Standard deviations of extinction are shown with dotted lines, and standard deviations of the cloud top pressure are shown with error bars.

70 bins in the k-distribution method are used for the simulations in channel 11. The spectral variation of the solar constant is accounted for by adjusting the weights of the bins accordingly.

Cloud layers at pressure levels above 440 hPa are simulated assuming an effective radius of 10 μm and using the radiative properties of water droplets, while for cloud layers at pressure levels below 440 hPa ice crystals are assumed. A Mie code based on Mie-theory (Wiscombe, 1980; Mie, 1908) was used to compute the phase functions for water droplets in a liquid cloud, as well as the extinction coefficient and single-scattering albedo. For the droplet size distribution the modified Gamma droplet size distribution is assumed (Hansen and Travis, 1974), where the mode radius equals the effective radius (Hansen and Hovenier, 1974):

$$n(r) = r^{\frac{1-3v_{eff}}{v_{eff}}} \cdot e^{-\frac{r}{r_{eff}v_{eff}}} \tag{3.1}$$

This droplet size distribution is described with the use of the effective radius
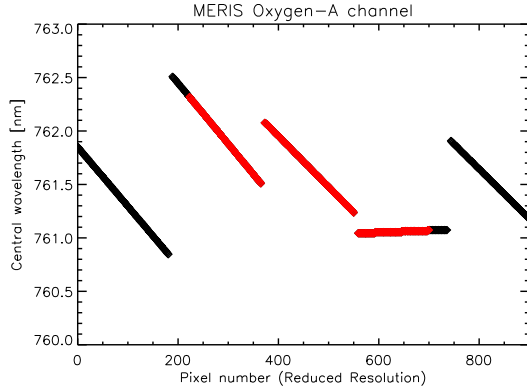
Figure 3.5: MERIS central wavelength per pixel number. The five optical camera's can be identified easily. In red are the pixels indicated that fall within the field of view of AATSR, thus the collocated AATSR-MERIS measurements.

and the effective variance v_{eff} , which is given by:

$$v_{eff} = \frac{\int_0^\infty (r - r_{eff}) r^2 n(r)\, \mathrm{d}r}{r_{eff} \int_0^\infty r^2 n(r)\, \mathrm{d}r} \tag{3.2}$$

The modified Gamma droplet size distribution is taken because the parameters describing it are equal to the parameters that describe the radiative scattering properties of the distribution. For ice clouds, the scattering phase functions and single scattering properties from Baum et al. (2005) are used assuming an effective radius of 40 μm.

The central wavelength of the MERIS channels vary across the field of view. This effect is called the spectral smile, which was determined in several spectral calibration campaigns (Delwart et al., 2007). In the oxygen-A absorption band a change in the central wavelength can result in different observed strengths of absorption. Hence, simulations are also performed for varying central wavelengths of the spectral response function of channel 11. Figure 3.5 shows the central wavelengths varying across the field of view, represented by the pixel number of the camera's. In red are the pixels indicated that fall within the AATSR swath. Its width is about half of the MERIS swath width. Since FAME-C is a daytime cloud property retrieval and applied to collocated AATSR and MERIS measurements, only the central wavelengths covering the combined field of view are taken into account in the production of the forward models.
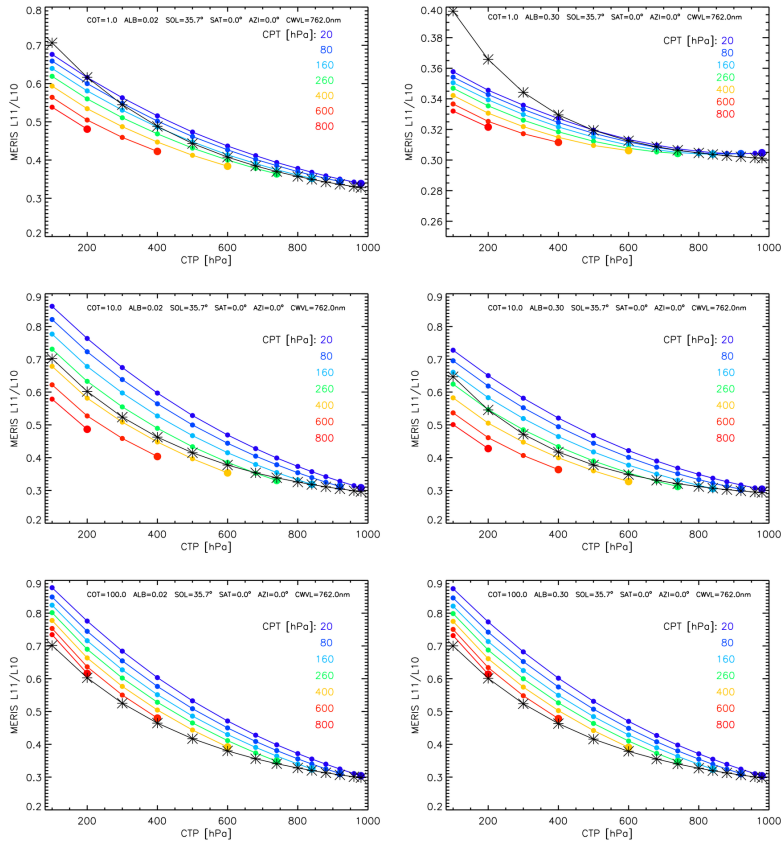
Figure 3.6: The ratio of MERIS channels L11 and L10 for several cloud top pressures and cloud optical thicknesses and for homogeneous and inhomogeneous cloud vertical extinction profiles.

For each simulation assuming one of the vertically inhomogeneous clouds, several counterpart simulations assuming the homogeneous vertical profile were performed by varying the cloud geometrical thickness. All other parameters, such as CTP, COT and surface albedo, were kept constant and equal to the inhomogeneous version.

3.4 Simulation results

The impact of the assumed vertical extinction profiles on the simulated MERIS ratio is presented in Fig. 3.6, which shows the change of the ratio for changing cloud top pressures, i.e., the sensitivity. For the vertically homogeneous cloud profiles the results for varying cloud geometrical thickness in terms of cloud pressure thickness (CPT in hPa) are also shown. Furthermore, the results are shown for optically thin (1), middle (10) and thick (100) clouds as well as for low (0.02) and high (0.3) surface albedo. A central wavelength of 762 nm was used in these simulations, since at this wavelength the sensitivity of the ratio to a change in CTP, COT, CPT, and surface albedo was found to be high (Preusker and Lindstrot, 2009).

First, a description of the dependence of the ratios on the various parameters is given. The ratios increase for decreasing CTP, increasing COT, decreasing surface albedo, and decreasing geometrical thickness for the homogeneous clouds. The ratio increases for increasing COT, because the photon penetration depth is lower which results in less absorption of radiation in channel 11. An increase in the surface albedo leads to an increase in the ratio, because its contribution to the top-of-atmosphere radiation observed in the absorption channel 11 is smaller than for the window channel 10. For optically very thick clouds (COT=100), this influence is negligible. By increasing the geometrical thickness of a cloud, the extinction in each cloud layer is decreased, which results in higher photon penetration depths and thus more absorption of radiation taking place in channel 11.

The sensitivity is defined as the change of the ratio for changing cloud top pressures, which can be observed qualitatively by the curvature of the lines. For all clouds, the sensitivity increases with decreasing CTP. This can be observed by an increasing rise of the ratio for decreasing CTPs. Furthermore, the sensitivity increases for increasing COT and decreasing surface albedo. The impact of CPT on the sensitivity is lower than for the latter two parameters. The sensitivity is highest for optically thick clouds above a dark surface and lowest for optically thin clouds above a bright surface. These findings are in agreement with the findings in Preusker and Lindstrot (2009).

Comparing the simulated ratios for homogeneous clouds, with varying CPTs, to the simulated ratios for inhomogeneous clouds shows that the assumed vertical extinction profile obviously will have a large impact on CTP retrievals using measurements in the oxygen-A absorption band. For example, a look at the middle panel on the left shows that a homogeneous cloud with COT=10, CTP=400 hPa and CPT=160 hPa and another homogeneous cloud with the same COT, but CTP=200 hPa and CPT=600 hPA will lead to similar observed ratios. The inhomogeneous cloud type with the same COT

needs to have CTP=300 hPa in order to observe a similar ratio. For the homogeneous clouds, the impact of the assumed cloud geometrical thickness on the simulated ratio is highest for clouds with COT=10. This can be explained as follows. For optically thin clouds, the radiation interacts less with the cloud particles, thus reducing the influence of the cloud vertical extinction profile. For optically thick clouds, most radiation that is observed at TOA stems from upper parts of the clouds, thus suppressing the influence of the entire cloud vertical extinction profile on the observed ratio. For optically thick clouds, the ratios of the homogeneous clouds are always higher than the ratios of the corresponding inhomogeneous cloud, even when increasing the geometrical thickness such that the homogeneous clouds extend down to the surface. The extinction values in the upper cloud layers are higher for the homogeneous clouds than the inhomogeneous clouds, which has higher extinction values at lower cloud layers.

3.5   Case studies

The technical framework in which the MERIS-CTP retrievals were performed is a precursor, but very similar to the FAME-C algorithm presented in Ch. 4. The MERIS-CTP retrieval 1) assuming vertically homogeneous extinction profiles (HOM) and 2) assuming the CPR vertical extinction profiles were performed and compared to CPR observations for two case studies. Spatially matching satellite overpasses of Envisat and CloudSat within a short time period only occurred at high latitudes (about 70°). The two case studies were manually selected in such a way that the time difference between the overpasses of CloudSat and Envisat is within several minutes. Further, influence of underlaying snow/ice surfaces, which complicate the retrievals, were limited by considering only cases in the Northern hemisphere during the summer time. This allows also to use cases with lower solar zenith angles than in other seasons. Moreover, cases which appeared spatially too inhomogeneous along the CloudSat track were not considered, due to difficulties in matching the observations in space (different viewing geometries) and time.

The resulting cloud top height retrievals along the CloudSat track are presented in Fig. 3.7. From the CPR radar reflectivity factors (>25 dBZ) and the CPR cloud mask (CPR CM) it can be seen that in both cases the clouds have mostly high cloud top heights (CTHs) > 5 km. The clouds extend down to altitudes close to the surface. For comparisons to the CPR-CTH, the retrieved MERIS cloud top pressures are converted to cloud top heights using the ECMWF atmospheric profiles provided by the CloudSat database. In addition, the AATSR cloud top temperatures were retrieved and also converted
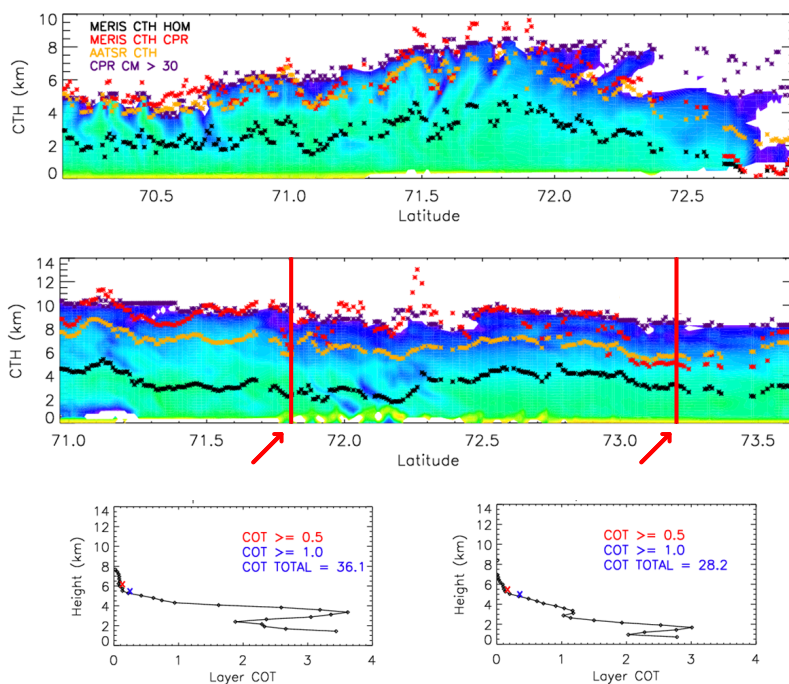
Figure 3.7: Comparison of MERIS cloud top height retrievals assuming a homogeneous cloud vertical extinction profile (MERIS CTH HOM) and using the CloudSat derived cloud vertical extinction profiles (MERIS CTH CPR) with cloud top heights determined from CloudSat (CPR). Also shown are the cloud top heights retrieved from AATSR infrared measurements (AATSR CTH). *Top:* Case A, 3 August 2008 at 23.01 UTC. *Bottom:* Case B, 8 June 2008 at 15.38 UTC.

to cloud top heights.

For both cases, the MERIS-CTHs retrieved with vertically homogeneous cloud profiles are located somewhere in the middle of the cloud, indicating an overestimation of CTP. The MERIS-CTHs retrieved with the CloudSat vertical extinction profiles are much closer to the cloud top height as observed by CPR. The overestimation of CTP when assuming vertically homogeneous cloud profiles can be explained as follows: The clouds have very low extinction values in the upper layers (this has been analyzed using the CPR-derived layer optical thickness). In the radiative transfer simulations, the extinction values are thus assumed too high in the upper cloud levels, which decreases the mean photon path length, and decreases the absorption by oxygen. A too high MERIS ratio is simulated, eventually resulting

Table 3.1: Calculated bias [km] and RMSE [km] for cases A and B (as in Fig. 3.7) from comparing retrieved MERIS-CTH, with vertically homogeneous extinction profiles (HOM) and with CPR vertical extinction profiles, to cloud top height as observed by CPR.

	Bias		RMSD	
	HOM	CPR	HOM	CPR
Case A	-5.85	-0.81	5.91	1.63
Case B	-3.84	-0.96	4.01	2.05

in an overestimation of CTP. The low layer optical thicknesses in the upper cloud layers can also be seen by the penetration depth of AATSR-CTH, especially for case A. Nevertheless, for both cases the MERIS-CTHs assuming CPR profiles show a large reduction in bias and root mean square deviation (RMSD, not corrected for bias) compared to MERIS-CTH assuming HOM profiles, see Table 3.1.

In the retrieval of MERIS-CTP for homogeneous clouds, an estimate of the geometrical thickness must be made. A naive approach was used, which is based on the relationship between the liquid water path and cloud geometrical thickness for adiabatic clouds, which assumes a linear increase of liquid water content with height. For vertically extend clouds, this will usually result in clearly too low geometrical thicknesses. However, allowing the clouds to extend down to the surface did not have a large impact on the retrieved MERIS-CTP for homogeneous clouds (not shown). This is due to the fact that in these two cases the clouds are optically very thin, thus having low extinction values, in the upper few kilometers. The too high assumed extinction values in the upper cloud layers in the homogeneous profiles can not be significantly reduced by extending the geometrical thickness.

3.6 Discussion and outlook

The comparison between simulated MERIS ratios assuming vertically homogeneous and inhomogeneous extinction profiles showed that large differences can occur, especially for optically thick and vertically extended clouds. In most cases, the ratio is higher for homogeneous clouds, due to the fact that the inhomogeneous cloud profiles have lower extinction values in the upper cloud layers.

First analyses of CTP retrievals using MERIS measurements show an encouraging improvement of the retrieved MERIS-CTPs for high, vertically extended clouds, taking mean cloud vertical extinction profiles derived from
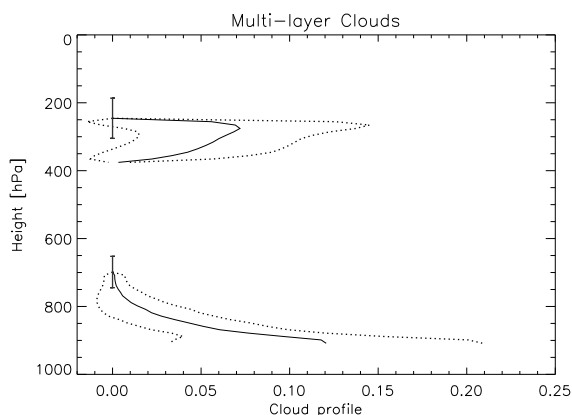
Figure 3.8: Average vertical extinction profiles for multi-layer clouds derived from CPR data.

one year of CloudSat data for several cloud types, with respect to retrieved MERIS-CTPs assuming homogeneous vertical cloud profiles. The improvement is seen in terms of a large decrease in bias when comparing to cloud top heights from CloudSat radar reflectivities and cloud mask data for two cases. Moreover, no assumption on the cloud geometrical thickness has to be made since the number of cloud levels is fixed for each of the nine cloud types. This reduces the dimensions in the LUTs that serve as forward models in the retrieval, and this in turn increases the retrieval efficiency. One aspect which needs further attention is the apparent increase in scatter in the retrieved CTP when using the CloudSat cloud vertical profiles. It is partly related to a sudden transition from one cloud type to another within one CTP retrieval. This problem could be overcome by smoothing the relevant subspace in the LUT before the iteration in the inversion starts. It has to be noted that a number of difficulties arise when comparing FAME-C cloud products to A-train cloud products due to overlapping overflights only at high latitudes ($> 70°$). The pixel-based comparison is complicated due to parallax effects and time differences between the Envisat and CloudSat overpasses.

In the future, CALIOP data can be analyzed and combined with the CPR data to obtain cloud vertical extinction profiles. Since the lidar is more sensitive to smaller cloud particles, this may lead to a more complete view on cloud vertical extinction profiles for various cloud types. Also, an mean cloud vertical extinction profile for multi-layer cloud situations, representing the most extreme case of vertically inhomogeneous clouds, is considered to be

included in the MERIS-CTP retrieval. The cloud height retrieval in multi-layer cloud situations could be performed in a similar way as described in Lindstrot et al. (2010b). Figure 3.8 shows the mean vertical extinction profile for multi-layer clouds derived from the CPR data. Multi-layer clouds are defined as thin cirrus clouds (CTP < 440 hPa and COT < 3.6) above low-level water (CTP > 680 hPa and COT > 3.6) clouds.

CHAPTER 4
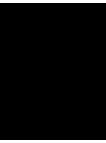
FAME-C cloud property retrieval using synergistic AATSR and MERIS observations

Abstract A newly developed daytime cloud property retrieval algorithm, FAME-C (Freie Universität Berlin AATSR MERIS Cloud), is presented. Synergistic observations from the Advanced Along-Track Scanning Radiometer (AATSR) and the Medium Resolution Imaging Spectrometer (MERIS), both mounted on the polar-orbiting Environmental Satellite (Envisat), are used for cloud screening. For cloudy pixels two main steps are carried out in a sequential form. First, a cloud optical and micro-physical property retrieval is performed using an AATSR near-infrared and visible channel. Cloud phase, cloud optical thickness, and effective radius are retrieved, and subsequently cloud water path is computed. Second, two cloud top height products are retrieved based on independent techniques. For cloud top temperature, measurements in the AATSR infrared channels are used, while for cloud top pressure, measurements in the MERIS oxygen-A absorption channel are used. Results from the cloud optical and micro-physical property retrieval serve as input for the two cloud top height retrievals. Introduced here are the AATSR and MERIS forward models and auxiliary data needed in FAME-C. Also, the optimal estimation method, which provides uncertainty estimates of the retrieved property on a pixel basis, is presented.

This chapter is based on Sect. 1-4 of Carbajal Henken et al. (2014)

4.1 Introduction

In the Earth's present climate system clouds play a key role through their strong interaction with solar radiation and thermal radiation emitted by the Earth's surface and atmosphere as well as their dominant role in the hydrological cycle. On average about 70 % (Stubenrauch et al., 2013) of the Earth's surface is covered by clouds and their temporal and spatial variability is high. Climate models are used to improve our understanding of regional and global climate and to project future climate changes. However, low confidence is given to the representation and quantification of cloud processes in these models, especially in combination with aerosol processes. Cloud adjustments due to aerosols still contribute the largest uncertainty to the total radiative forcing estimate (IPCC, 2013).

Accurate observations of cloud properties on a global scale are needed for climate model development and evaluation as well as for climate research. Satellite observations provide these global and long-term cloud observations. From observations in the visible, near-infrared and thermal infrared parts of the electromagnetic spectrum cloud macro-physical properties, such as cloud amount and cloud top height, as well as cloud optical and micro-physical properties such as cloud-top thermodynamic phase, cloud optical thickness and effective radius, which describes the cloud particle size distribution, can be retrieved.

A number of these types of cloud property retrievals and their accompanying global, long-term cloud data sets exist for a range of multi-spectral passive imagers on both polar-orbiting and geostationary satellites. Several of these data sets are included in the Global Energy and Water Cycle Experiment (GEWEX) Assessment of Global Cloud Datasets from Satellites (Stubenrauch et al., 2013). The objective of this assessment is to evaluate their overall quality. Participating cloud data sets include the ATSR-GRAPE based on observations from the Along-Track Scanning Radiometers (ATSRs) and the Advanced ATSR (AATSR) (Sayer et al., 2011), the International Satellite Cloud Climatology Project (ISCCP, 2014) based on observations from imagers on a set of satellites, the Pathfinder Atmospheres Extended (PATMOS-x) (PATMOS-x, 2014) based on observations from the Advanced Very High Resolution Radiometer (AVHRR) on the National Oceanic and Atmospheric Administration (NOAA) satellites and on the Meteorological Operation (MetOp) satellites of the European Organization for the Exploitation of Meteorological Satellites (EUMETSAT), and cloud products from the MODIS Science Team (NASA, 2014b) and MODIS CERES Science Team (NASA, 2014a), using observations from the Moderate Resolution Imaging Spectroradiometer (MODIS) from the National Aeronautics and

Space Administration (NASA) Earth Observing Satellites (EOS) Aqua and Terra. Inter-comparisons were performed on monthly mean, gridded cloud data sets. Results show that differences in average cloud properties can arise due to, e.g., retrieval filtering, ice-water cloud misidentification, assumptions on cloud particle shape and size distribution, and the set of spectral channels and ancillary data used in the retrievals.

To assess the quality of retrieved cloud properties due to algorithm design itself, i.e. not accounting for instrument design, the Cloud Retrieval Evaluation Workshop (CREW) was initiated by EUMETSAT (Roebeling et al., 2013). Level-2 cloud products derived from a set of well-established cloud property algorithms have been collected and inter-compared for pre-defined days against observations from the active instruments Cloud-Aerosol Lidar with Orthogonal Polarization (CALIOP) on Cloud-Aerosol Lidar and Infrared Pathfinder Satellite Observations (CALIPSO), Cloud Profiling Radar (CPR) on CloudSat and Advanced Microwave Scanning Radiometer for EOS (AMSR-E) on Aqua, all part of the the A-train constellation. Participating cloud property algorithms include the Clouds and Earth's Radiant Energy System (CERES) algorithm (Minnis et al., 2011), PATMOS-x including the Daytime Cloud Optical and Micro-physical Properties (DCOMP) algorithm (Walther and Heidinger, 2012), and the Cloud Physical Properties (CPP) algorithm (Roebeling et al., 2006). These kind of studies can reveal strengths and weaknesses for different methods of cloud property retrievals (Hamann et al. (2014)) and has shown that large differences can already arise due to different cloud detection methods. This will in turn also affect temporal and spatial averages of cloud properties for climate studies.

In the frame of the European Space Agency (ESA) Climate Change Initiative (CCI) Cloud project (Hollmann et al., 2013) a 10-year daytime cloud climatology of synergistic AATSR and Medium Resolution Imaging Spectrometer (MERIS), both flying on the Environmental Satellite (Envisat), cloud observations is to be produced. The ultimate objective of the project is to provide long-term coherent cloud property data sets for climate research, taking advantage of the synergy of different earth observation missions. The FAME-C (Freie Universität Berlin AATSR MERIS Cloud) algorithm uses optimal estimation to retrieve a set of daytime cloud properties and their uncertainties on a pixel basis. Originally, MERIS and AATSR were not designed for cloud observations, but together they provide a useful set of channels in the visible, near-infrared and thermal infrared wavelengths for cloud property retrieval. Furthermore, two independent cloud height products are retrieved, first, using AATSR brightness temperatures from two thermal infrared channels and, second, using the MERIS oxygen-A absorption channel. Follow-up instruments Sea and Land Surface Temperature Radiometer

(SLSTR) and Ocean Land Colour Instrument (OLCI) on-board Sentinel-3 (ESA, 2014d), expected to be launched by mid 2015, will have very similar channel settings, making the FAME-C algorithm applicable to their observations as well.

This paper is intended to serve as a reference to the FAME-C algorithm. The structure of the paper is as follows. First, AATSR and MERIS observations are introduced and pre-processing is shortly explained in Sect. 2. Section 3 presents the forward models used in the cloud optical and micro-physical property retrieval, and in both the cloud top temperature retrieval and cloud top pressure retrieval. Also, a short note on auxiliary data is given. Next, Sect. 4 presents an overview of the retrieval scheme, treating the applied inversion technique and listing uncertainty estimates. Sect. 5 shows verification results of the comparison of FAME-C level-2 cloud properties with MODIS-Terra cloud optical and micro-physical properties and cloud top heights derived from ground-based radar observations. Last, a summary and discussion is given.

4.2 Observation data and pre-processing

Instruments

AATSR and MERIS are both imaging multi-spectral radiometers mounted on the polar orbiting satellite Envisat, which was launched in March 2002 and was in operational use until April 2012, providing a 10 years measurement data set. Envisat flies in a sun-synchronous polar orbit around the earth at a mean altitude of 800 km and a 98.5° inclination. It has a repeat cycle of 35 days and the mean local solar time at descending node is 10.00 AM. The MERIS instrument has fifteen spectral channels, which are programmable in position and width within the solar spectral range (400 to 905 nm), and scans the earth with a push-broom method. It has a horizontal resolution of just over 1 km at the sub-satellite point and its field of view, resulting in a swath width of 1150 km, is covered using five identical optical cameras. AATSR has spectral channels in the visible part as well as in the near-infrared and thermal infrared part of the spectrum (channels at 0.55 μm, 0.66 μm, 0.87 μm, 1.6 μm, 3.7 μm, 11 μm, 12 μm). It has a horizontal resolution of 1 km at sub-satellite point and a swath width of 512 km. Due to its conical scanning method it has a dual-view of the earth surface for all spectral channels. More details on both instruments can be found at Llewellyn-Jones et al. (2001); Rast et al. (1999); ESA (2014c).

Collocation and Cloud Screening

Cloud property retrievals are performed for pixels identified as cloudy by a synergistic cloud mask, which is produced using the cloud screening module in the BEAM toolbox (Fomferra and Brockmann, 2005; ESA, 2014a). First, the AATSR observations are collocated with MERIS observations on the MERIS grid (reduced resolution mode; 1200 m x 1000 m) using a nearest neighbor technique. This grid has been chosen because of MERIS's better geo-location. Then, a cloud screening is performed combining a set of neural networks optimized for different cloudy situations and using all AATSR and MERIS channels. Finally, the produced synergy product contains all AATSR and MERIS channels as well as the newly produced cloud mask. It should be noted that the synergy product has a swath width of 493 pixels, which is less than the AATSR swath width of 512 pixels. This is related to collocating the curved AATSR grid with the MERIS grid. Technical details on the collocation and cloud screening method can be found in Gómez-Chova et al. (2008) and Gómez-Chova et al. (2010).

Drift and stray light correction

An improved long-term drift correction is applied to the AATSR reflectances for the visible and near-infrared channels from the second reprocessing as described in Smith et al. (2008). For MERIS measurements the third reprocessing has been used (ESA, 2011). Furthermore, an empirical stray light correction was applied to the reflectance of the MERIS oxygen-A absorption channel (Lindstrot et al., 2010a). For this correction, the spectral smile effect in the MERIS measurements (Bourg et al., 2008), which is the variation of the channel center wavelength along the field-of-view, as well as the amount of stray light in the MERIS oxygen-A absorption channel were determined.

4.3 Forward model

Cloud optical and micro-physical properties

The retrieval of the cloud optical and micro-physical properties cloud optical thickness (COT, τ) and effective radius (REF, r_{eff}) for water and ice clouds, and subsequently also cloud water path (CWP), is based on the DCOMP algorithm and largely follows the approach as described in Walther and Heidinger (2012). The COT-REF pair is retrieved using simultaneous measurements of the AATSR 0.66 μm and 1.6 μm channels. It is based on the assumption that the reflectance in the visible (VIS) mainly depends on COT

due to conservative scattering, while the reflectance in the near-infrared (NIR) mainly depends on the cloud droplet size distribution due to weak absorption. This method is based on work by Nakajima and King (1990) and since has been used in a number of cloud property retrievals (e.g. Nakajima and Nakajma, 1995; Roebeling et al., 2006; Walther and Heidinger, 2012).

Look-up tables for both water and ice clouds consisting of cloud reflectances have been created with simulations from the radiative transfer model Matrix Operator Model (MOMO). MOMO has been developed at the Freie Universität Berlin (Fell and Fischer, 2001; Hollstein and Fischer, 2012) and allows for simulations of radiative transfer in a plane-parallel homogeneous scattering medium with any vertical resolution. The cloud reflectance $R_{c,\lambda}$, at wavelength λ (wavelength dependency will not be used in the text from now on), is given by:

$$R_{c,\lambda} = \frac{\pi * L_{c,\lambda}(\theta_0, \theta, \phi, \tau, r_{eff})}{cos(\theta_0) * F_{0,\lambda}(\theta_0)}, \tag{4.1}$$

where L_c is the radiance reflected by the cloud and F_0 is the incoming solar irradiance at the top of the atmosphere. The radiance L_c is a function of solar zenith angle θ_0, viewing zenith angle θ, and relative azimuth angle ϕ, as well as cloud optical thickness and effective radius. The simulations have been performed assuming a homogeneous cloud and no contribution from the atmosphere as well as the surface, i.e. no gaseous absorption, Rayleigh scattering, aerosol extinction, and zero surface albedo. Then, the reflectance at the cloud top R'_{toc} when including a Lambertian reflecting surface is computed as follows:

$$R'_{toc,\lambda} = R_{c,\lambda} + \frac{\alpha_\lambda * t_{c,\lambda}(\theta_0, \tau, r_{eff}) * t_{c,\lambda}(\theta, \tau, r_{eff})}{1 - \alpha_\lambda * S_\lambda(\tau, r_{eff})}, \tag{4.2}$$

where α is the surface albedo, $t_c(\theta_0)$ and $t_c(\theta)$ are the cloud transmittance in the downward and upward directions, respectively, and S is the spherical albedo.

To compare the measured reflectances at the top of the atmosphere to the forward model results, which are simulated reflectances without consideration of atmospheric extinction processes, the measured reflectances are corrected for atmospheric extinction of radiation due to gaseous absorption and Rayleigh scattering. Other sources of extinction, e.g. aerosols, are not considered. The top-of-cloud reflectance R_{toc} is computed from the

Table 4.1: Atmospheric correction coefficients for AATSR 0.66 μm and 1.6 μm channels.

	a_0	a_1	a_2
0.66 H_2O	$7.86 * 10^{-5}$	$3.9971 * 10^{-3}$	$-1.06 * 10^{-4}$
0.66 O_3	$2.2229 * 10^{-3}$	$3.9840 * 10^{-5}$	$3.9945 * 10^{-8}$
1.6 H_2O	$-2.13 * 10^{-5}$	$9.472 * 10^{-4}$	$-4.0 * 10^{-6}$

measured top-of-atmosphere reflectance R_{toa} as follows:

$$R_{toc,\lambda} = \frac{R_{toa,\lambda} - R_{RS,\lambda}(\theta_0, \theta, \phi, \tau, r_{eff}, p_c)}{t_{a,\lambda}(\theta, \theta_0)}, \qquad (4.3)$$

where R_{RS} is the back-scattered signal due to single scattering events above the cloud, here only Rayleigh scattering in the visible channel is taken into account, and t_a is the two-way atmospheric transmittance above the cloud. The Rayleigh scattering correction is based on Wang and King (1997) and is only performed in the VIS channel. Next to the viewing geometry it depends on cloud albedo α_c, which in turn depends on COT and REF, and Rayleigh optical thickness from cloud top to top of atmosphere, τ_r. The Rayleigh optical thickness is determined assuming a total column Rayleigh optical thickness of 0.044 at surface pressure 1013 hPa (Wang and King, 1997) and scaling it by an estimated cloud top pressure p_c. The atmospheric transmittance above the cloud is determined considering absorption by water vapor (total column water vapor above cloud) and ozone (total ozone in Dobson Units) in the VIS channel and only absorption by water vapor in the NIR channel. A quadratic relationship, and its accompanying coefficients, a_i, between the amount of absorber gas M (here water vapor or ozone) above cloud and the gas transmittance, t_a, also depending on air mass factor (AMF), is determined using a number of MODTRAN simulations. The gas transmission is computed as follows:

$$t_{a,M,\lambda} = e^{-AMF * [a_{0,\lambda} + a_{1,\lambda}M^1 + a_{2,\lambda}M^2]} \qquad (4.4)$$

The atmospheric correction coefficients for the AATSR channels are listed in Table 4.1.

To account for atmospheric absorption below the cloud, the surface albedo in Eq. 4.2 is adjusted to a so called virtual surface albedo α_v by multiplying the surface albedo with the atmospheric transmittance below the cloud. The atmospheric transmittance below the cloud is computed in the same

manner as the atmospheric transmittance above the cloud. For the compu-
tation of the atmospheric transmittance below the cloud a diffuse radiation
field below the cloud is assumed, which means that an air mass factor of 2
is used. Rayleigh scattering is not considered below the cloud. The altitude
of the cloud is roughly estimated using the AATSR 11 μm brightness tem-
perature and atmospheric temperature and pressure profiles from model
data (described in Sect. 4.3). The full forward model looks as follows:

$$R_{toc,v,\lambda} = R_{c,\lambda} + \frac{\alpha_{v,\lambda} * t_{c,\lambda}(\theta_0, \tau, r_{eff}) * t_{c,\lambda}(\theta, \tau, r_{eff})}{1 - \alpha_{v,\lambda} * S_\lambda(\tau, r_{eff})}, \qquad (4.5)$$

Cloud reflectance, cloud transmittance, spherical albedo and cloud albedo
have all been computed for both water and ice clouds. For radiative trans-
fer simulations with water clouds Mie calculations (Wiscombe, 1980) have
been performed beforehand to compute scattering phase functions as well
as single scattering albedo and normalized extinction coefficient, which
serve as input to MOMO. In the Mie calculations a modified gamma-Hansen
cloud droplet size distribution $n(r)$ is assumed (Hansen and Travis, 1974),
where the mode radius equals the effective radius (Hansen and Hovenier,
1974):

$$r_{eff} = \frac{\int_0^\infty r^3 n(r) dr}{\int_0^\infty r^2 n(r) dr}, \qquad (4.6)$$

where r is the cloud droplet radius. A value of 0.1 for the effective vari-
ance is assumed for this droplet size distribution (Minnis et al., 1998). For
ice clouds single-scattering properties described in Baum et al. (2005) have
been used in the radiative transfer simulations. In the LUTs the COT and
REF (in micron) range in log_{10} space from -0.6 to 2.2 in 29 steps and 0.4 to
2.0 in 9 steps, respectively.

From the τ-r_{eff} pair the liquid water path (LWP) for water clouds and
the ice water path (IWP) for ice clouds are determined, assuming a plane-
parallel homogeneous cloud, as follows:

$$CWP = \frac{2}{3} * \tau * r_{eff} * \rho, \qquad (4.7)$$

where ρ is the density of liquid or frozen water (g/m^3). For optically thin
ice clouds the following equation is used to compute ice water path, which

is based on observations of mid-latitude thin ice clouds (Heymsfield et al., 2003):

$$IWP = \tau * \left[\frac{g_0}{r_{eff}} * \left[1 + \frac{g_1}{g_0} \right] \right]^{-1},$$ (4.8)

where g_0 and g_1 are constants with values 0.01256 and 0.725, respectively.

The cloud phase discrimination is done using a simple brightness temperature (BT) threshold of 261 K for the AATSR 11 μm channel, combined with a cirrus detection using the brightness temperature difference BT_{11}-BT_{12} technique (Saunders and Kriebel, 1988) and a maximum reflectance in the visible of 0.25. At 261 K the difference in equilibrium water vapor pressure with respect to ice and water is largest, favoring the growth of ice crystals over super-cooled water droplets for temperatures below 261 K (Pruppacher and Klett, 1997). For the cirrus detection a dynamic clear-sky brightness temperature difference threshold, depending on atmospheric moisture and surface temperature, is used. The clear-sky radiative transfer simulations have been performed with MOMO using a set of standard atmospheric profiles as input taken from McClatchey et al. (1972). From visual inspection of retrieved cloudy scenes the method also often appears to detect cloud edges.

Cloud top heights

Two cloud top height products are retrieved within FAME-C. First, the cloud top temperature (CTT) using AATSR brightness temperatures is retrieved. Second, the cloud top pressure (CTP) is retrieved using the ratio of the MERIS oxygen-A absorption channel over a nearby window channel. Both cloud top height retrievals are then converted to cloud top heights (in km) using the input atmospheric profiles.

AATSR Cloud Top Temperature

The cloud top temperature is retrieved using measurements at the 11 μm channel and the 12 μm channel, at which the extinction coefficient of water is larger. The forward model, assuming a plane-parallel atmosphere, consists of three parts contributing to the top-of-atmosphere radiation in cloudy situations: cloud, surface, and atmosphere. The contribution of the cloud $I_{c,\lambda}$ is given as follows:

$$I_{c,\lambda} = \epsilon_c(\tau, \theta) * B(T_{ct}, \lambda) * t_{ct \to 1, \lambda}(\theta),$$ (4.9)

where ϵ_c is the cloud emissivity, $B(T_c)$ is the Planck function at the temperature of the cloud top T_{ct}, assuming the cloud to be in thermal equilibrium with the surrounding air, and $t_{ct \to 1}$ is the atmospheric transmittance from the cloud top to the top of atmosphere. The cloud emissivity is computed as follows:

$$\epsilon_c = 1 - \exp\left[\frac{-\tau_{ir}}{\cos\theta}\right], \tag{4.10}$$

where τ_{ir} is the cloud optical thickness in the thermal infrared. Here, no multiple scattering is assumed and the thermal infrared cloud optical thickness is computed from the visible cloud optical thickness τ_{vis}, which is taken from the cloud optical and micro-physical property retrieval. The simple relationship $\tau_{ir} = 0.5 * \tau_{vis}$ is used, which is about true for large water and ice particles (Minnis et al., 1993).

The contribution of the surface $I_{s,\lambda}$ is given as follows:

$$I_{s,\lambda} = \epsilon_{s,\lambda} * B(T_s, \lambda) * t_{a,\lambda}(\theta) * t_c(\theta), \tag{4.11}$$

where ϵ_s is the surface emissivity, $B(T_s)$ is the Planck function at the surface temperature T_s, t_a is the transmittance of the atmosphere, and t_c is the transmittance of the cloud. The cloud transmittance is computed from the cloud emissivity with $t_c = 1 - \epsilon_c$. The contribution of the atmosphere at the top of atmosphere $I_{a,\lambda}$ is given as follows:

$$I_{a,\lambda} = \int_{t_{s,\lambda}}^{1} B(T_a, \lambda) dt_\lambda + \left[1 - \epsilon_{s,\lambda}\right] * t_{s,\lambda}(\theta)^2 * \int_{t_{s,\lambda}}^{1} \frac{B(T_a, \lambda)}{t_\lambda(\theta)^2} dt_\lambda, \tag{4.12}$$

where t_s is the total transmittance from surface to the top of the atmosphere, and $B(T_a)$ is the Planck function at the atmospheric temperature T_a of the level with transmittance t. The second term in the equation is of second order and arises from downward radiance reflected upward at the surface. For cloudy layers, the atmospheric transmittance $t_{a,j}$ of layer j is multiplied by the cloud transmittance $t_{c,j}$ to get the total transmittance t at layer j. The vertical extension of the cloud and the vertical distribution of cloud layer transmittance/emissivity values are based on vertical cloud profiles explained in Sect. 4.3. For atmospheric levels below the cloud the atmospheric transmittances are multiplied by the total cloud transmittance t_c. For very thick clouds with cloud emissivities equal to 1, the surface and atmospheric layers below the cloud do not contribute to the top-of-atmosphere radiance.

56

The fast radiative transfer model RTTOV version 9.3 (Saunders et al., 2010; METOffice, 2014) is used to simulate the clear-sky transmission for both AATSR IR channels at a given number of atmospheric levels. As input to RT-TOV are given atmospheric profiles of temperature, water vapor and ozone concentrations, as well as the temperature, water vapor concentration and pressure near the surface. Both the atmospheric profiles and surface properties are obtained from ERA-Interim re-analysis and forecasts (to be described in Sect. 4.3). At the time of development the optical parameter file for ATSR on ERS (version 7) was used. This will lead to a small error in the simulated AATSR brightness temperatures due to slightly different spectral response functions for the IR channels of the two instrument.

MERIS Cloud Top Pressure

The cloud top pressure (CTP) is retrieved using the radiance ratio of the MERIS oxygen-A absorption channel 11 at around 760 nm (L_{11}) and a near-by window channel 10 at around 753 nm (L_{10}), representing an apparent transmittance:

$$t_{o_2} = \frac{L_{11}}{L_{10}}, \tag{4.13}$$

Since oxygen is a well-mixed gas in the atmosphere, the ratio can be used to estimate the average photon path length through the atmosphere. In cloudy situations this average photon path length mainly depends on cloud top pressure.

MOMO radiative transfer simulations have been performed to create a LUT in which the ratio depends on cloud top pressure as well as cloud optical thickness, viewing geometry, surface pressure, and the MERIS channel 11 center wavelength. A US standard atmosphere (McClatchey et al., 1972) is assumed in the simulations. The k-distribution method (Bennartz and Fischer, 2000; Doppler et al., 2014b) is used to compute the absorption coefficients of the atmospheric gases. Information on the position and width of absorption lines is taken from the HITRAN database (Rothman et al., 2009). The CTP ranges from 100 to 1000 hPa in the LUT. For cloud layers below 440 hPa ice crystals are assumed with a fixed effective radius of 40 μm, otherwise water droplets are assumed with a fixed effective radius of 10 μm. A previous sensitivity study (Preusker and Lindstrot, 2009) has shown that the cloud micro-physical properties and the temperature profile account for errors of less than 10 and 20 hPa, respectively, in the MERIS-CTP retrieval and are much smaller than other error sources such as the presence of multi-layer clouds and unknown sub-pixel cloud fraction. For CTP

retrievals above high land surfaces the surface pressure has to be taken into account to prevent underestimation of CTP. For retrievals above oceans a surface pressure of 1013 hPa is assumed. To account for the spectral smile effect in the MERIS measurements, radiative transfer simulations are performed for varying center wavelengths in the oxygen-A absorption channel.

Due to in-cloud scattering the average photon path length is increased. This increase depends on the vertical extinction profile of the cloud. To derive 'realistic' cloud vertical extinction profiles for nine cloud types based on the ISCCP cloud classification (ISCCP), one year (2010) of layer optical thickness's as provided by the CloudSat database is used as described in Henken et al. (2013). The geometrical thickness of each cloud type, i.e., the number of adjacent cloud layers with a thickness of 20 hPa, is taken constant and based on an empirical analysis of a number of CloudSat scenes. The resulting averaged and normalized vertical extinction profiles are shown in Fig. 3.4. It can be seen that for most cloud types lower cloud layers tend to have higher extinction values than upper cloud layers. In the radiative transfer simulations of the MERIS channels 10 and 11 radiances the cloud is divided into a number of cloud layers, each with a thickness of 20 hPa. The appropriate extinction profile, and thus the extinction of each cloud layer, is selected according to the ISCCP cloud classification. this means that the layer cloud optical thickness is different for each cloud layer, while it would be taken constant for all cloud layers when assuming a vertically homogeneous cloud. The total cloud optical thickness is taken from the cloud optical and micro-physical property retrieval.

Auxiliary Data

A set of auxiliary data is needed within the FAME-C algorithm. For the atmospheric correction in the cloud optical and micro-physical property retrieval, atmospheric profiles from ERA-Interim re-analyses (00+00 UTC and 12+00 UTC) and forecasts (00+06 UTC and 12+06 UTC) are used. They are linearly interpolated in time, but kept on the ERA-Interim spatial resolution of 1.125°. The interpolated atmospheric profiles and surface properties also serve as input in the RTTOV clear-sky simulations. Furthermore, the IR land surface emissivities are taken from the UW-Madison Baseline Fit Emissivity Database (Seemann et al., 2008). The cloud optical and micro-physical property retrieval uses the MODIS 16-day composite white-sky surface albedo product (MCD43C3; NASA Land Processes Distributed Active Archive Center (LP DAAC)) on a 0.05°spatial grid as input, while the MERIS-CTP retrieval uses the 2005 monthly mean MERIS-derived land surface albedo product (Muller et al., 2007). To account for pixels that might con-

tain snow-covered surfaces, the MODIS monthly mean snow cover product (MYD10CM; Hall et al. (2006)) on a spatial 0.05°grid is used. Sea ice cover is taken from ERA-Interim. For water surfaces and surfaces containing snow or ice fractions of more than 50 %, fixed surface albedo and surface emissivity values are taken from narrow-band mean surface albedo (Chen et al., 2006) and surface emissivity (Chen et al., 2003) for water and snow/ice surfaces derived from MODIS-Terra data. The surface pressure that serves as input in the MERIS-CTP retrieval is estimated on a pixel basis from the MERIS surface height provided as meta-data in the AATSR-MERIS synergy product. The synergy product also provides for a pixel-based land-sea mask.

4.4 Retrieval scheme

The FAME-C cloud property retrieval is conducted orbit-wise on a pixel basis and in a sequential form. First, preprocessing is performed creating the synergy files with cloud mask as well as extracting auxiliary data. Then, for pixels identified as cloudy during the cloud screening, the cloud optical and micro-physical properties retrieval is performed (DCOMP). Last, two independent cloud top height retrievals are performed (DCHP; Daytime Cloud top Height Properties).

First, cloud top temperature is retrieved using AATSR IR measurements (DCHP-A). Second, cloud top pressure is retrieved using MERIS measurements in the oxygen-A absorption channel and a nearby window channel (DCHP-M). Note, the cloud optical thickness from the cloud optical and micro-physical property retrieval serves as input for both DCHP retrievals. Figure 4.1 gives a schematic overview of the FAME-C algorithm.

Inversion Technique

The retrieval of the cloud parameters is based on the optimal estimation method. This inversion technique allows for the combined use of an a-priori estimate of the most likely solution, $\vec{x}_a$, and the measurements given in the measurement vector $\vec{y}$, to maximize the probability of the retrieved cloud parameters given in the state vector $\vec{x}$. The cloud parameters, their a priori values with uncertainties, and measurements with uncertainties are listed in Table 4.2. Both $\vec{x}_a$ and $\vec{y}$ are weighted by their uncertainty estimates given in the error covariance matrices $\mathbf{S}_a$ and $\mathbf{S}_y$, respectively. In short, the
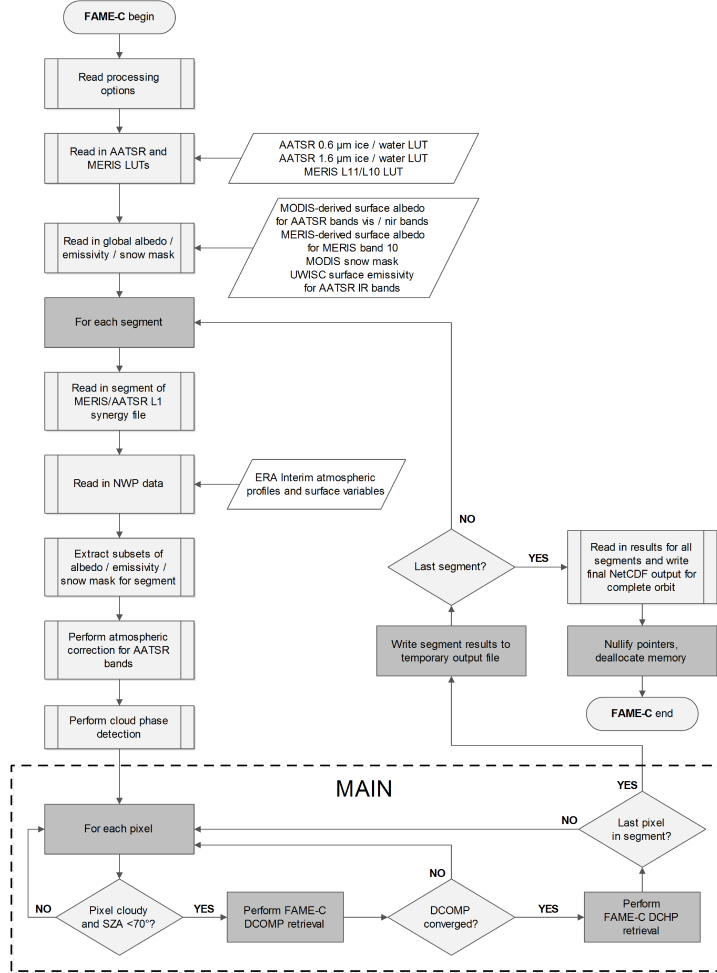
Figure 4.1: FAME-C algorithm flowchart with two main retrieval steps DCOMP (Day-time Cloud Optical and Micro-physical Properties) and DCHP (Daytime Cloud top Height Properties) and input and output data.

inversion technique aims to minimize the retrieval cost function J given as:

$$J(\vec{x}) = \left[\vec{y} - F(\vec{x}, \vec{b})\right]^T \mathbf{S}_y^{-1} \left[\vec{y} - F(\vec{x}, \vec{b})\right] + [\vec{x} - \vec{x}_a]^T \mathbf{S}_a^{-1} [\vec{x} - \vec{x}_a],$$

(4.14)

where $F(\vec{x}, \vec{b})$ is the output of the forward model for state $\vec{x}$ and background state $\vec{b}$. The forward model parameters and their uncertainties are listed in Table 4.3. The background state vector, or forward model parameter vector, includes parameters that are not retrieved, but do affect the retrieval. Due to non-linearity in the forward model the minimization is performed within an iterative process. Here, the Gauss-Newton method is used. A first guess, also listed in Table 4.3, is used to start the iteration. The iteration is terminated when the difference between the error-weighted length of two consecutive state vectors is one order of magnitude smaller than the length of the state vector, or the maximum number of allowed iterations has been reached. The error covariance matrix of the retrieved state $\mathbf{S}_x$ can be computed as follows:

$$\mathbf{S}_x = \left[\mathbf{K}_T \mathbf{S}_y^{-1} \mathbf{K} + \mathbf{S}_a^{-1}\right]^{-1}, \tag{4.15}$$

where $\mathbf{K}$ is the Jacobian matrix describing the sensitivity of F to changes in state parameters. This way, the pixel-based retrievals are accompanied by pixel-based uncertainties.

It has to be noted that the optimal estimation method is built on the assumption that the state parameters and their errors, as well as the observation errors, show a Gaussian distribution and the iteration method assumes that F changes linearly with small changes in the state parameters. To meet these assumptions, the τ-r_{eff} pair is retrieved in a logarithm-based space. An in-depth mathematical description of optimal estimation can be found in Rodgers (2000).

Figure 4.2 shows an example of the cloud mask and retrieved cloud parameters for a cloudy scene above Germany.

Table 4.2: Listed are the variables in the state vector $\vec{x}$, the measurements in the measurement vector $\vec{y}$ (R=reflectance, BT= brightness temperature, L=radiance) and their uncertainties $\vec{y}_{unc}$, and the a priori values in the a priori state vector $\vec{x}_a$ and their uncertainties $\vec{x}_{a\_unc}$, used in the cloud optical and micro-physical cloud properties retrieval (DCOMP) and both cloud top height properties retrievals for AATSR measurements (DCHP-A), and MERIS measurements (DCHP-M). Here, *wat* and *ice* are the water and ice cloud phases, respectively. Note that in DCOMP $\vec{x}_a$ and $\vec{x}_{a\_unc}$ are in $\log_{10}$ space.

alg	$\vec{x}$, (symbol) [unit]	$\vec{y}$: $\vec{y}_{unc}$	$\vec{x}_a$: $\vec{x}_{a\_unc}$
DCOMP	COT (τ)	R 0.66 μm: 4%	wat= 1.0: 2.0, ice= 1.0: 2.0
	REF (r_{eff}) [μm]	R 1.6 μm: 4%	wat= 1.2: 2.0, ice= 1.6: 2.0
DCHP-A	CTT [K]	BT 11 μm: 0.1K	wat= 280K: 40K, ice= 250K: 40K
		BT 12 μm: 0.1K	
DCHP-M	CTP [hPa]	L_{761nm}/L_{753nm}: 0.004%	wat= 800 hPa: 300 hPa, ice=300 hPa: 300 hPa

Table 4.3: Listed are the forward model parameters $\vec{b}$ and their uncertainties $\vec{b}_{unc}$ as well as the first guess $\vec{x}_{guess}$ used in the cloud optical and micro-physical cloud properties retrieval (DCOMP) and both cloud top height properties retrievals for AATSR measurements (DCHP-A) and MERIS measurements (DCHP-M). The cloud optical thickness (COT,τ) uncertainty, τ_{unc}, is taken from the DCOMP results. Misc stands for miscellaneous and is an estimated forward model parameter uncertainty arising from differences in spectral response function of ATSR-2 (assumed in clear-sky RTTOV simulations) and AATSR, and tabular integration. In the cloud top pressure (CTP) retrieval different first guesses are used for low ($>$680 hPa), middle ($>$400 hPa and $<$680 hPa) and high ($<$400 hPa) clouds. To estimate the cloud height level, the previously retrieved cloud top temperature is converted to cloud top pressure using the ERA-Interim temperature profile. Here, α is surface albedo, ϵ_c is cloud emissivity, *wat* and *ice* are the water and ice cloud phases, respectively, $R_{0.66}$ and $R_{1.6}$ are the reflectances in the AATSR 0.66 μm and 1.6 μm channels, respectively, and BT_{11} is the brightness temperature in the AATSR 11 μm channel. Note that in DCOMP $\vec{x}_{guess}$ is in $\log_{10}$ space. * Only performed for pixels with $\tau < 8$.

alg	$\vec{x}$	$\vec{b}$: $\vec{b}_{unc}$	$\vec{x}_{guess}$
DCOMP	COT	α: 0.02 & CTP: 20 hPa	wat= 1+R$_{0.66}$, ice= 1+R$_{0.66}$
	REF		wat= 1.2, ice= 1.6-R$_{1.6}$
DCHP-A	CTT	ϵ_c*: $\tau_{unc}/2cos(\theta)*exp(-\tau/2cos(\theta))$ & Misc: 0.5K	BT$_{11}$
DCHP-M	CTP	α*: 0.02 & τ*: τ_{unc}	low= 850 hPa, middle= 540 hPa, high= 300 hPa
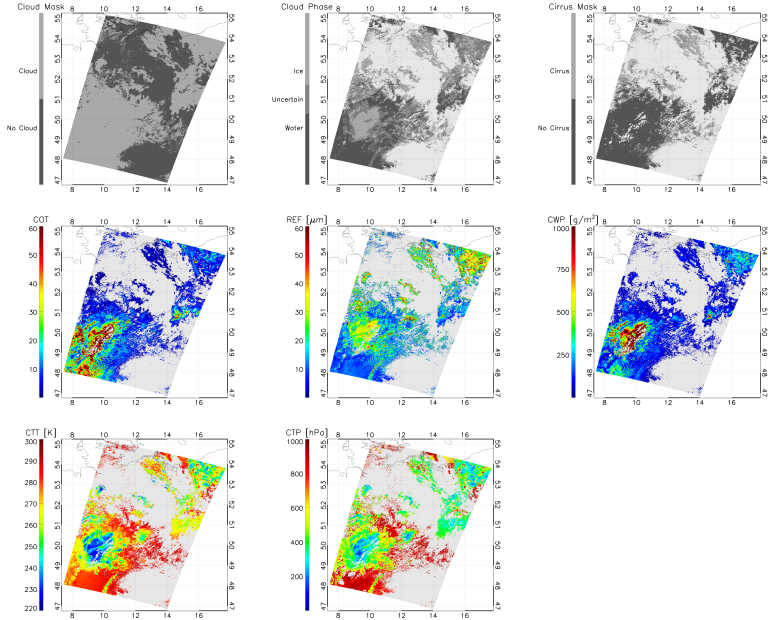
Figure 4.2: Example of the FAME-C cloud mask, cloud phase mask, cirrus mask and retrieved cloud optical and micro-physical as well as macro-physical properties for a synergy AATSR-MERIS orbit segment above Germany on 21 July 2007.

Uncertainty estimates

The reliability of the error covariance matrix of the retrieved state depends on the reliability of the characterization of $\mathbf{S}_y$ and $\mathbf{S}_a$, i.e. on the estimated uncertainties in the measurements and the a-priori state. Also, forward model parameter uncertainties, which are uncertainties caused by non-retrieved parameters in the forward model, can be added to the measurement uncertainties to form a combined measurement error covariance matrix $\mathbf{S}_\epsilon$ as follows:

$$\mathbf{S}_\epsilon = \mathbf{S}_y + \mathbf{K}_B \mathbf{S}_B \mathbf{K}_B^T, \tag{4.16}$$

where $\mathbf{S}_B$ is the forward model error covariance matrix, and $\mathbf{K}_B$ is the Jacobian matrix, which describes the sensitivity of F to changes in the forward model parameters.

64

At the moment, all error covariance matrices only have non-zero values for the diagonal elements, meaning that correlations between uncertainties are neglected. Furthermore, we do not make use of an independent source that can provide for well-characterized a-priori knowledge of the cloud parameters and their uncertainties. Therefore, the estimated uncertainties are set to high values, shown in Table 4.2. This will reduce the constraint of the a-priori estimate $\vec{x}_a$ on possible solutions $\vec{x}$. Estimated uncertainties in the measurements (based on ESA (2014b) for AATSR) as well as for a set of forward model parameters are listed in Table 4.2 and Table 4.3, respectively. For certain pixels that have reached convergence, we take into account the uncertainties due to the rather simple cloud phase discrimination. This is realized by adding the difference in forward model values between the water cloud and ice cloud, keeping everything else constant, to the measurement error covariance matrix. This is done for pixels with 11 μm brightness temperatures between 245 K and 273 K and where the reflectance pair 0.66 μm-1.6 μm lies within both the water and ice cloud LUT. Figure 4.3 shows the atmospheric corrected 0.66 μm and 1.6 μm reflectances for cloudy pixels from the scene as shown in Fig. 4.2 together with the AATSR LUT reflectances for a mean viewing geometry and surface albedo, as function of cloud optical thickness and effective radius and for both water and ice clouds. In green are shown the cloudy pixels with an uncertain retrieved cloud phase located in the overlapping area of the water and ice LUT. According to our forward models in this area we can have both large water droplets and small ice crystals or a mix of both.

The retrieved uncertainties for all successfully retrieved cloudy pixels, which are defined as cloudy pixels that converged within the allowed maximum number of iterations and with cost < 20, for all orbit segments covering a region in Germany as presented in Fig. 5.1 (GER), and for each retrieved cloud phase, are shown in Fig. 4.4. For COT, REF and CWP, the mean relative uncertainty is lowest for about 10, 10 μm and 80 g/m^2, respectively, and increases for both decreasing and increasing values of the accompanying cloud properties. For both CTT and CTP the relative uncertainty decreases for decreasing cloud top height. The shapes can be largely explained as follows. For thin clouds the surface albedo uncertainty has a large contribution as well as the uncertainty in cloud emissivity. For very thick clouds the reflectance in the visible is less sensitive to cloud optical thickness leading to an increased uncertainty in COT. The uncertainties in cloud emissivity and COT are propagated to uncertainties in CTT and CTP, respectively. In general, the relative uncertainty is highest for pixels with uncertain cloud phase and lowest for water cloud pixels.

Uncertainties in ERA-Interim atmospheric profiles are neglected. Also,
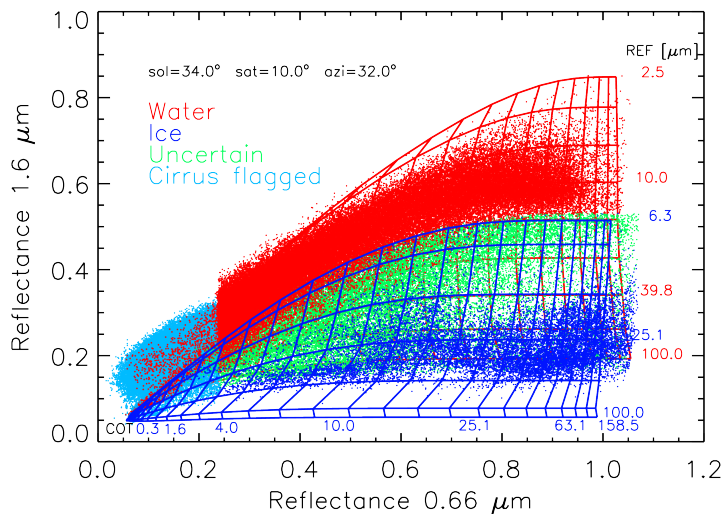
Figure 4.3: AATSR atmospheric corrected reflectance in visible and near-infrared
(dots) for water/ice/uncertain/cirrus pixels from the scene shown in Fig. 4.2. The
two grids represent the forward modeled AATSR reflectances for water (red) and ice
(blue) clouds, assuming mean viewing geometry and surface albedo values for the
scene.

uncertainties in the radiative transfer simulations, chosen cloud micro-
physical models, and due to interpolations in the LUTs are not considered
at present.

Last, the forward model assumes fully cloudy pixels with plane-parallel
clouds either consisting of water droplets or ice crystals. The impact of sub-
pixel clouds, 3-dimensional effects (e.g. cloud shadows), multi-layer cloud
situations, and mixed-phase clouds, needs to be studied in the future for
an improved uncertainty estimate budget.

4.5 Summary

With the FAME-C algorithm daytime cloud optical and micro-physical prop-
erties and macro-physical properties and their uncertainties are retrieved
on a pixel basis. The AATSR and MERIS observations and accompanying for-
ward models are presented as well as the auxiliary data used in FAME-C. As

part of the pre-processing, AATSR and MERIS observations are collocated and cloud screening is performed using all channels from both instruments. Next, for all cloudy pixels a simple cloud phase detection is performed. The retrieval scheme itself consists of two main steps and is carried out on a pixel-basis for those pixels identified as cloudy by the cloud mask. First, the cloud optical and micro-physical property retrieval is performed using an AATSR visible and near-infrared channel, resulting in retrieved cloud optical thickness and effective radius. From those also cloud water path is computed. Separate forward models have been developed for water and ice clouds. Second, the cloud top height retrievals are performed using observations from AATSR thermal infrared channels for the cloud top temperature retrieval and observations from the MERIS oxygen-A absorption channel for the cloud top pressure retrieval. Especially the MERIS cloud top pressure retrieval depends on the assumed vertical extinction profile of the cloud. Therefore, in both cloud top height retrievals vertically inhomogeneous cloud profiles are assumed derived from one year of CloudSat data. The cloud optical thickness previously retrieved serves as input for both cloud top height retrievals.

The use of the optimal estimation method in the retrieval scheme allows for a propagation of a-priori knowledge and the uncertainty estimates of the measurements and forward model parameters into the final retrieval of the cloud property and its uncertainty. At this point, the contribution of the a-priori estimate in FAME-C to the retrieved state and its uncertainty is negligible. Shown are estimates of uncertainties in the measurements and forward model parameters. Both the inclusion of independent a-priori knowledge and a more extended uncertainty estimate budget and assessment are envisaged in the future to fully exploit the advantages of the optimal estimation method.
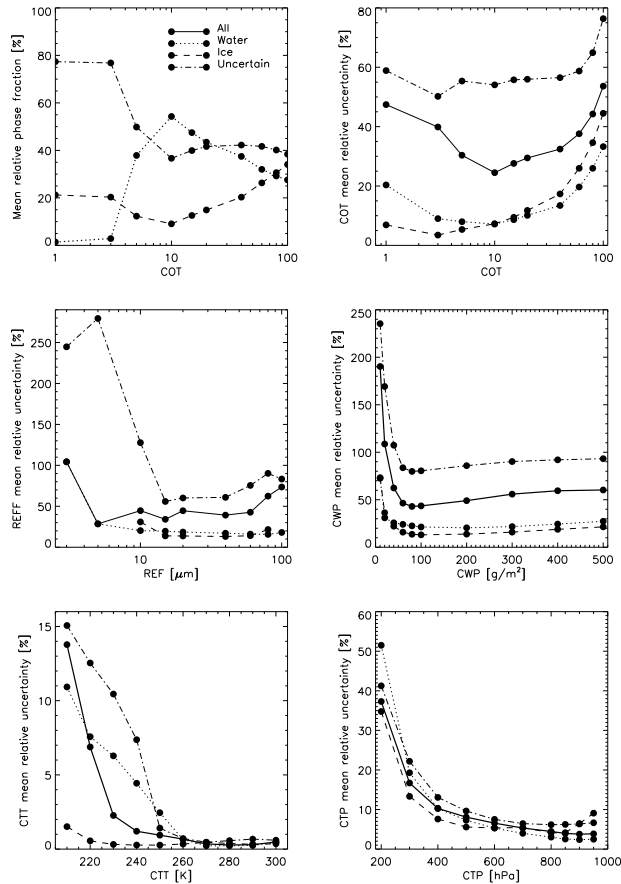
Figure 4.4: Histograms of the mean relative phase fraction and mean relative uncertainty estimates for FAME-C cloud properties cloud optical thickness (COT), effective radius (REF), cloud water path (CWP), cloud top temperature (CTT), and cloud top pressure (CTP), for all successfully retrieved cloudy pixels (converged and cost < 20) for orbit segments covering the region in Germany between latitudes 9° and 14° and longitude 49° and 54° (presented in Fig. 5.1 as GER) for the years 2007-2009. Results are shown separately for the three cloud phases, water, ice and uncertain, and for all cloudy pixels.

5
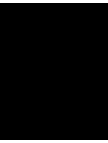
Evaluation of the FAME-C cloud properties

Abstract Within the frame of the European Space Agency (ESA) Climate Change Initiative (CCI) project, the first global cloud property retrievals have been conducted for the years 2007–2009. For this time period, verification efforts are presented, comparing, for four selected regions around the globe, FAME-C cloud optical and micro-physical properties to cloud optical and micro-physical properties derived from measurements of the Moderate Resolution Imaging Spectroradiometer (MODIS) on the Terra satellite. The results show a reasonable agreement between the cloud optical and micro-physical property retrievals. Biases are generally smallest for marine Stratocumulus clouds: −0.28, 0.41 μm and −0.18 g/m^2 for cloud optical thickness, effective radius and cloud water path, respectively. This is also true for the root-mean-square deviation. Furthermore, both cloud top height products are compared to cloud top heights derived from ground-based cloud radars located at several Atmospheric Radiation Measurement (ARM) sites. FAME-C mostly shows an underestimation of cloud top heights when compared to radar observations. The lowest bias of −0.3 km is found for AATSR cloud top heights for single-layer clouds, while the highest bias of −3.0 km is found for AATSR cloud top heights for multilayer clouds. Variability is low for MERIS cloud top heights for low-level clouds, and high for MERIS cloud top heights for mid-level and high-level single-layer clouds, as well as for both AATSR and MERIS cloud top heights for multilayer clouds.

Sect. 5.2 and 5.3 of this chapter are largely based on Sect. 5-6 of Carbajal Henken et al. (2014)

5.1   Introduction

The FAME-C algorithm was applied to the synergistic AATSR and MERIS measurements from the years 2007-2009, for daytime cloud observations with solar zenith angles below 70°.

To get confidence in the performance of satellite cloud property retrievals, and assess situations for which the retrievals are problematic, several validation exercises are performed. Validation is the assessment of the quality of the data. The accuracy can be described quantitatively in terms of bias and root mean square deviation. The precision of the data depends on the data itself and is, e.g., affected by the sampling frequency of the measurements. The validation exercise is done by comparing the retrieved cloud properties to cloud properties retrieved from independent measurements. These reference data sets can include cloud properties from well-established satellite retrievals, that themselves have been thoroughly validated and its accuracy and known issues are well documented. Also ground-based observations serve as reference data sets. Since each dataset has it's own strengths and weaknesses, depending on instrument characteristics and retrieval method, hardly any can be considered to represent the 'ground truth' in all (cloudy) situations. Therefore, also the terms evaluation and comparisons are used in the validation process.

The evaluation is performed for level-2 as well as level-3 cloud products. Level-2 cloud products consist of instantaneous retrievals on the native instrument projection, the orbit swath. Level-3 cloud products are derived from the level-2 data by mapping the data to an equal-angle grid with spatial resolution of 0.5° x 0.5° and simply computing per grid cell the arithmetic mean of all collected successful retrievals, for each cloud property. The monthly means thus represent in-cloud means. Successful retrievals are selected based on a convergence criterion and an empirical cost threshold.

5.2   Level-2 comparisons

Comparison to MODIS-Terra level-2 cloud optical and micro-physical properties

The comparison of the FAME-C level-2 cloud optical and micro-physical properties to the MODIS-Terra level-2 cloud optical and micro-physical properties (MOD06 collection-5 cloud products) is performed for four selected regions as shown in Fig. 5.1. For each region all available orbit segments of both Envisat and Terra are collected. Overpasses of the satellites
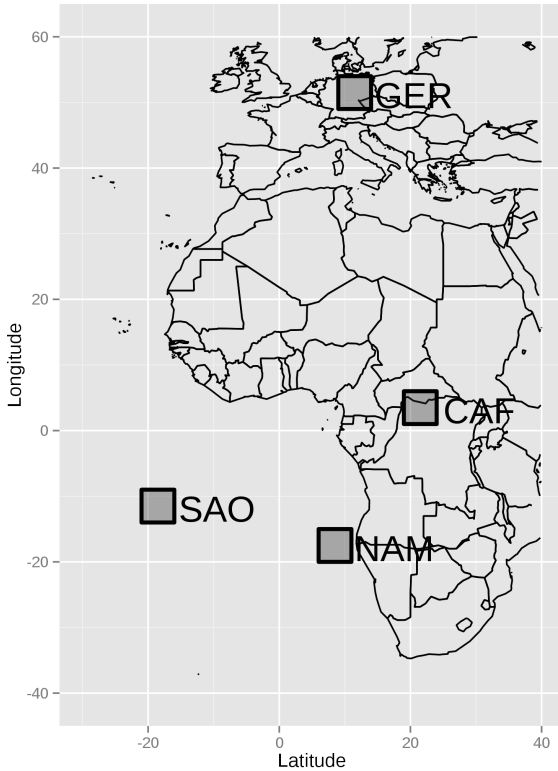
Figure 5.1: Map showing four regions where Level-2 based comparisons between FAME-C and MODIS-Terra cloud properties are conducted for the years 2007-2009. SAO = Southern Atlantic Ocean, NAM = Coast of Namibia, CAF = Central Africa, GER = Germany.

Terra and Envisat do not necessarily occur on the same days. Therefore, no pixel-based comparison is possible. From all selected cloudy pixels within the region and within one month, monthly means and standard deviations are produced for each of the cloud optical and micro-physical properties.

For both, only cloudy pixels with satellite viewing angles of $< 21.6°$, which is the maximum AATSR satellite viewing angle, and solar zenith angles of $< 70°$, are considered. For MODIS-Terra level-2, the effective radius is limited to 30 μm for water clouds. In this comparison this is also done for FAME-C

effective radius for water clouds. Furthermore, for the MODIS cloud optical and micro-physical properties cloudy pixels with a general assessment set to *Useful* according to the quality flag (Quality Assurance at 1 km Resolution) are selected. For FAME-C successfully retrieved cloudy pixels, as defined in Sect. 4.4, are selected.

Figure 5.2 shows the frequency distribution of COT, REF and CWP for all retrieved cloudy pixels in the time period 2007-2009 for both FAME-C and MODIS-Terra for two selected regions GER and NAM as presented in Fig. 5.1. Also, a distinction in cloud phase is made. Generally, the overall distributions agree well with similar shapes and peaks located around similar values. Especially for NAM this is expected since one cloud regime, marine Stratocumulus clouds, dominates this region. Differences become larger when only considering one specific cloud phase. For NAM both FAME-C and MODIS-Terra agree that almost all pixels consist of the water cloud phase. For both regions, FAME-C has a larger number of pixels with cloud phase uncertain. A major difference is the sharp peak at low COT values for FAME-C, mainly consisting of ice phase. From visual inspection of several scenes it is assumed that this is due to pixels misidentified as cirrus clouds by the cirrus detection method and the peak vanishes when these pixels are not considered. Consequently, the peak CWP is shifted towards lower values for FAME-C. The FAME-C REF values agree very well with the MODIS-Terra REF values for NAM. In GER, the second peak in the MODIS-Terra REF arising from the ice cloud phase is not visible in FAME-C REF.

Table 5.1 lists for each region and cloud property the bias and root mean square deviation (RMSD) computed from the monthly means in the 3-year time period. They have been computed for all successfully retrieved cloudy pixels (All), and separately, for cloudy pixels identified as water cloud (Wat), ice cloud (Ice) and with cloud phase uncertain (Unc). The cloud fraction here is defined as the cloud fraction which only considers successfully retrieved cloudy pixels, so those pixels contributing to the statistics of the cloud optical and micro-physical properties. The cloud phase fractions are considered relative to this overall retrieval cloud fraction. It should be emphasized that the cloud fractions and the fraction of clouds with a specific phase, in particular cloud phase uncertain, can be quite different for FAME-C and MODIS-Terra, and consequently this will affect the statistics of the other cloud properties.
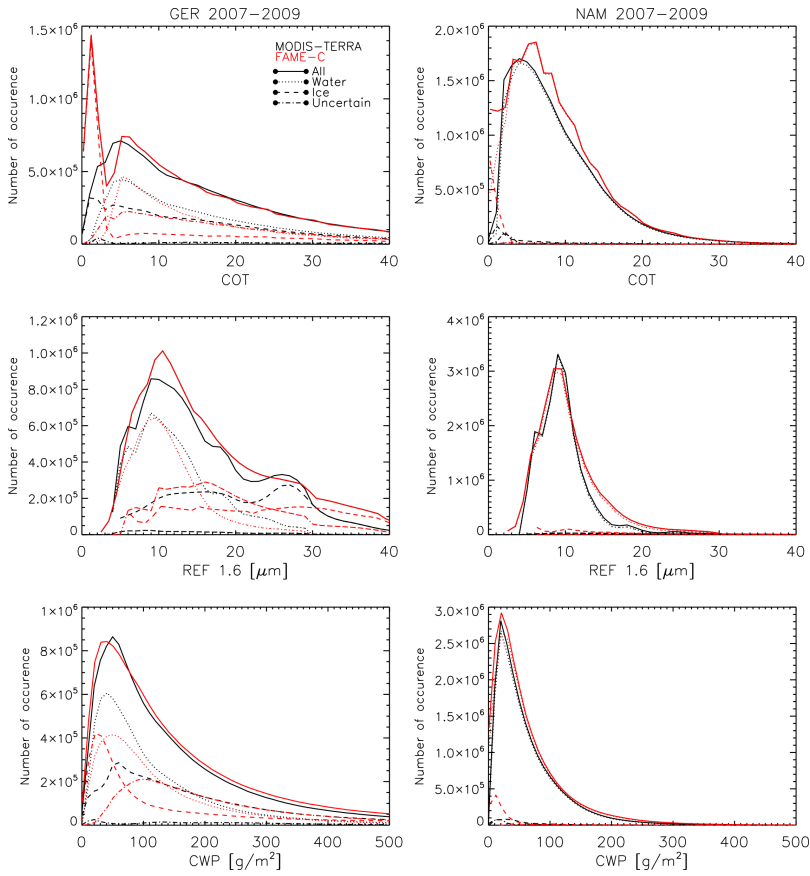
Figure 5.2: Frequency histograms of the pixel-based retrieved cloud optical and micro-physical properties* of FAME-C and MODIS-Terra for the GER and NAM regions as presented in Fig. 5.1. * Cloud optical thickness (COT), effective radius using channel 1.6 μm (REF16) and cloud water path (CWP).

73

Table 5.1: Results of the comparison with monthly mean MODIS-Terra cloud optical and micro-physical properties for 4 regions as presented in Fig. 5.1. Performed for all successfully retrieved cloudy pixels (All), and separately for water cloud pixels (Wat), ice cloud pixels (Ice), and cloudy pixels with uncertain phase (Unc), for cloud properties cloud fraction (CF), cloud optical thickness (COT), effective radius (REF), cloud water path (CWP). REF16 is the MODIS-Terra effective radius retrieved using the 1.6 μm channel. RMSD is root mean square deviation.

		Bias				RMSD			
		All	Wat	Ice	Unc	All	Wat	Ice	Unc
CAF	CF [%]	-1.87	-10.13	-1.95	21.83	12.45	16.24	6.73	22.87
	COT [1]	-1.54	0.58	-3.73	-2.70	4.84	2.08	7.40	7.52
	REF [μm]	0.07	-1.49	0.92	0.28	3.48	1.95	4.10	2.45
	REF16 [μm]	-1.06	-3.11	0.42	0.21	3.56	3.33	4.13	2.03
	CWP [g/m^2]	21.62	4.61	29.05	2.48	83.70	19.11	111.78	75.29
GER	CF [%]	4.70	-11.97	-2.39	29.81	15.59	17.26	9.66	33.82
	COT [1]	-4.57	-3.02	-9.70	-3.03	6.20	5.80	11.91	11.18
	REF [μm]	2.26	0.09	4.50	0.43	3.14	1.38	5.61	3.61
	REF16 [μm]	1.64	-1.01	4.18	1.10	2.78	1.90	5.83	3.04
	CWP [g/m^2]	0.45	-8.39	-40.89	11.31	40.39	35.27	107.55	86.28
NAM	CF [%]	7.57	-2.41	0.08	0.28	12.98	6.08	0.48	2.22
	COT [1]	-0.60	-0.28	-4.94	7.95	1.38	1.27	7.06	10.52
	REF [μm]	-0.31	-0.47	1.59	3.68	1.33	1.34	5.48	5.29
	REF16 [μm]	0.65	0.41	3.60	4.71	1.35	1.18	6.45	6.21
	CWP [g/m^2]	-1.95	-0.18	-27.91	115.42	13.62	14.46	47.44	141.66
SAO	CF [%]	14.23	-1.77	0.26	1.25	16.17	8.30	1.17	2.51
	COT [1]	-1.10	-0.56	-3.57	1.96	1.75	1.43	4.38	5.31
	REF [μm]	1.11	1.11	-1.44	4.38	2.41	2.18	7.04	6.58
	REF16 [μm]	2.00	1.80	2.05	5.38	2.70	2.39	6.92	7.18
	CWP [g/m^2]	-0.28	5.20	-28.78	66.98	17.25	17.16	44.56	88.68

For three regions FAME-C shows an overall cloud fraction that is higher than the MODIS-Terra overall cloud fraction (positive bias), especially for the regions over the ocean (NAM and SAO). This may partly be explained by the clear-sky restoral in the MODIS-Terra cloud property retrieval and likely a more strict quality assessment than in FAME-C. The relative water cloud fraction is usually lower for FAME-C, while the uncertain cloud fraction is higher for FAME-C. Generally, the overall tendency is that FAME-C shows lower COTs and higher REFs. Especially noticeable is the COT negative bias for GER. This can be attributed to a large number of optically thin ice clouds retrieved with FAME-C, but not with MODIS-Terra. First inspections have revealed that this is due to misidentified cirrus clouds, which, through visual inspection, appear to be mainly cloud edges. Neglecting those pixels reduces the overall COT, REF, and REF16 biases to -1.92, 1.01 μm, and 0.45 μm, respectively, but increases the CWP bias to 25.20 g/m^2.

The bias between the REF where both FAME-C and MODIS-Terra retrieved REF using the 1.6 μm channel (REF16) is not necessarily smaller than the bias when MODIS-Terra uses the 2.1 μm channel (REF). The NAM region is dominated by marine Stratocumulus clouds, which are relatively horizontally homogeneous and sub-adiabatic (e.g., Pawlowska and Brenguier, 2000). An adiabatic cloud shows an increasing REF with height. The penetration depth at 1.6 μm is larger than at 2.1 μm and would result in a lower retrieved effective radius assuming an adiabatic cloud. Therefore, in that case a negative bias would be expected when comparing the FAME-C REF retrieved using 1.6 μm and MODIS-Terra REF using 2.1 μm. When comparing both REF retrievals at 1.6 μm a slight positive bias is found. Retrievals of REF using different near-infrared channels can however also be affected differently by, e.g., 3-d radiative effects (e.g., Zhang et al., 2012), which makes interpretation of small differences difficult. The CWP bias is largest for the CAF region. This is however also the region where deep convection takes place which can result in very high CWP values. Mostly, biases are largest for pixels with uncertain cloud phase followed by the ice cloud phase. This is also true for the root mean square deviation.

It should be noted that the Terra satellite flies in a sun-synchronous near-polar orbit with a mean local solar time of 10.30 AM at descending node, which is half an hour later than the Envisat satellite. Slightly shifted observation times as well as different viewing geometry can also contribute to differences in mean cloud properties.

Comparison to cloud top heights derived from ground-based radar observations

The comparison of FAME-C cloud top height products to cloud top heights derived from ground-based observations is performed at the Atmospheric Radiation Measurement (ARM) program's sites in the Southern Great Plains (SGP), Tropical Western Pacific (TWP) and North Slope Alaska (NSA). The active remote sensing of clouds (ARSCL) product provides cloud boundary heights, i.e., cloud base height and cloud top height, based on Millimeter Cloud Radar (MMCR) and Micropulse Lidar (MPL) data (Clothiaux et al., 2000). The cloud boundaries are provided at a vertical resolution of 45 m, a temporal resolution of 10 s, and for up to 10 cloud layers.

For the comparison the dates and times of the Envisat overpasses at each ARM site are determined. For each overpass mean and standard deviation of both FAME-C cloud top height products are computed for a 9 by 9 pixel box centered around the pixel that matches best with the ARM site latitude and longitude values. Before doing so, parallax correction was performed for cloudy pixels. The mean ARSCL cloud top height is computed from cloud top heights within a 5-minute period centered at the Envisat overpass time. Here, the ARSCL cloud top height is defined as the height of the highest cloud layer. The cases were selected based on the following three criteria. First, at least 75 % of the pixels in the FAME-C 9 by 9 pixel box show a successful cloud top height retrieval for either AATSR or MERIS measurements. Second, for all time steps within the 5-minute period a ARSCL cloud top height is determined by the MMCR. Third, the standard deviation of both FAME-C and ARSCL cloud top heights is less than 1 km. This results in 115 cases for AATSR and 90 for MERIS. We assume this difference in cases between both FAME-C cloud top height retrievals to be partly related to the fact that at the moment the MERIS cloud top pressure retrieval tends to fail more often than the AATSR cloud top temperature retrieval. This is related to the use of the different cloud vertical extinction profiles derived from CloudSat data for different cloud types in the radiative transfer simulations used to create the MERIS LUT and leads to jumps in the LUT at the cloud type transitions. It is envisaged to deal with this issue in future versions of FAME-C.

Figure 5.3 shows the comparison of AATSR and MERIS cloud top heights to the ARSCL cloud top heights for single-layer and multi-layer cloud cases. Single-layer clouds are defined as cases where at least 80 % of the radar observations in the 5-minute time period only show one cloud layer. Multi-layer cloud cases are defined as cases where in the ARSCL product at least two cloud layers exist with a minimum distance of 1 km between the cloud
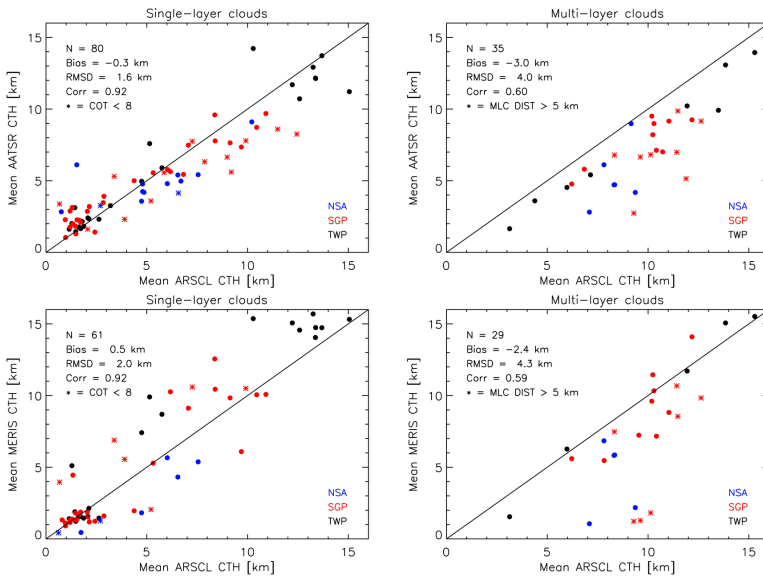
Figure 5.3: Results of the comparison of AATSR (top) and MERIS (bottom) mean cloud top height products with mean cloud top heights derived from radar observations at ARM sites for single-layer clouds (left) and multi-layer clouds (right). For FAME-C the mean was computed from a 9 by 9 pixel box, for radar the mean was computed from all selected observations within a 5-minute time period centered at the Envisat overpass time.

top height of the lower cloud layer and the cloud base height of the upper cloud layer, for at least 80 % of the radar observations in the 5-minute time period.

For single-layer clouds there is an overall small negative bias of -0.3 km found between AATSR and ARSCL cloud top heights. Taking into account only the single-layer cloud cases with ARSCL cloud top heights larger than 3.5 km, i.e., the mid-level and high-level clouds, the bias is -1.1 km with a RMSD of 1.9 km. This negative bias falls within the expected range of a few kilometers, since the retrieved cloud top temperature is rather the temperature at a height one or more optical depths into the cloud. The cloud top height computed from the retrieved cloud top temperature therefore represents the radiometric height. Even for deep convective clouds, the IR radiometric height may lie a few kilometers below the physical cloud top (Sherwood et al., 2004). Minnis et al. (2008) found that for optically thick

ice clouds the difference in IR radiometric height and cloud top heights derived from CALIOP data depends on the ice water content and its vertical profile, i.e., cloud vertical extinction profile, at the top of the cloud. For the single-layer clouds below 3.5 km the bias is 0.7 km with a RMSD of 1.3 km. An overestimation of cloud top height for low-level clouds can occur in cases where the cloud top temperature is assigned to the wrong height level or temperature inversions that are not represented accurately in the modeled temperature profiles.

The overall positive bias of 0.5 km between MERIS and ARSCL cloud top heights for single-layer clouds can be mainly attributed to cases with midlevel and high-level clouds. For those clouds also the variability is large with a RMSD of 2.8 km for cases with ARSCL cloud top heights larger than 3.5 km. This shows that, on the one hand, by introducing the inhomogeneous cloud vertical extinction profiles for nine cloud types in the MERIS cloud top pressure retrieval, the large positive/negative bias found for cloud top pressures/cloud top heights retrievals assuming homogeneous cloud vertical extinction profiles appears to be eliminated. On the other hand, large scatter is introduced, since large variability in real cloud vertical extinction profiles exist. An underestimation/overestimation of MERIS cloud top pressures/cloud top heights may occur due to the fact that the radar on CloudSat does not detect small ice particles, therefore leading to an underestimation of extinction in upper cloud layers in the nine computed average extinction profiles. For low-level clouds variability and bias are generally small. For both AATSR and MERIS single-layer cloud cases it is not evident to see that differences in cloud top heights between FAME-C and ARSCL is larger for optically thin clouds (mean cloud optical thickness < 8) than for optically thick clouds.

Both MERIS and AATSR cloud top heights for multi-layer clouds show higher biases and RMSDs, and lower correlations than the cloud top heights for single-layer clouds. A few cases showing large deviations are identified as cases where there is a minimum distance of 5 km (mlc dist > 5) between two cloud layers, possibly representing high, thin cirrus clouds overlaying a low-level water cloud. In those cases the retrieved cloud top height is expected to be below the height of the upper cloud layer. Interestingly, the MERIS cloud top heights show a smaller negative bias than the AATSR cloud top heights, though the RMSD is high and the number of cases is relatively small. Due to in-cloud scattering of photons in the visible channels and mainly absorption of photons in the IR channels, the AATSR cloud top height is expected to be closer to the height of the upper cloud than the MERIS cloud top height. An in-depth study is needed to assess the differences in AATSR and MERIS cloud top height retrievals in multi-layer cloud cases and
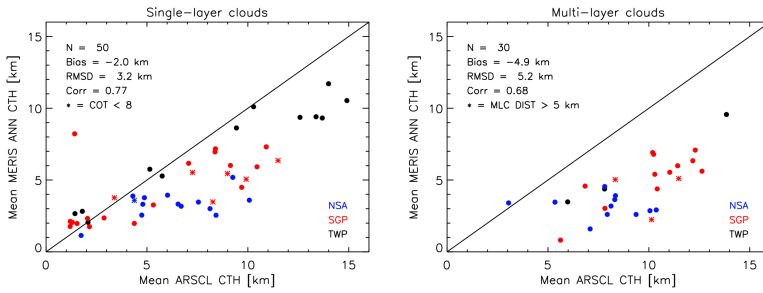
Figure 5.4: Results of the comparison of MERIS-ANN mean cloud top height products with mean cloud top heights derived from radar observations at ARM sites for single-layer clouds (left) and multi-layer clouds (right). For MERIS-CTH ANN the mean was computed from a 9 by 9 pixel box, for radar the mean was computed from all selected observations within a 5-minute time period centered at the Envisat overpass time.

cases with vertically extended clouds.

As a reference, the same validation was performed for a former MERIS cloud top pressure retrieval with a cloud mask (Merheim-Kealy et al., 1999; Fischer et al., 2010), which were developed using Artificial Neural Networks (ANNs). Almost all channels are used as well as information on the sun-satellite viewing geometry, and surface albedo. The surface albedo and atmospheric profiles for cloud top height conversion were taken from the same databases as used in FAME-C. The MERIS-ANN cloud top height shows a negative bias for higher clouds and greater for multi-layer clouds. A slight overestimation is apparent for low-level clouds. When comparing to the results shown in Fig. 5.4, it is clearly visible that MERIS-ANN on average retrieves lower cloud top heights than FAME-C. Comparing the FAME-C MERIS and MERIS-ANN cloud top heights, biases of 2.2 km and 2.3 km, and correlations of 0.93 and 0.88, were found for single-layer clouds and multi-layer clouds, respectively. A large part of the differences can likely be attributed to differences in assumed cloud vertical profiles, though they might also rise from differences in retrieved cloud optical thickness and a different cloud masking method. Note, the set of cases found are not identical to the ones shown in Fig. 5.3.

5.3 Summary and outlook: level-2 comparison

A comparison to MODIS-Terra monthly means derived from level-2 cloud products for four selected regions was performed for cloud fraction, cloud phase, and the cloud optical and micro-physical properties. Results show an overall good agreement between FAME-C and MODIS cloud optical and micro-physical properties. Differences do become larger when looking at biases and root mean square deviations for one specific cloud phase. The comparison of the FAME-C cloud top height products and cloud top heights derived from a ground-based cloud radar reveal an underestimation of FAME-C cloud top height, except for AATSR cloud top heights for low-level single-layer clouds and MERIS cloud top heights for mid-level and high-level single-layer clouds. For single-layer clouds variability is clearly higher for mid-level and high-level clouds than for low-level clouds. The bias and root mean square deviation are higher for multi-layer clouds than for single-layer clouds, while correlation is clearly lower. For in-depth FAME-C cloud top height retrieval evaluations, the comparisons will be extended to CloudSat and CALIPSO observations of cloud top heights for scenes where Envisat and A-train have matching overpasses in space and time.

Ongoing FAME-C retrieval developments and verifications, taking place within phase 2 of the ESA Climate Change Initiative Cloud project, focus on a more advanced cloud phase retrieval, an improved cirrus cloud detection, a separate forward model for multi-layer cloud situations, and extended and improved uncertainty estimates. One of the main topics of interest is the exploitation of the difference in sensitivity of the independent AATSR and MERIS cloud top height retrievals to distinct cloud layers and relating these differences in retrieved cloud top heights to the characterization of cloud vertical distribution. Furthermore, it is planned to adapt FAME-C to retrieve all cloud properties at once resulting in a physically more consistent retrieval, i.e., all resulting retrieved cloud properties are consistent with all measurements. Further ongoing work includes verification efforts on larger spatial scales, comparisons of seasonal and inter-annual variations, and comparisons to other satellite-derived cloud properties as well as cloud properties derived from ground-based observations.

5.4 Level-3 comparisons

Comparison to MODIS-Terra level-3

For the level-3 comparisons to MODIS cloud products, the MODIS-Terra gridded atmosphere monthly global product (MOD08_M3, Collection 5.1)
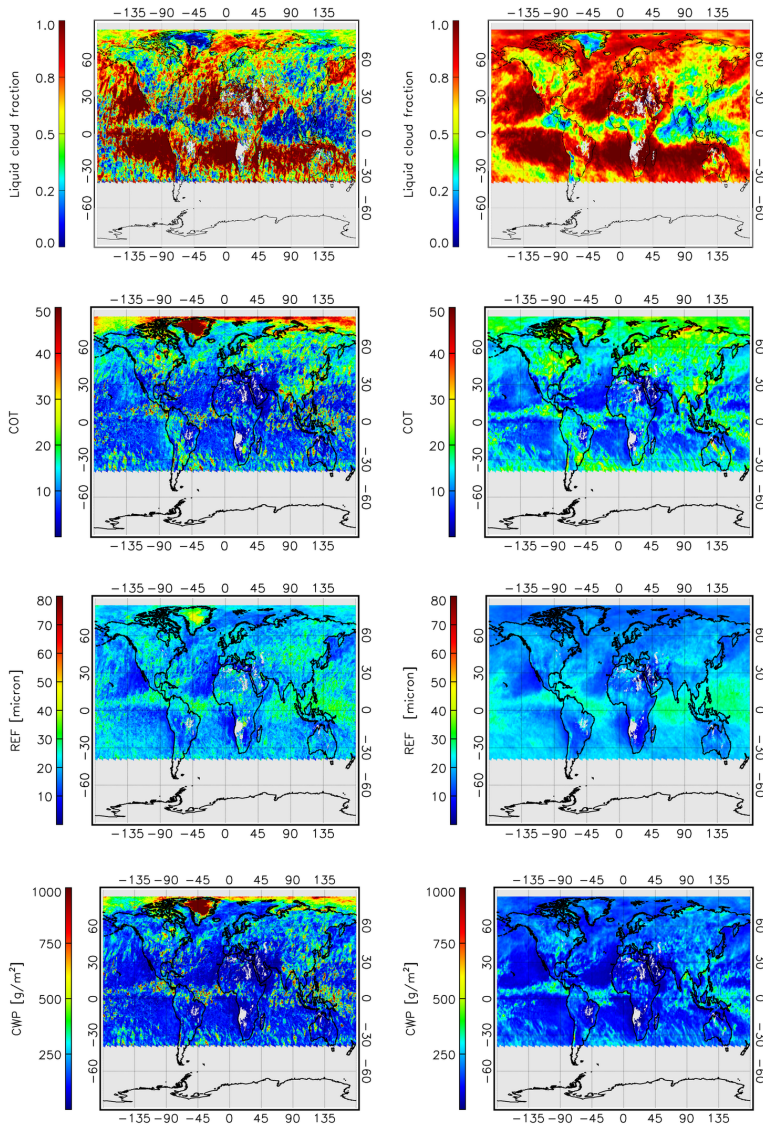
Figure 5.5: FAME-C (*left*) and MODIS-Terra (*right*) monthly mean for June 2008. *From top to bottom:* liquid cloud fraction, cloud optical thickness, effective radius [μm], cloud water path [g/m²].

Table 5.2: Bias and root mean square deviation (RMSD) for all grid cells as shown in Fig. 5.5 (all) and for latitudes below 60° (non-polar=np). LCF=liquid cloud fraction.

	Bias (all)	RMSD (all)	Bias (np)	RMSD (np)
LCF [0-1]	-0.15	0.26	-0.13	0.26
COT	-0.14	8.71	-1.28	7.33
REF [μm]	1.30	5.36	0.34	4.94
CWP [g/m^2]	54.65	199.1	21.71	137.0

was used. The equator crossing time difference between the Envisat and Terra (10.30 a.m.) satellites is about half an hour. The MODIS monthly mean values are computed from averaging daily product means on a global equal-angle grid with a spatial resolution of 1° x 1°. For the comparison, which was confined to the optical and micro-physical cloud properties, the FAME-C monthly mean cloud products are binned to the MODIS grid and only the daytime monthly means of the MODIS cloud properties are used. The MODIS effective radius based on measurements from the 1.6 μm channel are used.

Figure 5.5 and Table 5.2 present the results of the monthly mean comparison for set of optical and micro-physical cloud properties for the month June of the year 2008, for both FAME-C and MODIS observations. On a global scale, a general good agreement between the spatial patterns in the datasets is revealed. The variability within the FAME-C dataset is clearly higher than within the MODIS dataset. The FAME-C product for regions further away from the poles are much more impacted by individual orbits than the MODIS products due to lower sampling frequency. The MODIS swath width is about 4 times larger than the synergistic AATSR-MERIS swath width.

Regions with largest disagreements include the polar regions, particularly Greenland, with an overestimation of the cloud properties by FAME-C. This can be largely attributed to incorrectly identified clouds over snow/ice surfaces and the rather simple cloud phase detection method. Globally, the liquid cloud fraction is clearly lower for FAME-C than MODIS. Possible explanations are wrongly identified cirrus pixels as well as supercooled cloud droplets identified as ice clouds due to observed low brightness temperatures. An incorrectly identified cloud phase will also result in larger differences found between the cloud optical and micro-physical property retrievals. For example, incorrectly identified ice cloud pixels are expected to show lower retrieved effective radii than when assuming a water cloud in the forward model, see Fig. 4.3. This issue does however not explain the overestimation in the polar regions.

Comparison to MWR liquid water path

The FAME-C LWP monthly means are compared to the version 3 University of Wisconsin (UWisc) LWP dataset (O'Dell et al., 2008) for the years 2007 and 2008. The UWisc LWP climatology consists of monthly mean LWP as well as a mean monthly diurnal cycle on a 1°x1° spatial grid for the time period 1988-2008. It is based on retrievals applied to measurements from passive microwave radiometer instruments onboard several polar-orbiting and near-equatorial orbiting satellites: the Special Sensor Microwave/Imager (SSM/I), the Tropical Rainfall Measurement Mission (TRMM) Microwave Imager (TMI), and the Advanced Microwave Scanning Radiometer-EOS (AMSR-E). The retrievals are only performed over the oceans. The microwave channels fully penetrate clouds and provide a direct measurement of the total liquid cloud content, i.e., the cloud liquid water path. The retrieval is mostly insensitive to ice particles, however large ice particles might cause an underestimation of LWP. An estimate of rain water path in precipitating clouds is made and subtracted from the total liquid water path in order to retrieve the cloud liquid water path. The accuracy of the LWP climatology is estimated to be 15-30 % or higher, depending on the region.

The comparison is restricted to three regions mainly consisting of marine Stratocumulus clouds(liquid cloud phase): the area west of South Africa at 10°-20°S and 0°-10°E (SAO) the area west of California at 20°-30°N and 120°-130°W (NPA), the area west of South America at 16°-26°S and 76°-86°W (SPA). The areas are also indicated in Fig. 5.7. In order to enable a direct comparison of the LWP climatologies, the UWisc monthly mean LWP were corrected for the diurnal cycle in order to obtain the UWisc monthly mean LWP at the Envisat local overpass time at descending node, 10 a.m.. This was done with the information provided with the UWisc LWP climatology:

$$LWP(y,t) = \overline{LWP}(y) + a_1 cos\omega(t - T_1) + a_2 cos2\omega(t - T_2) \qquad (5.1)$$

where $\overline{LWP}(y)$ is the uncorrected monthly mean for each grid box of year y, ω is the radial frequency corresponding to a 24 hour time period, t is the local time, and a_1, a_2, T_1 and T_2 are the amplitudes and phases of first (24 hours) and second (12 hours) harmonic of the diurnal cycle, respectively. In addition, the UWisc LWP climatology represents all-sky values, thus the FAME-C values were multiplied with the monthly mean cloud fraction and the fraction of liquid water clouds, to convert the in-cloud LWP to all-sky LWP.

Table 5.3: Bias between FAME-C LWP and UWisc LWP for three marine Stratocumulus regions (described in the text).

Cloud fraction [%]	< 60	60-70	70-80	80-90	< 90
Occurrence [%]	18	24	19	25	14
LWP bias [g/m^2]	-9.6	-11.6	-5.8	-3.6	-1.2

Within FAME-C LWP is derived from the cloud optical thickness τ and effective radius r_{eff} assuming vertically homogeneous clouds:

$$LWP = \frac{2}{3}\tau \cdot r_{eff} \cdot \rho \qquad (5.2)$$

where ρ is the density of liquid water. The regions of interest in this study are characterized by marine Stratocumulus clouds with little cirrus contamination. These cloud types are known to be better represented by the adiabatic cloud model than the homogeneous cloud model for which the factor 2/3 becomes 5/9. Thus, the LWP of adiabatic clouds, LWP_{adi}, is related to the LWP of homogeneous clouds, LWP_{hom}, simply by a factor:

$$LWP_{adi} = \frac{5}{6} \cdot LWP_{hom} \qquad (5.3)$$

The results of the LWP comparison are presented in Fig. 5.6, as well as the FAME-C retrieved cloud fraction and liquid phase fraction. The FAME-C LWP error bars show the standard deviation within the region, while for UWisc LWP a fixed relative error of 20 % is taken. For all three regions the seasonal cycle is well captured, with the SAO region showing the most pronounced seasonal cycle in LWP and cloud fraction. For all regions, the liquid cloud fraction is very close to 1 for most of the time period. The underestimation of LWP, i.e., a negative bias, might be related to the fact that in clear-sky scenes non-zero MWR LWPs are retrieved. For AMSR-E retrieved LWP in marine Stratocumulus regions in clear-sky cases (as seen by MODIS) a positive biases of about 20 g/m^2 was found (Bennartz, 2007). Seethala and Horváth (2010) found a negative biases in the comparisons of MODIS LWP with AMSR-E LWP and biases increase with decreasing cloud fraction. Similar findings in this comparison are shown in Table 5.3.

The largest underestimation of LWP is observed for the SAO region during the months of August and September, in both years. This corresponds well with the biomass burning season in this area, which leads to absorbing aerosol layers either at or above the marine boundary layer clouds. Fig. 5.7

Figure 5.6: Comparison of liquid water path climatology for the years 2007-2008 for three marine Stratocumulus regions (described in the text).

shows monthly images of the Absorbing Aerosol Index (AAI) for the year 2008. The AAI indicates the presence of elevated absorbing aerosols in the atmosphere, such as desert dust and biomass burning aerosols from reflectances measured by GOME-2/MetOp-A (De Graaf et al., 2005). The maximum AAI is indeed found for the months August and September for both years (2007 not shown) in this region. The other two regions are hardly impacted by absorbing aerosol layers. In Haywood et al. (2004) it was found from theoretical calculations that satellite retrieved COT and REF from 1.6 μm channels, and hence the derived LWP, can be systematically low biased for elevated absorbing aerosol layers above marine boundary layer clouds. The underestimation of LWP derived from passive imagers with respect to LWP from MWR in the Stratocumulus region off the coast of southern Africa during the biomass burning was also observed in Bennartz (2007) and Seethala and Horváth (2010).

5.5 Summary and outlook: level-3 comparison

The level-3 comparisons to satellite reference datasets showed in general a good agreement for the optical and micro-physical cloud properties on a
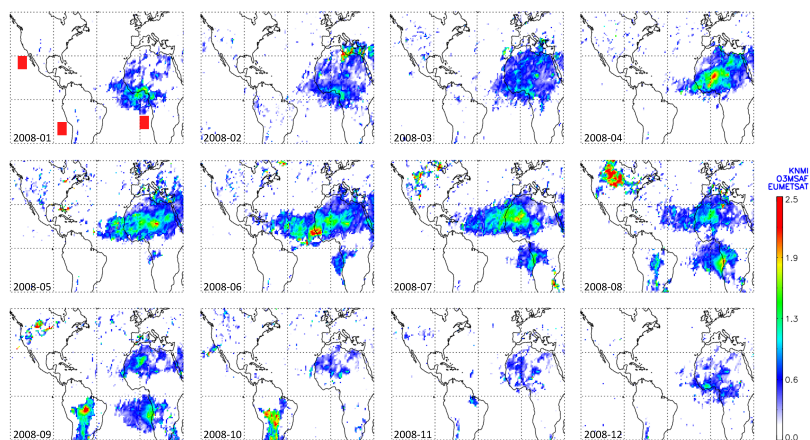
Figure 5.7: GOME-2/MetOp-A monthly means of the aerosol absorbing index (AAI) for the year 2008 (De Graaf et al., 2005). Adapted from http://www.temis.nl/airpollution/absaai. In the upper left panel are shown the three marine Stratocumulus regions in red.

global scale concerning spatial patterns. Due to lower sampling frequency of the synergistic AATSR-MERIS observations, the precision of the FAME-C level-3 dataset is reduced. Differences on a regional scale can become quite large, such as in the polar regions. The latter is mainly attributed to wrongly identified clouds over snow and ice surfaces in the FAME-C algorithm. One major uncertainty in the cloud properties is related to the simple cloud phase detection method. A large difference in liquid cloud fraction between FAME-C and MODIS was found, which has an impact on the results of the other cloud properties.

The marine Stratocumulus regions are often regarded as a good test bed for studies on cloud-aerosol interactions. In addition, their important role in the Earth-atmosphere energy balance contributes to the large number of climate-cloud studies focused on these regions. The impact of the absorbing aerosol index needs to be quantified for accurate interpretations of analysis. To a first order this can be done by using the AAI data to identify cloudy regions with and without overlying aerosol layers. The differences between the LWPs in non-affected regions and affected regions give an estimate of the bias, assuming that the elevated aerosol layer do not have a significant impact on the cloud dynamics of the affected region. The supposed influence of absorbing aerosol index on the cloud property retrievals should be kept in mind in approaches that use the satellite retrievals to as-
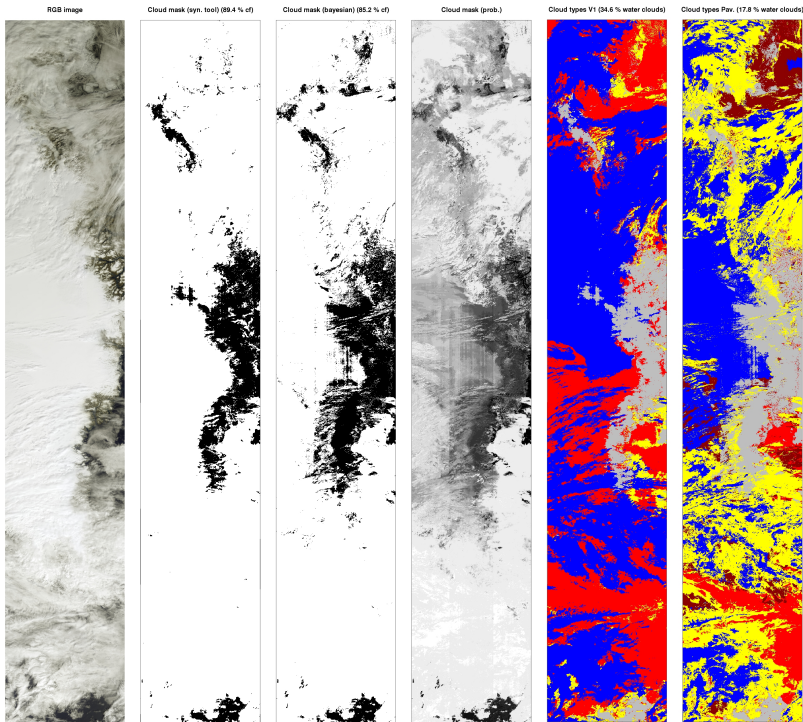
Figure 5.8: AATSR-MERIS orbit segment over Greenland on 17 August 2007. *From left to right:* 1) MERIS RGB, 2) old cloud mask synergistic (cloud fraction = 88.4 %), 3) new cloud mask (Bayesian, 4) cloud fraction = 84.1 % for a probability threshold of 50 %), 5) cloud probability from for new cloud masking method, 6) old cloud phase detection, 7) new cloud phase detection. For 2 and 3, white = cloud, black = cloud free. For 4, the whither the higher the probability. Cloud phase/types; For 5, red = water, blue = ice, yellow = cirrus, gray = no clouds. For 6, red = water, blue = opaque ice, yellow = cirrus and overlapping, gray = no clouds.

sess aerosol-cloud interactions, e.g., the first indirect effect. Low values of effective radius could be partly a result of the elevated absorbing aerosols and less due to the influence of aerosols on the cloud micro-physics directly.

One of the main limitation of cloud climatologies from polar-orbiting satellites is that they do not provide information on the daily cycle of the cloud properties. For this, the cloud climatologies can be combined with cloud climatologies from geostationary satellite. The disadvantage of the latter cloud climatologies is the limited coverage of the globe.

A couple of major adjustments concerning cloud detection and forward models, are being applied to the FAME-C algorithm, which are expected to have a significant impact on the level-2 retrievals and hence on the level-3 products as well. Figure 5.8 shows the old and new cloud mask as well as the old and new cloud phase detection for a scene over Greenland. From visual inspection it can be seen that the old and new cloud mask are very similar, with a slightly lower cloud fraction from the Bayesian cloud mask when taking a probability threshold of 50 %. From visual inspection, the amount of clouds over the elevated regions of Greenland appears to be overestimated. Considering that opaque ice clouds, cirrus clouds and overlapping clouds are grouped into the ice cloud category, the new cloud phase detection method identifies about 17 % more ice clouds for this scene. Through the use of separate water and ice cloud forward models, a change in cloud phase detection is expected to lead to changes in the retrieved cloud properties. The impact of the implementation of the new cloud mask and cloud phase detection method on the cloud property retrievals will be investigated on a level-2 basis for a set of specific scenes as well as for gridded and temporally averaged products.

The level-3 comparisons help to assess the overall retrieval performance as well as finding regions for which the retrievals are problematic. Then, the situations can be selected on a level-2 basis for in-depth retrieval assessments. Future level-3 evaluations will include comparisons of time series, i.e., for analysis of multi-annual and seasonal variability of cloud properties. In a similar manner, the FAME-C cloud climatologies for the cloud height products will be analyzed once processed on a global scale. Furthermore, the set of reference cloud climatologies will be extended, e.g., using a CALIOP global cloud climatology for the evaluation of the cloud detection method and cloud height retrievals. In addition, extensive analysis are needed to determine how the estimated (random and systematic) uncertainties and optimal estimation diagnostics on a level-2 basis can be meaningfully propagated to the level-3 products.

6

Exploiting the sensitivity of two satellite cloud height retrievals to cloud vertical distribution

Abstract This work presents a study on the sensitivity of two satellite cloud height retrievals to cloud vertical distribution. The difference in sensitivity is exploited by relating the difference in the retrieved cloud heights to cloud vertical extent. The two cloud height retrievals, performed within the Freie Universität Berlin AATSR MERIS Cloud (FAME-C) algorithm, are based on independent measurements and different retrieval techniques. First, cloud top temperature (CTT) is retrieved from Advanced Along Track Scanning Radiometer (AATSR) measurements in the thermal infrared. Second, cloud top pressure (CTP) is retrieved from Medium Resolution Imaging Spectrometer (MERIS) measurements in the oxygen-A absorption band. Both CTT and CTP are converted to cloud top height (CTH) using atmospheric profiles from a numerical weather prediction model. A sensitivity study using radiative transfer simulations in the near-infrared and thermal infrared were performed to demonstrate the larger impact of the assumed cloud vertical extinction profile on MERIS than on AATSR top-of-atmosphere measurements. The difference in retrieved CTH (ΔCTH) from AATSR and MERIS are related to cloud vertical extent (CVE) as observed by ground-based lidar and radar at three ARM sites. To increase the impact of the cloud vertical extinction profile on the MERIS-CTP retrievals, single-layer and geometrically thin clouds are assumed in the forward model. The results of the comparison to the ground-based observations were separated into single-layer and multi-layer cloud cases. Similar to previous findings, the MERIS-CTP retrievals

---

This chapter is based on Carbajal Henken et al. (2015)

appear to be close to pressure levels in the middle of the cloud. Assuming a linear relationship, the ΔCTH multiplied by 2.5 gives an estimate on the CVE for single-layer clouds. The relationship is weaker for multi-layer clouds. Due to large variations of cloud vertical extinction profiles occurring in nature, a quantitative estimate of the cloud vertical extent is accompanied with large uncertainties. Yet, estimates of the CVE can contribute to the characterization of a cloudy scene. To demonstrate the plausibility of the approach, an estimate of the CVE was applied to a case study. In light of the follow-up mission Sentinel-3 with AATSR and MERIS like instruments, Sea and Land Surface Temperature Radiometer (SLSTR) and (Ocean and Land Colour Instrument) OLCI, respectively, for which the FAME-C algorithm can be easily adapted, a more accurate estimate of the CVE can be expected. OLCI will have three channels in the oxygen-A absorption band, thus providing more pieces of information on the cloud vertical extinction profile.

6.1   Introduction

The vertical distribution of clouds plays an important role in both meteorological and climatological applications. It can be an indicator of the meteorological conditions, (thermo-)dynamical and micro-physical processes, in which a cloud forms (e.g. Yin and Zhai, 2013; Yuan et al., 2011; Luo et al., 2009). Further, the cloud vertical distribution affects radiative and latent heating fluxes, which in turn, affect the large-scale atmospheric circulation and precipitation processes (e.g. Wang and Rossow, 1998; Li et al., 2014).

Cloud-climate feedbacks are the main source of uncertainty in climate models (Flato et al., 2013). Accurate characterization of vertical distributions of different cloud types are needed to evaluate and improve the modeling of cloud-climate feedbacks and thus climate change projections. In Jiang et al. (2012) A-train observations are used to quantify the performances of models that participate in the Coupled Model Intercomparison Project (CMIP) in simulating clouds at different vertical levels. The results were submitted to the Intergovernmental Panel on Climate Change (IPCC) reports, and improvements in the simulation of ice water path, for example, were found in the comparison of Phase 5 CMIP model results compared to Phase 3 CMIP3 model results. Largest differences and spreads between the CMIP5 models and A-train observations of cloud water content profiles are found at upper tropospheric levels.

Cloud vertical distribution can be described by a set of cloud parameters, such as cloud top height and cloud base height, and subsequently cloud geometrical thickness, and the number of distinct cloud layers in an air column. These cloud parameters can be observed by a set of remote-sensing techniques using observations from ground-based or space-born instruments.

From ground-based observations information on cloud vertical distribution can be derived from, e.g., human observers, lidars, and radars. The first two only observe the cloud base height, while radar can observe the cloud vertical profile. However, the spatial coverage of these ground-based observations are mainly limited to land areas in the Northern hemisphere. Global and accurate observations of cloud vertical distribution are necessary for an improved understanding of cloud processes, and subsequently improved representations of these processes in climate models. Satellite observations can provide this global coverage. In 2005, the active instruments CPR (Cloud Profiling radar) and CALIOP (Cloud-Aerosol Lidar with Orthogonal Polarization) , on polar-orbiting satellites CloudSat (Stephens et al., 2002) and CALIPSO (Cloud-Aerosol Lidar and Infrared Pathfinder Satellite Observations) (Winker et al., 2003), respectively, as part of the A-train constellation, were launched. They provided first radar and lidar measurements on cloud and aerosol vertical profiles on a global scale. Since then both instruments have given the atmospheric research community many new insights on clouds and aerosols (e.g. Mace et al., 2007; Sassen et al., 2008) and their observations were extensively used in many evaluation studies (e.g. Naud et al., 2010; Weisz et al., 2007). However, they have a poor spatial coverage due to the nadir-only measurements.

Satellite observations from passive instruments have a larger spatial coverage. However, here the cloud properties are retrieved from information coming mainly from upper cloud layers, such as cloud top temperature, or they represent an integrated property, such as cloud water path. A number of satellite remote sensing techniques exist that retrieve cloud top heights (CTHs) from measurements of passive imagers. For example, cloud top height retrievals from thermal infrared (TIR) measurements have been performed using the CO_2 slicing technique (e.g. Menzel et al., 2008) or with brightness temperature (BT) measurements in window channels (Hamann et al., 2014) (TBD extent refs). Further, cloud top heights can be obtained from stereo, which is based on the parallax effect occurring between cloud observations from different viewing angles (e.g. Moroney et al., 2002). In (Wu et al., 2009) the vertical and latitudinal monthly mean of the vertically distributed volume cloud occurrence frequency were compared among various passive and active satellite instruments. Here, also a discussion on the strengths and weaknesses of the various passive CTH retrieval techniques is given. Also in Naud et al. (2005) inter-comparisons were performed for several passive and active cloud top height retrievals.

In 1961, Yamamoto and Wark (1961) proposed to retrieve cloud top altitude from space by measuring the absorption of reflected solar radiation in the oxygen-A absorption band located at around 760 nm. In the method the

strength of the absorption of radiation in the oxygen-A band is related to the cloud top pressure, via the mean photon path length. Later in the 1960s, first satellite retrievals using the oxygen-A absorption band showed that the enhancement of photon path length, due to multiple scattering inside the cloud, which in turn depends on cloud thickness and type, needs to be taken into account for accurate cloud top pressure retrievals (Saiedy et al., 1967). The impact of the cloud vertical inhomogeneity on the accuracy of the cloud top pressure retrievals has also been recognized in a number of theoretical studies (Fischer and Grassl, 1991a; Rozanov and Kokhanovsky, 2004; Preusker and Lindstrot, 2009). Various cloud height retrievals based on measurements in the oxygen-A absorption band are described in, e.g., Wang et al. (2008); Rozanov and Kokhanovsky (2004); Koelemeijer et al. (2002); Vanbauce et al. (1998). In most of these cloud height retrievals, multiple scattering inside the cloud layer is neglected or homogeneous cloud vertical profiles are assumed. This leads to the retrieval of a so called apparent cloud height which corresponds to a pressure level somewhere in the middle of the cloud rather than to the cloud top.

The Freie Universität Berlin AATSR MERIS Cloud (FAME-C) algorithm retrieves cloud top pressures (CTPs) from radiance measurements of the Medium Resolution Imaging Spectrometer (MERIS) in the oxygen-A band as well as cloud top temperatures (CTTs) from BT measurements in two TIR channels of the Advanced Along Track Scanning Radiometer (AATSR). Both instruments are mounted on the polar-orbiting Environmental satellite (Envisat). FAME-C is developed within the frame of the ESA Climate Change Initiative (Hollmann et al., 2013). Within FAME-C, mean cloud vertical extinction profiles derived from 1 year of data from CPR onboard CloudSat combined with MODIS data were used in order to account for a more realistic description of the multiple scattering inside the cloud. The extinction profiles where derived for nine cloud types taken from the ISCCP cloud classification (Rossow and Schiffer, 1999), which is based on total cloud optical thickness (COT) and cloud top pressure. For two case studies with vertically extended clouds it was shown that the choice of the cloud vertical extinction profile can have a large impact on the retrieved MERIS cloud top pressure. Comparisons to CPR cloud heights showed that on average the bias was reduced by a large amount when using the mean CPR profiles in stead of vertically homogeneous profiles (HOM) (Henken et al., 2013). This can be mainly attributed to lower extinction values in the upper cloud layers for the CPR profiles than for the HOM profiles, which appears to be closer to reality for these vertically extended clouds. However, for individual cloud scenes, the CTP retrieval can still have a large error if the profile assumption is wrong. The TIR cloud height retrievals are less affected by the profile

assumption.

In this study we aim to make use of the difference between the two different cloud height retrievals, since it obviously carries information on the cloud vertical distribution. The method of combining a cloud height retrieval from measurements in the oxygen-A absorption band with an independent cloud height retrieval to retrieve information on the cloud vertical distribution was suggested by others before (e.g. Vanbauce et al., 2003; Kokhanovsky and Rozanov, 2005; Lindstrot et al., 2010b). In order to maximize the impact of the desired parameter, which is the cloud vertical extent (CVE), on the signal, which is here the difference between the cloud height retrievals, we limit the correction for in-cloud scattering in the MERIS-CTP retrieval. For this purpose, the FAME-C algorithm was extended to also retrieve the cloud height assuming a single-layer cloud with a geometrical thickness of 20 hPa, which can be considered to be close to a solid reflector for optically thick clouds. Ground-based observations from lidar and radar at three Atmospheric Radiation Measurement (ARM) program's site are used to relate the retrieved cloud height differences to observed cloud vertical extent.

The structure of this paper is as follows. First, a sensitivity study is presented for which radiative transfer simulations in the near-infrared and thermal infrared part of the spectrum for clouds with different cloud vertical extinction profiles are performed and compared. Second, the ground-based and satellite observations are presented. Next, the method for the comparison of the ground-based data and satellite data is described. Then, the results are presented and discussed. In addition, the application of the method is shown in a case study. Last, conclusions are given.

6.2 Sensitivity study

For cloud particles, the single scattering albedo is close to one in the visible (VIS) and near-infrared (NIR) part of the spectrum and therefore little absorption of photons by cloud particles takes place. In the thermal infrared (TIR) part of the spectrum the single scattering albedo has values clearly less than one, so most photons will be absorbed by cloud particles after just a few scattering events. Thus in the satellite-based TIR CTH retrievals the signal mostly stems from the upper part of the clouds, while the VIS/NIR CTH retrievals are affected by a larger part of the cloudy atmosphere. Therefore, the assumed cloud vertical extinction profiles in the retrievals are expected to have a larger impact on the VIS/NIR CTH retrieval than on the TIR CTH retrievals.
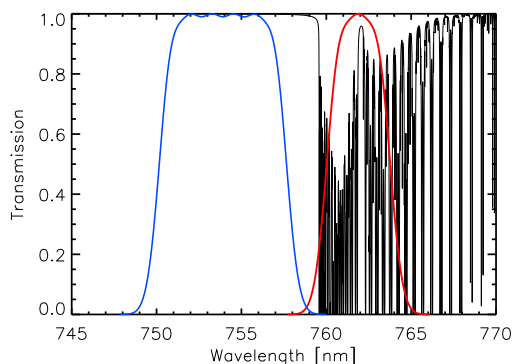
Figure 6.1: Spectral response functions for MERIS window channel 10 (blue) and MERIS channel 11 in the oxygen-A absorption band (red). Black lines: oxygen absorption lines.

To investigate the difference in impact of cloud vertical extinction profile on cloud top height retrieved with radiances from NIR spectral bands and BTs from a window TIR spectral band, radiative transfer simulations have been performed using the model Matrix Operator Model (MOMO). MOMO has been developed at the Freie Universität Berlin (Fell and Fischer, 2001; Hollstein and Fischer, 2012). Recently, MOMO was extended trough the implementation of thermal emission of radiation by the surface and (cloudy) atmospheric layers, allowing for accurate simulations in the thermal infrared (Doppler et al., 2014a). The spectral response function of the AATSR 10.8 μm channel was used for the simulations in the TIR. The spectral response functions of the MERIS window channel 10 centered at 753 nm and the oxygen-A absorption channel 11 centered at 761 nm, were used to simulate the ratio of the absorption channel over the window channel, shown in Fig. 6.1.

Radiative transfer simulations in a cloudy atmosphere are performed assuming a plane-parallel atmosphere with a vertical resolution of 20 hPa in the troposphere. A US Standard Atmosphere was assumed in the simulations (McClatchey et al., 1972). Furthermore, the surface is modeled as a Lambertian reflector with a surface albedo of 0.02 and a surface pressure of 1013 hPa. A Rayleigh optical thickness of 0.026 is taken. To compute the absorption coefficients of the atmospheric gases, the k-distribution method is used (Bennartz and Fischer, 2000; Doppler et al., 2014b), where the in-
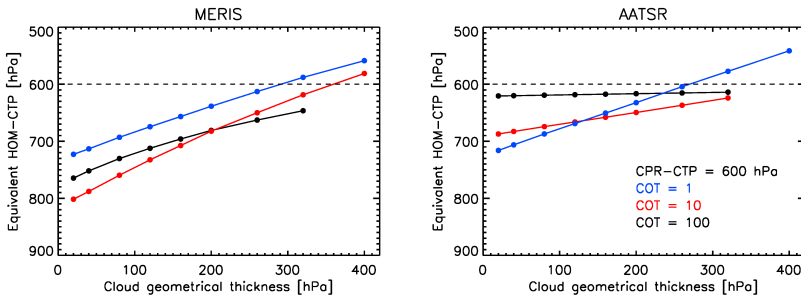
Figure 6.2: The equivalent HOM-CTP for varying CGT and COT, assuming a CPR cloud with CTP = 600 hPa. Settings in the radiative transfer simulations: satellite viewing angle = 0°, solar viewing angle = 35°, relative azimuth angle = 0°, surface albedo = 0.02 and MERIS central wavelength = 762 nm.

formation on the position and width of absorption lines is taken from the HITRAN database (Rothman et al., 2009).

Two types of cloud vertical extinction profiles are assumed in the simulations. For the first type, 1 year of data from the combined CPR and MODIS product (2B-TAU, Polonsky et al. (2008)) was analyzed. The clouds observed by CPR and MODIS were sorted with respect to their CTP and COT, resulting in 9 different cloud types, using the ISCCP cloud type classification (Rossow and Schiffer, 1999). For each cloud type, the average vertical profile of extinction and the average vertical extent were determined (Henken et al., 2013). The derived normalized extinction profiles (from here on called CPR profiles/clouds) were then used in the MOMO radiative transfer simulations to generate LUTs for each of the nine cloud types. The LUTs serve as forward models in the cloud height retrievals. For the second type, vertically homogeneous extinction profiles are assumed (from here on called HOM profiles/clouds) . As an additional LUT dimension, each cloud is modeled with varying vertical extents, starting with a cloud geometrical thickness (CGT) of 20 hPa and ending at the maximum possible geometrical thickness.

For cloud layers below 440 hPa water droplets are assumed with a fixed effective radius of 10 μm, The single-scattering properties were computed using a Mie code (Wiscombe, 1980). For cloud layers above 440 hPa ice crystals are assumed with a fixed effective radius of 40 μm, assuming single-scattering properties described in Baum et al. (2005).

For a number of selected CTP and COT combinations, the simulated results (MERIS radiance ratio and AATSR BT) at the top of the atmosphere (TOA)
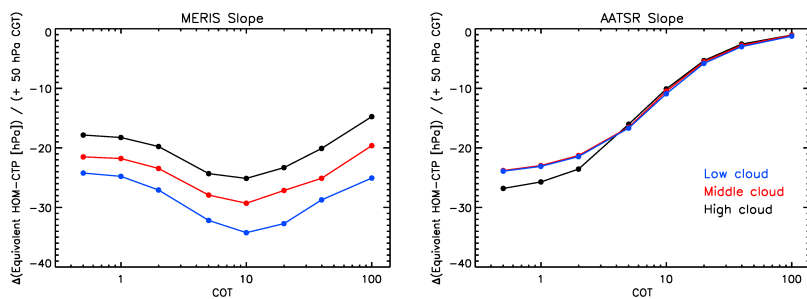
Figure 6.3: The sensitivity of the equivalent AATSR HOM-CTP to an increase of CGT by 50 hPa. Cloud top pressure of low cloud = 800 hPa, middle cloud = 600 hPa, and high cloud = 300 hPa.

using CPR profiles were compared to the simulated results using HOM profiles with varying CGT. Figure 6.2 shows the combinations of CTP and CGT of HOM clouds resulting in the smallest deviation in the simulated signal from the case of a CPR cloud with CTP of 600 hPa, for both AATSR and MERIS. In general, the difference between the equivalent HOM-CTP and CPR-CTP is smaller for AATSR than MERIS, especially for optically thick clouds. The largest difference between the equivalent HOM-CTP and the CPR-CTP is found for geometrically thin clouds with COT= 10 for MERIS, while for AATSR the largest difference is found for optically thin clouds. The higher CTPs of the HOM clouds can be explained by the fact that for clouds with the CPR profiles, the extinction of the upper cloud layers is lower than the extinction of the upper cloud layers for clouds with a HOM profile. In order to get the same TOA signal as the CPR-cloud, the HOM-cloud needs to be placed at a lower altitude. Alternatively, the CGT of the HOM-cloud can be increased. For both MERIS and AATSR, the HOM-CTP approaches the CPR-CTP for increasing CGT, and even underestimates the CTP for clouds extending down to the surface. Note that for the very optically thick clouds (COT=100), the HOM-CTP does not reach the CPR-CTP, even for vertically extended clouds. Missing points relate to CPR simulations results that did not fall within the range of HOM-CTP results for the assumed CGT. For optically thick clouds, the dependence of the HOM-CTP on the CGT is much weaker for AATSR than for MERIS, due to the fact that in the TIR the contribution from lower cloud layers to the TOA signal is weaker, and thus the shape of the entire cloud vertical extinction profile plays a less important role in the TIR than in the NIR.

The sensitivity of the equivalent HOM-CTP to the CGT, i.e., the change in

96
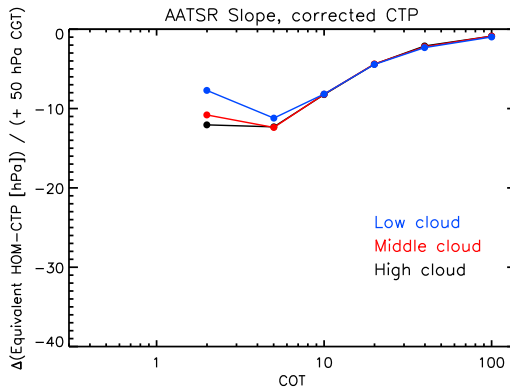
Figure 6.4: The sensitivity of the equivalent MERIS and AATSR HOM-CTP to an increase of CGT by 50 hPa. The pressure at 1 COT into the cloud is taken as corrected CTP. Cloud top pressure of low cloud = 800 hPa, middle cloud = 600 hPa, and high cloud = 300 hPa.

the equivalent HOM-CTP for an increase of the CGT with 50 hPa, is summarized in Fig. 6.3 for various cloud types. The sensitivity was computed by simply applying a linear fit to each line that corresponds to a fixed COT and varying CGT (as can be seen in Fig. 6.2). This was done for a low (800 hpa), mid-level (600 hPa), and high (300 hPa) cloud and a range of COTs. For MERIS, the sensitivity is largest for clouds with COT = 10. This can be explained as follows. For optically thin clouds, a large part of the radiation arriving at TOA has traversed the cloud without interaction with cloud particles, thus not affected by the vertical extinction profile of the cloud at all. For optically very thick clouds, the contribution from upper cloud layers will dominate the TOA signal even for geometrically thicker clouds, thus the influence of the entire vertical extinction profile is smaller. For optically moderate thick clouds, the full vertical extinction profile has an impact on the TOA signal, while the contribution of the earth surface and the lower atmosphere is suppressed. For AATSR, the sensitivity decreases for increasing COT, indicating that the assumed shape of the extinction profile is of less importance for optically thick clouds due to contributions to the TOA signal arising mainly from upper cloud layers. In summary, the MERIS sensitivity is always higher than the AATSR sensitivity for COT $>$ 5.

Figure 6.4 shows the AATSR sensitivity of the equivalent HOM-CTP to the CGT for which the physical CTPs are substituted by radiometric CTPs. For each cloud type, the CTP is taken at the pressure level for which COT=1.

This is the radiometric cloud top, when assuming no scattering and a linear dependency of the Planck function on the COT. Again linear fits were applied. Now, the sensitivity is largest for clouds with COTs around 5. For optically thinner clouds, the CPR and HOM radiometric cloud heights are located more closely to each other than the physical cloud heights. Note, considering scattering and contribution to the TOA signal from lower cloud layers, the actual radiometric cloud top will be located at more than one COT into the cloud (Sherwood et al., 2004).

This exercise confirms that one can expect cloud height retrievals from MERIS to be more affected by the cloud vertical extinction profiles than the AATSR cloud height retrievals, at least for optically thick clouds.

6.3 Data

AATSR and MERIS

Within FAME-C two independent cloud top height products are retrieved on a pixel-basis: AATSR cloud top temperature and MERIS cloud top pressure. AATSR and MERIS are two passive imagers mounted on the polar-orbiting satellite Envisat, launched in March 2002 and operational until April 2012. Envisat flies in a sun-synchronous orbit with an equator crossing time of 10.00 LT, descending node.

In the MERIS-CTP retrieval the transmission within the oxygen-A band is estimated from the ratio of channel 11 and window channel 10. In the AATSR cloud top temperature retrieval, brightness temperature measurements at 10.8 μm and 12 μm are used to retrieve cloud top temperature. Atmospheric profiles from a numerical weather prediction model (NWP) reanalysis are used to convert cloud top temperature and cloud top pressure to cloud top height. The cloud top temperature is compared to the temperature profile and the minimum height at which the cloud top temperature equals the atmospheric temperature is assumed to be the cloud top height. For optically thick clouds, CTT will be similar to the measured 10.8 μm brightness temperature, corrected for the atmosphere. For optically thin clouds, the cloud emissivity is taken into account, which will result in a CTT that is lower than the measured 10.8 μm brightness temperature. More information on the two independent cloud top height retrievals can be found in Carbajal Henken et al. (2014).

For this study, the FAME-C algorithm was extended to also provide retrieved cloud top temperature from AATSR, cloud top pressure from MERIS, and accompanying cloud top heights, assuming a single-layer and vertically homo-

geneous cloud with a geometrical thickness of 20 hPa. For optically thick clouds, this comes close to a solid reflector. Further adjustments in the FAME-C algorithm include the use of a new cloud masking method (Hollstein et al., 2014), which is in first order aimed to reproduce the former cloud masking method but with higher computational efficiency. Before applying the cloud mask, the AATSR and MERIS measurements are collocated using the BEAM toolbox (Fomferra and Brockmann, 2005; ESA, 2014a). In addition, the 3rd reprocessing for AATSR data were used and an empirical nonlinear correction was applied to the 12 μm channel (Smith, 2014). Further, a straylight correction was performed for the MERIS measurements (Lindstrot et al., 2010a). Last, a pixel-based multi-layer cloud detection, i.e., thin cirrus over low-level water clouds, based on Pavolonis and Heidinger (2004) is implemented. Note, no distinct retrievals for multi-layer cloud cases are performed, the pixels are simply flagged as multi-layer cloud or not.

ARM milimeter cloud radar and micropulse lidar

The active remote sensing of clouds (ARSCL) product from ground-based observations performed at the Atmospheric Radiation Measurement (ARM) program's site in the Southern Great Plains (SGP), three sites in the Tropical Western Pacific (TWP), and North Slope Alaska (NSA) is used. It provides cloud boundary heights, i.e., cloud base height and cloud top height, for up to 10 cloud layers (Clothiaux et al., 2000). The cloud boundary heights are determined from a combination of measurements from the Micropulse Lidar (MPL) and Millimeter Cloud Radar (MMCR) and are provided at a vertical resolution of 45 m and a temporal resolution of 10 s.

With the radar, vertically extended and multiple cloud layers can be penetrated and observed, while the laser beam of the lidar is attenuated quite fast and thus can not penetrate much further beyond the lowest cloud base in case of optically thick clouds. The radar is less sensitive to small cloud particles and optically thin clouds, often occurring at great heights. These clouds can be observed well with the lidar system. Furthermore, radar observations of cloud base heights are often hampered in the presence of large non-hydrometeor particles, such as insects. They might be observed as low-level clouds. For large concentrations of non-hydrometeors, also the lidar observations of cloud base become problematic. In case of heavy precipitation both radar and lidar observations are not useful (Clothiaux et al., 2000).

6.4 Method

To study the relationship between the difference in the two FAME-C cloud height retrievals and the cloud vertical extent as observed by ground-based lidar and radar instruments, the satellite and ground-based observations of clouds need to be matched accordingly.

For each ARM site the satellite orbit segments of all Envisat overpasses with available FAME-C level-2 cloud properties for the years 2003-2011 are collected. The ground-based observations and satellite observations occur on different spatial scales, thus temporal averaging for the ARSCL products and spatial averaging for the FAME-C products is performed. From the ARSCL data, the height of the top height of the highest cloud layer and the base height of the lowest cloud layer are collected for a 5-minute time period centered at the time of overflight of Envisat. The CVE is derived from the difference between the two extreme cloud boundaries. In addition, also the number of cloud layers and the distance between the cloud layers is extracted from the ARSCL data. From the FAME-C data, a 9 by 9 pixel box centered at the center pixel was taken to compute mean vertical cloud top heights. The pixel with the minimum distance to the location of the radar was selected as the center pixel. Using the ARSCL cloud top height and the satellite instrument viewing geometry, parallax correction is applied to adjust the center pixel. This was performed separately for AATRS-CTT and MERIS-CTP.

In the evaluation, only cases with enough successfully retrieved cloud height products within the satellite pixel box ($>$ 80 %) and within the 5-minute time period ($>$80 %) are selected. More precisely, only pixels for which the FAME-C cloud top heights that converged successfully with a cost $<$ 20 are considered. For the ARSCL products at least 80 % of the time steps need to have a cloud base height determined by the lidar and a cloud top height either determined by radar or lidar. In addition, the temporal and spatial variability should not be too large, i.e., the standard deviation of the selected cloud top heights should be $<$1 km. The selection criteria were chosen in such a way that the study is directed towards mainly overcast cloudy scenes with spatially and temporally uniform cloud top heights, but still a large enough number of cases remain available. It results in a total of 153 selected cases, which is less than 6 % of all Envisat overflights for which the AATSR swath passes over one of the ARM sites within the years 2003-2011. Note, both the ARSCL products, depending on the ARM site, and FAME-C products do not cover the full time period of the years 2003-2011. There were 82, 24 and 47 valid cases found for the SGP, TWP and NSA ARM sites, respectively.
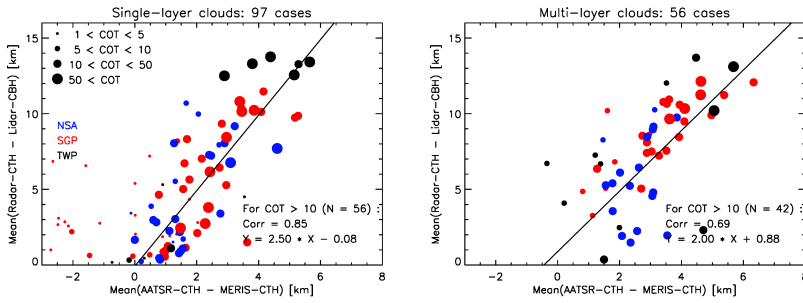
Figure 6.5: Results of the comparison of mean cloud vertical extent derived from radar and lidar observations to the difference in mean cloud top height retrieved with AATSR and MERIS.

6.5   Results and discussion

Figure 6.5 shows the results presented separately for single-layer and multi-layer clouds. Single-layer cloud cases are defined as cases where at least 80 % of the pixels in the satellite pixel box have not been identified as multi-layer clouds according to the multi-layer test implemented in FAME-C. Multi-layer cloud cases are defined as cases where at least 80% of the pixels in the pixel box have been identified as multi-layer clouds.

One can immediately see that on average the difference in AATSR and MERIS CTHs (ΔCTH) increases with increasing CVE as observed by the radar and lidar. This is true for both single-layer and multi-layer clouds, though the correlation is higher for single-layer clouds. Most obvious outliers mainly represent cases where the mean COT < 10. As one would expect from the climatic regimes, the most vertically extended clouds are found at the TWP sites, followed by the SGP site. The dependence of the ΔCTH on the CVE is strongest for the SGP site for optically thick clouds. There are several cases with optically thin clouds for which the MERIS-CTH is higher than the AATSR-CTH. One of the possible reasons for this is that the AATSR-CTT might be incorrect due to wrong assumptions in the forward model, which are related to estimates of the cloud emissivity and ignoring multiple scattering. For single-layer low-level clouds, the derivation of the AATSR-CTH might be ambiguous or missed if the temperature profile does not represent a temperature inversion accurately enough. This leads to a positive ΔCTH for clouds with observed small vertical extents.

A linear fit was computed for the cases with COT > 10, also shown as the black solid line in the figures. Variability around the fitted lines present an

Table 6.1: Resulting biases and root mean square deviation (RMSD) from the comparison between the FAME-C cloud top heights and radar/lidar derived cloud top heights. Presented separately for single-layer clouds (Single) and multi-layer clouds (Multi) as well as for FAME-C cloud top heights retrieved using 1 homogeneous cloud layer (HOM) and the CPR vertical cloud profiles (CPR). Results are also shown for clouds with a mean cloud optical thickness larger than 5.

		Bias [km]		RMSD [km]	
		Single	Multi	Single	Multi
AATSR-CTH	CPR	-0.88	-1.58	2.38	2.89
	HOM	-1.20	-1.58	2.63	2.89
MERIS-CTH	CPR	-0.27	-1.76	2.51	4.03
	HOM	-2.44	-4.50	3.57	5.44
AATSR-CTH, COT > 5	CPR	-0.56	-1.55	1.99	2.86
	HOM	-0.62	-1.56	1.98	2.86
MERIS-CTH, COT > 5	CPR	-0.22	-1.71	2.57	3.99
	HOM	-2.71	-4.42	3.81	5.38

indication of the variability of cloud vertical profiles/distributions that occur in nature. However, the variability will also have contributions from errors in the retrievals as well as incorrect matching of the observations (not observing the same cloud volume). For single-layer clouds a factor of 2.5 is found between ΔCTH and CVE. Knowing that on average the retrieved AATSR cloud top temperature is close to, but just below the cloud top, the difference between the AATSR-CTH and MERIS-CTH is about half of the vertical extent of the cloud. This corresponds well to the findings of Ferlay et al. (2010) were it was found that the POLDER (Polarization and Directionality of the Earth's Reflectances) cloud oxygen pressure is on average close to the pressure level at the geometrical middle of the cloud. The multi-layer cloud cases show a weaker dependence of the ΔCTH on the CVE, which can be explained by considering that for these cloud cases also a large part of the vertical column consists of cloud-free atmosphere. Here, the mean photon path length in the NIR is not increased due to in-cloud scattering. Thus, the effect of the cloud vertical distribution is suppressed relative to vertically extended single-layer clouds.

To demonstrate the difference in retrieved cloud top height products assuming CPR cloud vertical profiles and HOM cloud vertical profiles they were compared to the radar-based CTHs. The results are listed in Table 6.1. AATSR-CTH shows a negative bias. As expected, the difference in biases between CPR and HOM, and also between single-layer and multi-layer clouds are small, since AATSR tends to see the upper cloud layers and there-
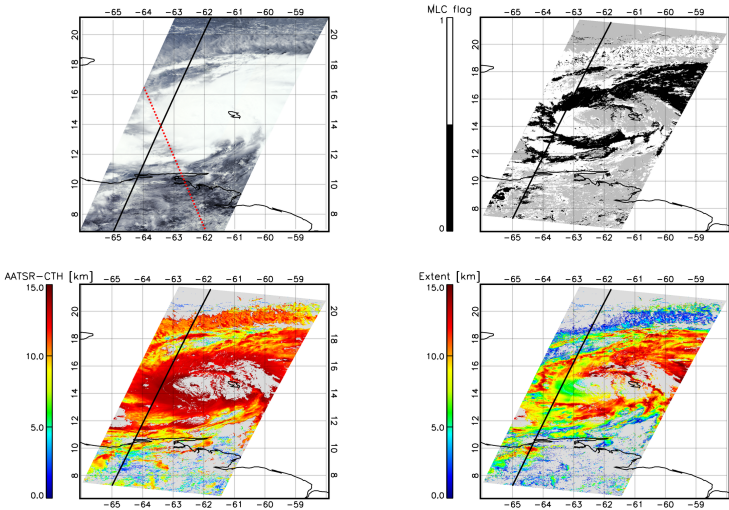
Figure 6.6: View on hurricane Dean on 17 August 2007. *Top left:* color composite from MERIS bands 2, 3 and 4. *Top right:* FAME-C multi-layer cloud flag. *Bottom left:* retrieved AATSR cloud top height. *Bottom right:* estimated cloud vertical extent. The solid black line and the dotted red line show the AATSR-MERIS and CloudSat cross-section, respectively, as presented in Fig. 6.7. Note, the CloudSat overpass occurred about 3 hours later than the AATSR-MERIS observations presented here.

fore is less dependent on the cloud vertical extinction profile and vertical extent. For MERIS-CTH, the difference in biases between CPR and HOM is large, with a small negative bias for CPR and a large negative bias for HOM. When only including cases where the mean COT > 5, the absolute biases decreases slightly for all except MERIS-CTH HOM. For AATSR-CTH the root mean square deviation (RMSD) of HOM and CPR show similar values and are smallest for single-layer clouds with COT > 5. The RMSD of MERIS-CTH HOM is larger than for MERIS-CTH CPR, and overall largest for multi-layer clouds.

6.6 Case study

The estimate of CVE from the relationship found in the former section has been applied to Envisat observations of Hurricane *Dean*, which moved across the Caribbean Sea in August 2007. Hurricanes are dynamical cloud
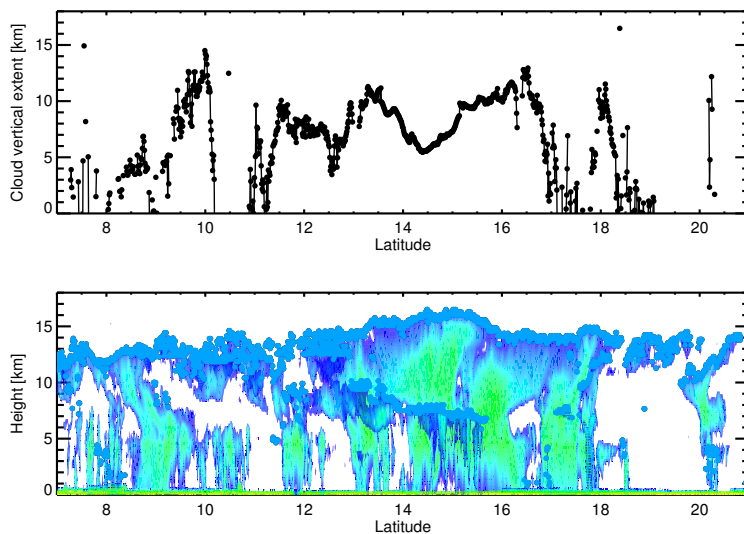
Figure 6.7: Cross-section of hurricane Dean (17 August 2007). *Top:* estimated cloud vertical extent from FAME-C cloud heights. *Bottom:* radar reflectivity from CPR on CloudSat. The blue dots show the height of the most upper layer identified as cloud by the CPR cloud mask (> 30). Note, cross sections from the Envisat and CloudSat overpasses did not collocate in space and time.

systems which consist of parts with dense and vertically extended clouds in the main part of the system, multi-layer clouds, optically thick and thin cirrus clouds, and single-layer low-level clouds at the outer regions of the system.

Figure 6.6 shows the true color image of the hurricane, as well as the multi-layer flag, cloud top height retrieved from AATSR and the estimate of the vertical extent of the system. In the inner area no successful retrievals were performed within FAME-C partly due to no convergence and partly due to saturation occurring in the AATSR IR channels. This is also the area where the hurricane eye is located. The estimated CVE along the black line can be qualitatively compared to observations from CPR. The cross-section as well as the CPR radar reflectivities are shown in Fig. 6.6. The Envisat cross-sections slightly 'touches' the main part of the system. Note that the Cloud-Sat overpass is about three hours later than Envisat. The cloud system will have moved mostly towards the west as well as rotated. Therefore, no pixel-

based comparison is possible. The overpass of CloudSat is shown in the upper left panel of Fig. 6.6 with the dotted red line. Further, CPR observations of low-level water clouds near the surface can be problematic due to ground clutter.

The vertical extent is estimated to be up to 15 km for the main part of the hurricane, which agrees well with the maximum height as observed by CPR. The maximum estimated vertical extent near the main part of the system (between latitude 14° and 16°) appears to be underestimated when comparing to CPR observations. At around latitude 14° and longitude 63° there is an area for which the estimated extent is smaller (about 6 km), while for this area still a height of up to 15 km is retrieved. This might be the dense part of the cirrus shield where the hurricane does not extend down to the surface anymore. The area south of the main part of the hurricane appears to be dominated by low-level clouds with some thin cirrus aloft. Here, the estimated CVE is mostly small (< 5 km). Directly north of the main part of the hurricane, where the spiral outflow of thin cirrus is located, the CVE is also low (< 3 km). In general, the estimated vertical extent is within several kilometers of the cloud top height for the main part of the system as well as for optically thick clouds (the very bright areas in the true color image). Further, the variability in the estimated CVE is much larger than the variability in the retrieved cloud top height. This is in agreement with the fact that the main part of a hurricane consists of vertically extended clouds (from the tropopause to the surface), while areas directly surrounding this main part consist of a very dense cirrus shield with bands of clouds below. There is an indication that in case of thin cirrus above low-level clouds, occurring in the outer regions of the system, the estimated CVE is well below the distance between the two cloud layers.

6.7 Summary and outlook

This study presents the evaluation of differences between two cloud height retrievals that are based on independent techniques, and relating the differences to cloud vertical extend as observed by ground-based active instruments. The cloud vertical extent is an additional parameter to the cloud top height, both parameters describing the cloud vertical distribution. As suggested by others before, the combined use of the cloud pressure retrieval in the oxygen-A absorption band with an independent cloud height retrieval, here the cloud top temperature from thermal infrared measurements, could potentially be used to characterize the vertical distribution of observed clouds. Measurements from the passive imagers AATSR and MERIS onboard the polar-orbiting satellite Envisat were used in the FAME-

C algorithm. Cloud top temperature is retrieved using brightness temperature measurements from two AATSR thermal infrared channels, while cloud top pressure is retrieved with the use of the ratio of the MERIS channel in the oxygen-A absorption band and a near-by window channel.

Due to larger mean in-cloud photon penetration depths for shortwave radiation than for longwave radiation, the sensitivity of the latter retrieval (in the NIR) to the cloud vertical extinction profile is larger than for the former retrieval (in the TIR). This was shown in a sensitivity study were simulations results from the radiative transfer model MOMO for homogeneous and inhomogeneous cloud vertical extinction profiles are compared, for both simulations using MERIS and AATSR spectral response functions. The inhomogeneous profiles are derived from combined CPR and MODIS data. The equivalent cloud top pressure of the homogeneous clouds with predefined cloud geometrical thickness was derived by comparing the simulated TOA signals of both cloud types. The results confirm that in general, the MERIS equivalent HOM-CTP is more sensitive to a change in the CGT than AATSR. For both AATSR and MERIS simulations, this sensitivity decreases for increasing COT.

The differences between the MERIS-CTP and AATSR-CTT, both converted to CTH using atmospheric profiles from a numerical weather prediction model, were compared to the cloud vertical extent. In the MERIS-CTP retrieval a single-layer, vertically homogeneous and geometrically thin cloud was assumed to suppress the correction for multi-scattering in the cloud. This was done to increase the impact of the cloud vertical extent on the CTH difference. The extent is defined as the distance between the top height of the highest cloud layer and the base height of the lowest cloud layer. These cloud boundaries are extracted from the ARSCL cloud product based on ground-based radar and lidar observations. A comparison strategy was developed whereby spatial averaging is applied to the satellite products and temporal averaging to the ARSCL products. Only cases with a high cloud cover and limited spatial and temporal variability in the cloud height products are selected. Comparisons were performed at three ARM sites covering different climate regimes, surface conditions and sun-satellite viewing geometry. Results were separated into single-layer and multi-layer cloud cases. It was shown that the difference in CTHs increases with increasing cloud vertical extent for both single-layer and multi-layer clouds, though the relation appears stronger for single-layer clouds. Applying a linear fit to the results with COT > 10 indicates that a rough estimate of the cloud vertical extent can be obtained by multiplying the CTH difference by a factor of 2.5. If we assume that AATSR-CTH is close to but a bit lower than the physical cloud top (this was indicated by a small negative bias compared to radar

CTH), than the MERIS-CTH is close to the geometrical center of the cloud. Similar findings were found in other studies related to cloud pressure retrievals using measurements in the oxygen-A absorption band. The large variability in cloud vertical extinction profiles occurring in nature and the use of only one measurement in the oxygen-A absorption band limits the accuracy of cloud vertical extent estimates. However, by using a simple linear relationship a rough estimate of the cloud vertical extent can be made, contribution to the characterization of a cloudy scene. An estimate of cloud vertical extent is automatically an estimate of the cloud base height of the lower cloud layer. As a demonstration of the plausibility of the approach, estimates of the cloud vertical extent for a cloudy scene were performed within a case study.

A limited number of cases was exploited mainly due to filtering out observations of inhomogeneous cloud fields in space and time. Comparisons to observations of cloud vertical extent from CPR on CloudSat and CALIOP on CALIPSO can be performed next. However, matching overpasses of Envisat and A-train only occurred at high latitudes for which CTH retrievals are complicated due to snow/ice surfaces and large solar zenith angles. Moreover, the different satellite viewing geometries in the presence of inhomogeneous cloud fields complicate the matching of Envisat and A-train observations.

The impact of future improvements/updates in the FAME-C algorithm on the cloud height retrievals will be investigated. Such changes will include an updated version of RTTOV (and coefficient files) as well as an improved cloud phase detection and a new cloud masking method.

Follow-up mission Sentinel-3, planned to be launched in 2015, will carry the AATSR and MERIS like instruments, Sea and Land Surface Temperature Radiometer (SLSTR) and the Ocean and Land Colour Instrument (OLCI), respectively. Thus making FAME-C applicable to those measurements as well. Three channels in the oxygen-A absorption band are planned for OLCI. Several channels can help to separate signals coming from different parts of the cloudy atmosphere or from the surface, potentially allowing for retrieving more information on the cloud vertical distribution compared to one channel.

CHAPTER **7**
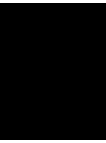
Conclusions and outlook

In this work a set of cloud properties is retrieved from satellite observations on a global scale and for a multi-annual time series. The synergy of two multi-spectral imaging radiometers AATSR and MERIS, onboard the polar-orbiting satellite Envisat, was exploited to retrieve the following macro-physical, optical and micro-physical properties:

- cloud cover

- cloud thermodynamic phase

- cloud optical thickness

- cloud effective radius

- cloud water path

- cloud top temperature

- cloud top pressure

- cloud top height

The synergistic approach allows for an improved characterization of clouds with regards to a single-sensor approach by combining spectral information from AATSR and MERIS instruments. For this purpose, the AATSR and MERIS

measurements are collocated and a cloud detection method is applied that uses measurements from both instruments (Gómez-Chova et al., 2010).

Both AATSR and MERIS were primarily designed for observations of sea surface temperature and ocean color, respectively. However, together they provide measurements ranging from the visible, near-infrared to the thermal infrared part of the spectrum. A set of measurements in the visible and near-infrared allows for retrievals of cloud optical thickness and effective radius based on an earlier method (Nakajima and King, 1990). From these retrievals, the cloud liquid and ice water path are derived. The forward models were made separately for water and ice clouds. The cloud phase determination is based on a simple brightness temperature threshold technique combined with a cirrus detection method. Cloud top temperatures are retrieved from AATSR thermal infrared measurements. Of particular interest in this work is the cloud top pressures retrieval using MERIS measurements in the oxygen-A absorption band. It provides an additional independent source of information on cloud height next to the cloud top temperature. From both, the cloud top height is derived using atmospheric profiles from a numerical weather prediction model.

As an additional cloud property, the cloud vertical extent is estimated from the two independently retrieved cloud heights. The method exploits the fact that the MERIS-CTP retrieval is more sensitive to the cloud vertical extinction profile than the AATSR-CTT retrievals. This was demonstrated with radiative transfer simulations as well as relating the difference in the retrieved cloud heights to vertical cloud extent as observed with ground-based radar and lidar instruments. To increase the impact of the cloud vertical extinction profile on the MERIS-CTP retrieval, the FAME-C algorithm was extended with a forward model that assumes geometrically thin clouds, which are close to a solid reflector for optically thick clouds. Knowing that the derived AATSR-CTH is relatively close to, but below the physical cloud top for most cloud cases, the retrieved MERIS-CTP is close to pressure levels corresponding to the geometrical middle of the cloud. This is in agreement with previous studies on cloud top pressure retrievals from measurements in the oxygen-A absorption band. The estimates on the cloud vertical extent have large uncertainties due to the combination of the variability of the cloud vertical extinction profiles occurring in nature and the limitation of only one MERIS measurement in the oxygen-A absorption band. The potential to contribute to the characterization of a cloudy scene was demonstrated in a case study.

The retrievals are performed within the framework of the optimal estimation method, which allows for propagation of uncertainties in the measure-

ments, forward model and forward model parameters as well as the inclusion of a-priori knowledge and its uncertainty. In addition to the uncertainty on the retrievals, the method provides another diagnostic that can serve as a quality control on the retrievals. The value of the cost function at the solution provides a measure of consistency between the state parameters and the measurements. In the evaluation exercise, FAME-C cloud property retrievals with very high costs were not considered, since these likely indicate scenes that are not well represented by the forward model. A rough estimate of a cost threshold was determined based on visual inspection of several scenes, balancing the effect of loosing too many retrievals when setting the cost threshold too low and considering too many problematic retrievals when setting the cost threshold too high. In the interest of evaluating the newly developed FAME-C algorithm, most retrievals were included in the validation exercises. For an improved quality control on the retrievals, the uncertainty estimates need to be improved and extended. For example, correlations between uncertainties should be quantified. Furthermore, random and systematic errors should be distinguished in the analyses and possibly corrected for. Also, more analysis need to be made on how to propagate the uncertainties meaningfully into higher level products.

To obtain confidence in the performance of the retrievals as well as to assess deficiencies in the retrievals for particular cloudy scenes, comparisons to well established and documented satellite cloud property retrievals were performed. The MODIS-Terra cloud optical and micro-physical cloud products were chosen as a reference dataset since the retrievals and their performances are well-documented and based on similar measurements. The latter reduces the impact of very different instrument characteristics on the differences in the retrievals. The evaluation was done by focusing on specific regions of interest, with each their own characteristics of cloud type occurrences. Best agreements were found for a marine Stratocumulus region. Ground-based radar and lidar observations are used to evaluate the two cloud top height products. As was anticipated by earlier performed sensitivity studies, the AATSR-CTH is more accurate than MERIS-CTH for high clouds, while MERIS-CTH is more accurate for low-level clouds. This emphasizes the advantage of having two cloud height retrievals based on different techniques. Both CTH retrievals are more accurate for single-layer clouds than for multi-layer clouds.

Several quality control flags are produced that help to identify difficult cloudy scenes, such as thin cirrus clouds, multi-layer clouds, the presence of sun-glint and snow and ice surfaces. The flags contribute to the identification of problematic retrievals. From comparisons to MODIS level-2

cloud properties it was found that wrongly identified cloudy pixels as cirrus clouds by the cirrus detection method, which for most turned out to be partially filled cloud pixels at cloud boarders, resulted in some large inconsistencies between both datasets. A few major adjustments are currently made in the FAME-C algorithm, including a newly developed cloud mask and implementation of more advanced cloud typing algorithm. The impact of these changes on the retrievals will be assessed accordingly. Further, the accuracy of the FAME-C retrievals also depends on the accuracy of the auxiliary input data. This will be assessed for specific cases, such as the impact of the surface albedo uncertainty on the uncertainty of retrievals of thin clouds over bright surfaces. Also, improvements on a technical basis in the algorithms as well as the incorporation of more accurate auxiliary data are analyzed, which are expected to affect the retrievals, e.g., the way interpolation is performed in the look-up tables and the inclusion of near-real time ice and snow extent data, respectively. The impact of sub-pixel cloudiness on the retrievals can be investigated by using the full-resolution MERIS data. The use of the forward view of AATSR is considered, which can potentially add information on the cloud micro-physical properties. However, the challenge is to accurately combine the nadir and forward view in cloudy scenes.

The ultimate objectives of developing satellite based cloud property retrievals and reprocessing the retrievals on a global scale and for a multi-annual time series, is to increase our understanding on the role of clouds in climate, to monitor climate change and to improve climate projections by improved parameterizations of cloud processes in the climate models. This is done by observing spatial and temporal variations of cloud properties on a global scale and for long time series. For the purpose of consistency with climate model outputs, as well as with large-scale cloud property datasets from other instruments, the orbit-wise and pixel-based retrievals are gridded spatially to equal-angle grids and daily composites as well as monthly means are computed to create level-3 products, i.e., cloud climatologies. The FAME-C monthly mean was compared to the MODIS-Terra monthly mean. The spatial patterns are very similar, though large differences were found in the polar regions. The FAME-C cloud climatologies are much noisier, which is related to the relatively small swath width of AATSR, resulting in a much lower sampling frequency compared to MODIS-Terra. The accuracy of the liquid water path climatology when compared to a climatology based on microwave radiometer measurements falls well within the estimated uncertainty. Largest differences can likely be explained by the presence of elevated absorbing aerosol layers, which affect the cloud optical and micro-physical retrievals from which the liquid water path is de-

rived.

The inter-comparison and validation exercises will be extended to the global scale to cover a large range of climatic regions, surface conditions and sun-satellite viewing geometries, and for the entire time period, to evaluate seasonal and multi-annual variability. Further extensions comprise of increasing the pool of reference datasets from well-established satellite retrievals, such as AVHRR-GAC, CALIOP and CPR based cloud products, and MSG-SEVIRI CPP products as well as from ground-based observations. Within the frame of the ESA Cloud CCI project, comparisons to AATSR retrievals with the use of the CC4CL algorithm are planned. This is of particular interest since differences in the retrievals can then be attributed to the retrieval method only, basically the assumptions made in the retrievals, and not to different instrument characteristics. At the same time, in-depth studies on difficult cloudy scenes as well as cloudy scenes of special interest will be conducted. From both the energy-budget and aerosol-cloud interaction perspective, the vast regions dominated by marine Stratocumulus clouds at the west sides of the continents are of particular interest.

The FAME-C cloud retrievals and cloud climatologies will be extended to the 10 year time period of Envisat observations. This dataset can then serve as a basis for studying inter-annual variability of cloud properties on a global scale. Since Envisat was a polar-orbiting satellite, the daily cycle of cloud properties can not be inferred from the retrievals. Very long (multi-decadal) and consistent time series are needed to be able to observe small, but potentially significant trends in the cloud properties accurately. Unfortunately, contact with Envisat was lost in April 2012 resulting in a time gap between Envisat and its follow-up mission Sentinel-3, planned to be launched in 2015. A proposed method to bridge the gap is based on using measurements from MODIS-Terra. Though several channels have similar characteristics, difficulties can arise due to, e.g., different channel settings and sun-satellite geometry, which will suppress consistency between the datasets. Importantly, MODIS does not have a channel in the oxygen-A absorption band. Fortunately, a series of Sentinel-3 satellites is planned, which will allow for a multi-annual time series of measurements.

The FAME-C algorithm can be easily adapted as well as extended and applied to SLSTR and OLCI measurements for retrievals of cloud properties. Both instruments will be onboard the polar-orbiting satellite Sentinel-3. Several things are considered to improve the retrievals for these instruments. First, more spectral channels are available. SLSTR will have a channel at 2.2 μm, which can be used for retrieval of effective radius. At these wavelengths, cloud particles are more absorbing reducing the uncertainty

of the retrievals due to less impact of 3D effects. In the 3.7 μm channel this is even more true. However, then the contribution of thermal emission in these measurements needs to be taken into account. Further, OLCI will have three channels in the oxygen-A absorption band, which is exptected to increases the independent pieces of information to describe a given cloud scene. The TOA signals at different wavelengths in the oxygen-A band will stem from different parts of the clouds. This could be used for an improved characterization of the cloud vertical profile. In addition, the swath width of SLSTR is about three times larger than the swath width of AATSR. This will increase the sampling frequency and hence the precision in the level-3 cloud products.

Satellite retrievals of cloud properties have become essential in climate studies. A series of space-born platforms for the remote sensing of the Earth-atmosphere system are planned to be launched in the near future, each with their own strengths and weaknesses with regards to cloud observations. As the collection of cloud observations on a global scale and the improvements of cloud property retrievals continue in time, so will their significance in climate studies.

Bibliography

Arakawa, A. Modelling clouds and cloud processes for use in climate models. *The Physical Basis of Climate and Climate Modelling. GARP Publications Series, WMO*, 16:183–197, 1975. (p. 5).

Arking, A. Latitudinal distribution of cloud cover from TIROS iii photographs. *Science*, 143 (3606):569–572, 1964. (p. 7).

Baum, B. A.; Yang, P.; Heymsfield, A. J.; Platnick, S.; King, M. D.; Hu, Y. X., and Bedka, S. T. Bulk scattering properties for the remote sensing of ice clouds. part ii: Narrowband models. *J. Appl. Meteorol.*, 44(12):1896–1911, 2005. (pp. 19, 20, 24, 38, 54, 95, 139).

Bender, F. A. M.; Ramanathan, V., and Tselioudis, G. Changes in extratropical storm track cloudiness 1983–2008: observational support for a poleward shift. *Clim. Dynam.*, 38(9-10):2037–2053, 2012. (p. 4).

Bennartz, R. Global assessment of marine boundary layer cloud droplet number concentration from satellite. *J. Geophys. Res.: Atmospheres (1984–2012)*, 112(D2), 2007. (pp. 84, 85).

Bennartz, R. and Fischer, J. A modified k-distribution approach applied to narrow band water vapour and oxygen absorption estimates in the near infrared. *J. Quant. Spectrosc. Radiat. Transf.*, 66(6):539–553, 2000. (pp. 24, 57, 94).

Bezy, J. L.; Delwart, S., and Rast, M. MERIS-A new generation of ocean-colour sensor onboard Envisat. *ESA bulletin*, 103:48–56, 2000. (p. 21).

Boucher, O.; Randall, D.; Artaxo, P.; Bretherton, C.; Feingold, G.; Forster, P.; Kerminen, V.; Kondo, Y.; Liao, H.; Lohmann, U., et al. Clouds and aerosols climate change 2013: The physical science basis. contribution of working group i to the fifth assessment report of the Intergovernmental Panel on Climate Change ed t. f. stocker, d. qin, g. k. plattner, m. tignor, s. k. allen, j. boschung, a. nauels, y. xia, v. bex and p. m. midgley. *Cambridge University Press, Cambridge, United Kingdom and New York, NY, USA*, 2013. (p. 4).

Bourg, L.; D'Alba, L., and Colagrande, P. Meris smile effect characterisation and correction. *ESA Technical Note*, 2008. (p. 51).

Buriez, J. C.; Vanbauce, C.; Parol, F.; Goloub, P.; Herman, M.; Bonnel, B.; Fouquart, Y.; Couvert, P., and Seze, G. Cloud detection and derivation of cloud properties from POLDER. *Int. J. Rem. Sens.*, 18(13):2785–2813, 1997. (p. 33).

Carbajal Henken, C. K.; Lindstrot, R.; Preusker, R., and Fischer, J. FAME-C: cloud property retrieval using synergistic AATSR and MERIS observations. *Atmos. Meas. Tech.*, 7(11): 3873–3890, 2014. doi:10.1117/12.465995. (pp. 47, 69, 98).

Carbajal Henken, C. K.; Doppler, L.; Lindstrot, R.; Preusker, R., and Fischer, J. Exploiting the sensitivity of two satellite cloud height retrievals to cloud vertical distribution. *Atmos. Meas. Tech. Discuss.*, 8(3):2623–2655, 2015. (p. 89).

Cess, R. D.; Zhang, M. H.; Potter, G. L.; Alekseev, V.; Barker, H. W.; Bony, S.; Colman, R. A.; Dazlich, D. A.; Del Genio, A. D.; Deque, M., et al. Comparison of the seasonal change in cloud-radiative forcing from atmospheric general circulation models and satellite observations. *J. Geophys. Res.: Atmospheres (1984–2012)*, 102(D14):16593–16603, 1997. (p. 6).

Chen, Y.; Sun-Mack, S.; Minnis, P.; Smith, W. L., and Yooung, D. F. Surface spectral emissivity derived from MODIS data. In *Optical Remote Sensing of the Atmosphere and Clouds III*, volume 361 of *Proc. SPIE 4891*, 2003. doi:10.1117/12.465995. (p. 59).

Chen, Y.; Sun-Mack, S.; Arduini, R. F., and Minnis, P. Clear-sky and surface narrowband albedo variations derived from VIRS and MODIS Data. In *CONFERENCE ON CLOUD PHYSICS -CD ROM EDITION-; 5.6 Atmospheric radiation 12th:; Conference, Atmospheric radiation*, volume 12, Boston, Mass., USA, 2006. Atmospheric radiation. (p. 59).

Clapp, P. F. Global cloud cover for seasons using TIROS nephanalyses. *Mon. Wea. Rev*, 92(495): 22, 1964. (p. 7).

Clement, A. C.; Burgman, R., and Norris, J. R. Observational and model evidence for positive low-level cloud feedback. *Science*, 325(5939):460–464, 2009. (p. 4).

Clothiaux, E. E.; Ackerman, T. P.; Mace, G. G.; Moran, K. P.; Marchand, R. T.; Miller, M. A., and Martner, B. E. Objective determination of cloud heights and radar reflectivities using a combination of active remote sensors at the ARM CART sites. *J. Appl. Meteorol.*, 39(5): 645–665, 2000. (pp. 76, 99, 99).

Clough, S. A.; Iacono, M. J., and Moncet, J. Line-by-line calculations of atmospheric fluxes and cooling rates: Application to water vapor. *J. Geophys. Res.: Atmospheres (1984–2012)*, 97 (D14):15761–15785, 1992. (p. 25).

Clough, S. A.; Shephard, M. W.; Mlawer, E. J.; Delamere, J. S.; Iacono, M. J.; Cady-Pereira, K.; Boukabara, S., and Brown, P. D. Atmospheric radiative transfer modeling: a summary of the AER codes. *J. Quant. Spectrosc. Radiat. Transf.*, 91(2):233–244, 2005. (p. 25).

De Graaf, M.; Stammes, P.; Torres, O., and Koelemeijer, R. B. A. Absorbing Aerosol Index: sensitivity analysis, application to GOME and comparison with TOMS. *J. Geophys. Res.: Atmospheres (1984–2012)*, 110(D1), 2005. (pp. 85, 86, 142).

De Haan, J. F.; Bosma, P. B., and Hovenier, J. W. The adding method for multiple scattering calculations of polarized light. *Astronomy and Astrophysics*, 183:371–391, 1987. (p. 23).

Delwart, S.; Preusker, R.; Bourg, L.; Santer, R.; Ramon, D., and Fischer, J. MERIS in-flight spectral calibration. *Int. J. Rem. Sens.*, 28(3-4):479–496, 2007. (p. 38).

Deschamps, P. Y.; Bréon, F. M.; Leroy, .; Podaire, A.; Bricaud, A.; Buriez, J. C., and Seze, G. The POLDER mission: Instrument characteristics and scientific objectives. *IEEE Trans. Geosci. Remote Sens.*, 32(3):598–615, 1994. (p. 8).

Dessler, A. E. A determination of the cloud feedback from climate variations over the past decade. *Science*, 330(6010):1523–1527, 2010. (p. 4).

Diedenhoven, B. van; Cairns, B.; Geogdzhayev, I. V.; Fridlind, A. M.; Ackerman, A. S.; Yang, P., and Baum, B. A. Remote sensing of ice crystal asymmetry parameter using multi-directional polarization measurements–part 1: Methodology and evaluation with simulated measurements. *Atmos. Meas. Tech. Discuss.*, 5(3):4321–4359, 2012. (p. 20).

Doppler, L.; Carbajal Henken, C.; Pelon, J.; Ravetta, F., and Fischer, J. Extension of radiative transfer code MOMO, matrix-operator model to the thermal infrared–Clear air validation by comparison to RTTOV and application to CALIPSO-IIR. *J. Quant. Spectrosc. Radiat. Transf.*, 144:49–67, 2014a. (pp. 23, 23, 24, 25, 26, 94).

Doppler, L.; Preusker, R.; Bennartz, R., and Fischer, J. k-bin and k-IR: k-distribution methods without correlation approximation for non-fixed instrument response function and extension to the thermal infrared—Applications to satellite remote sensing. *J. Quant. Spectrosc. Radiat. Transf.*, 133:382–395, 2014b. (pp. 25, 57, 94).

Eitzen, Z. A.; Xu, K., and Wong, T. Cloud and radiative characteristics of tropical deep convective systems in extended cloud objects from CERES observations. *J. Climate*, 22(22):5983–6000, 2009. (p. 4).

ESA. MERIS quality working group: MERIS 3rd data reprocessing, software and adf updates, tech. rep. a879.nt.008.acri-st, acri. Technical report, ESA, 2011. available at http://earth.eo.esa.int/pcs/envisat/meris/documentation. (p. 51).

ESA. BEAM earth observation toolbox and development platform. http://www.brockmann-consult.de/cms/web/beam, 2014a. last access: May 2014. (pp. 51, 99).

ESA. AATSR handbook, section "pre-flight characteristics and expected performance", 2014b. available at https://earth.esa.int/handbooks/aatsr/CNTR3-2-1.htm. (p. 65).

ESA. ESA bulletin 105 -february 2001; AATSR: Global-change and surface-temperature measurements from envisat, 2014c. available at http://www.esa.int/esapub/bulletin/bullet105/bul105_1.pdf. (p. 50).

ESA. SENTINEL-3, 2014d. http://www.esa.int/Our_Activities/ObservingtheEarth/Copernicus/Sentinel-3. (p. 50).

Fell, F. and Fischer, J. Numerical simulation of the light field in the atmosphere–ocean system using the matrix-operator method. *J. Quant. Spectrosc. Radiat. Transf.*, 69(3):351–388, 2001. (pp. 22, 52, 94).

Ferlay, N.; Thieuleux, F.; Cornet, C.; Davis, A. B.; Dubuisson, P.; Ducos, F.; Parol, F.; Riédi, J., and Vanbauce, C. Toward new inferences about cloud structures from multidirectional measurements in the oxygen A band: Middle-of-cloud pressure and cloud geometrical thickness from POLDER-3/PARASOL. *J. Appl. Meteor. Climatol.*, 49(12):2492–2507, 2010. (p. 102).

Fischer, J. and Grassl, H. Radiative transfer in an atmosphere—ocean system: an azimuthally dependent matrix-operator approach. *Appl. Opt.*, 23(7):1032–1039, 1984. (p. 22).

Fischer, J. and Grassl, H. Detection of cloud-top height from backscattered radiances within the oxygen a band. part 1: Theoretical study. *J. Appl. Meteorol.*, 30(9):1245–1259, 1991a. (p. 92).

Fischer, J. and Grassl, H. Detection of cloud-top height from backscattered radiances within the oxygen A band. Part 1: Theoretical study. *J. Appl. Meteorol.*, 30(9):1245–1259, 1991b. (p. 34).

Fischer, J.; Cordes, W.; Schmitz-Peiffer, A.; Renger, W., and Mörl, P. Detection of cloud-top height from backscattered radiances within the oxygen a band. part 2: Measurements. *J. Appl. Meteorol.*, 30(9):1260–1267, 1991. (p. 32).

Fischer, J.; Preusker, R., and Schüller, L. ATBD 2.3 Cloud Top Pressure. Algorithm Theoretical Basis Document PO-TN-MEL-GS-0006. Algorithm theoretical basis document, European Space Agency, 2010. (p. 79).

Flato, G.; Marotzke, J.; Abiodun, B.; Braconnot, P.; Chou, S. C.; Collins, W.; Cox, P.; Driouech, F.; Emori, S.; Eyring, V., et al. Evaluation of climate models. In *Climate Change 2013: The Physical Science Basis. Contribution of Working Group I to the Fifth Assessment Report of the Intergovernmental Panel on Climate Change*, pages 741–866. Cambridge University Press, 2013. (p. 90).

Fomferra, N. and Brockmann, C. BEAM - The ENVISAT MERIS and AATSR toolbox. In *MERIS (A) ATSR Workshop 2005*, volume 597, page 13, 2005. (pp. 51, 99).

Gómez-Chova, L.; Camps-Valls, G.; Munoz-Marı, J.; Calpe, J., and Moreno, J. Cloud screening methodology for MERIS/AATSR synergy products. In *Proc.'2nd MERIS/AATSR User Workshop', ESRIN, Frascati*, pages 22–26, 2008. (p. 51).

Gómez-Chova, L.; Camps-Valls, G.; Calpe, J.; Munoz, J., and Moreno, J. Cloud screening ATBD. Algorithm theoretical basis document, University of Valencia, 2010. (pp. 10, 51, 110).

Govaerts, Y. RTMOM V0B. 11 user's manual. *Rep. EUM/MET/DOC/06*, 503, 2008. (p. 23).

Grainger, R. G. *An Atmospheric Radiative Transfer Primer*. 2015. in preparation. (pp. 28, 29).

Hall, D. K.; Salomonson, V. V., and A., Riggs G. Modis/aqua snow cover monthly l3 global 0.05deg cmg. version 5.[2007-2009], 2006. Online resource: http://nsidc.org/data/myd10cm.html. (p. 59).

Ham, S.; Sohn, B.; Kato, S., and Satoh, M. Vertical structure of ice cloud layers from Cloud-Sat and CALIPSO measurements and comparison to NICAM simulations. *J. Geophys. Res.: Atmospheres*, 118(17):9930–9947, 2013. (p. 35).

Hamann, U.; Walther, A.; Baum, B.; Bennartz, R.; Bugliaro, L.; Derrien, M.; Francis, P.; Heidinger, A.; Joro, S.; Kniffka, A., et al. Remote sensing of cloud top pressure/height from SEVIRI: analysis of ten current retrieval algorithms. *Atmos. Meas. Tech. Disc.*, 7(1):401–473, 2014. (pp. 49, 91).

Hanel, R. A. Determination of cloud altitude from a satellite. *J. Geophys. Res.*, 66(4): 1300–1300, 1961. (p. 32).

Hansen, J. E. and Hovenier, J. W. The doubling method applied to multiple scattering of polarized light. *J. Quant. Spectrosc. Radiat. Transf.*, 11(6):809–812, 1971. (p. 23).

Hansen, J. E. and Hovenier, J. W. Interpretation of the polarization of venus. *J. Atmos. Sci*, 31 (4):1137–1160, 1974. (pp. 19, 37, 54).

Hansen, J. E. and Travis, L. D. Light scattering in planetary atmospheres. *Space Science Reviews*, 16(4):527–610, 1974. (pp. 20, 37, 54).

Harrison, E. F.; Minnis, P.; Barkstrom, B. R.; Ramanathan, V.; Cess, R. D., and Gibson, G. G. Seasonal variation of cloud radiative forcing derived from the Earth Radiation Budget Experiment. *J. Geophys. Res.: Atmospheres (1984–2012)*, 95(D11):18687–18703, 1990. (p. 2).

Harrop, B. E. and Hartmann, D. L. Investigating tropical cloud radiative forcing in a cloud-resolving model. In *AGU Fall Meeting Abstracts*, volume 1, page 0057, 2012. (p. 4).

Haywood, J. M.; Osborne, S. R., and Abel, S. J. The effect of overlying absorbing aerosol layers on remote sensing retrievals of cloud effective radius and cloud optical depth. *Quarterly Journal of the Royal Meteorological Society*, 130(598):779–800, 2004. (p. 85).

Henken, C.; Lindstrot, R.; Filipitsch, F.; Walther, A.; Preusker, R., and Fischer, J. Fame-c: Retrieval of cloud top pressure with vertically inhomogeneous cloud profiles. In *AIP Conference Proceedings*, volume 1531, page 412, 2013. (pp. 31, 58, 92, 95).

Heymsfield, A. J.; Bansemer, A.; Field, P. R.; Durden, S. L.; Stith, J. L.; Dye, J. E.; Hall, W., and Grainger, C. A. Observations and parameterizations of particle size distributions in deep tropical cirrus and stratiform precipitating clouds: Results from in situ observations in TRMM field campaigns. *J. Atmos. Sci.*, 59(24):3457–3491, 2002. (pp. 17, 139).

Heymsfield, A. J.; Matrosov, S., and Baum, B. A. Ice water path-optical depth relationships for cirrus and deep stratiform ice cloud layers. *J. Appl. Meteorol.*, 42(10):1369–1390, 2003. (p. 55).

Hollmann, R.; Merchant, C. J.; Saunders, R.; Downy, C.; Buchwitz, M.; Cazenave, A.; Chuvieco, E.; Defourny, P.; De Leeuw, G.; Forsberg, R., et al. The ESA climate change initiative: Satellite data records for essential climate variables. *Bull. Amer. Meteor. Soc.*, 94(10):1541–1552, 2013. (pp. 10, 49, 92).

Hollstein, A. and Fischer, J. Radiative transfer solutions for coupled atmosphere ocean systems using the matrix operator technique. *J. Quant. Spectrosc. Radiat. Transf.*, 113(7):536–548, 2012. (pp. 23, 52, 94).

Hollstein, A.; Fischer, J.; Carbajal Henken, C., and Preusker, R. Bayesian cloud detection for MERIS, AATSR, and their combination. *Atmos. Meas. Tech. Discuss.*, 7(5):11045–11085, 2014. (p. 99).

IPCC. Ipcc, 2013: Summary for policymakers. in: Climate change 2013: The physical science basis. Technical report, 2013. (p. 48).

ISCCP. International satellite cloud climatology project, 2014. http://isccp.giss.nasa.gov. (p. 48).

Jiang, J. H.; Su, H.; Zhai, C.; Perun, V. S.; Del Genio, A.; Nazarenko, L. S.; Donner, L. J.; Horowitz, L.; Seman, C.; Cole, J., et al. Evaluation of cloud and water vapor simulations in CMIP5 climate models using NASA A-Train⍰ satellite observations. *J. Geophys. Res.: Atmospheres (1984–2012)*, 117(D14), 2012. (p. 90).

Justice, C. O.; Vermote, E.; Townshend, J. R. G.; Defries, R.; Roy, D. P.; Hall, D. K.; Salomonson, V. V.; Privette, J. L.; Riggs, G.; Strahler, A., et al. The Moderate Resolution Imaging Spectroradiometer (MODIS): Land remote sensing for global change research. *IEEE Trans. Geosci. Remote Sens.*, 36(4):1228–1249, 1998. (p. 8).

Koelemeijer, R. B. A.; Stammes, P.; Hovenier, J. W., and De Haan, J. F. Global distributions of effective cloud fraction and cloud top pressure derived from oxygen A band spectra measured by the Global Ozone Monitoring Experiment: comparison to ISCCP data. *J. Geophys. Res.: Atmospheres (1984–2012)*, 107(D12):AAC–5, 2002. (p. 92).

Kokhanovsky, A. A. and Rozanov, V. V. Cloud bottom altitude determination from a satellite. *IEEE Geoscience and Remote Sensing Letters*, 2(3):280, 2005. (p. 93).

Li, Y.; Thompson, D. W. J.; Stephens, G. L., and Bony, S. A global survey of the instantaneous linkages between cloud vertical structure and large-scale climate. *J. Geophys. Res.: Atmospheres*, 119(7):3770–3792, 2014. (p. 90).

Lindstrot, R.; Preusker, R.; Ruhtz, T.; Heese, B.; Wiegner, M.; Lindemann, C., and Fischer, J. Validation of MERIS cloud-top pressure using airborne lidar measurements. *J. Appl. Meteor. Climatol.*, 45(12):1612–1621, 2006. (p. 32).

Lindstrot, R.; Preusker, R., and Fischer, J. Empirical correction of stray light within the meris oxygen a-band channel. *J. Atmos. Oceanic Technol.*, 27(7):1185–1194, 2010a. (pp. 51, 99).

Lindstrot, R.; Preusker, R., and Fischer, J. Remote sensing of multilayer cloud-top pressure using combined measurements of MERIS and AATSR on board Envisat. *J. Appl. Meteor. Climatol.*, 49(6):1191–1204, 2010b. (pp. 45, 93).

Lindstrot, R.; Preusker, R.; Diedrich, H.; Doppler, L.; Bennartz, R., and Fischer, J. 1D-Var retrieval of daytime total columnar water vapour from MERIS measurements. *Atmos. Meas. Tech.*, 5(3):631–646, 2012. (p. 25).

Llewellyn-Jones, D.; Edwards, M. C.; Mutlow, C. T.; Birks, A. R.; Barton, I. J., and Tait, H. AATSR: Global-change and surface-temperature measurements from Envisat. *ESA bulletin*, 105: 11–21, 2001. (pp. 21, 22, 50, 145).

Loeb, N. G.; Wielicki, B. A.; Doelling, D. R.; Smith, G. L.; Keyes, D. F.; Kato, S.; Manalo-Smith, N., and Wong, T. Toward optimal closure of the earth's top-of-atmosphere radiation budget. *J. Climate*, 22(3):748–766, 2009. (p. 2).

Luo, Y.; Zhang, R., and Wang, H. Comparing occurrences and vertical structures of hydrometeors between eastern China and the Indian monsoon region using CloudSat/CALIPSO data. *J. Climate*, 22(4):1052–1064, 2009. (p. 90).

Mace, G. G.; Benson, S., and Kato, S. Cloud radiative forcing at the Atmospheric Radiation Measuremnt Program Climate Research Facility; 2. Vertical redistribution of radiant energy by clouds. *J. Geophys. Res.: Atmospheres (1984-2012)*, 111(16):2591–2610, 2006. (p. 3).

Mace, G. G.; Marchand, R.; Zhang, Q., and Stephens, G. Global hydrometeor occurrence as observed by CloudSat: Initial observations from summer 2006. *Geophys. Res. Lett.*, 34(9), 2007. (p. 91).

Matricardi, M.; Chevallier, F., and Tjemkes, S. An improved general fast radiative transfer model for the assimilation of radiance observations. ECMWF Research Dept. Technical report, Tech. Memo., 345pp., 2001. (p. 26).

McClatchey, R. A.; Fenn, R. W.; Selby, J. E.; Volz, F. E., and Garing, J. S. Optical properties of the atmosphere. Technical report, DTIC Document, 1972. (pp. 36, 55, 57, 94).

Menzel, W. P.; Frey, R. A.; Zhang, H.; Wylie, D. P.; Moeller, C. C.; Holz, R. E.; Maddux, B.; Baum, B. A.; Strabala, K. I., and Gumley, L. E. MODIS global cloud-top pressure and amount estimation: Algorithm description and results. *J. Appl. Meteor. Climatol.*, 47(4):1175–1198, 2008. (p. 91).

Merheim-Kealy, P.; Huot, J. P., and Delwart, S. The MERIS ground segment. *Int. J. Rem. Sens.*, 20(9):1703–1712, 1999. (pp. 32, 79).

METOffice. RTTOV v9, 2014. http://research.metoffice.gov.uk/research/interproj/nwpsaf/rtm/rtm_rttov9.html. (p. 57).

Mie, G. Pioneering mathematical description of scattering by spheres. *Ann. Phys.*, 25:337, 1908. (pp. 20, 37).

Minnis, P.; Liou, K., and Takano, Y. Inference of cirrus cloud properties using satellite-observed visible and infrared radiances. part i: Parameterization of radiance fields. *J. Atmos. Sci.*, 50 (9):1279–1304, 1993. (p. 56).

Minnis, P.; Garber, D. P.; Young, D. F.; Arduini, R. F., and Takano, Y. Parameterizations of reflectance and effective emittance for satellite remote sensing of cloud properties. *J. Atmos. Sci.*, 55(22):3313–3339, 1998. (p. 54).

Minnis, P.; Yost, C. R.; Sun-Mack, S., and Chen, Y. Estimating the top altitude of optically thick ice clouds from thermal infrared satellite observations using CALIPSO data. *Geophys. Res. Lett.*, 35(12), 2008. (p. 77).

Minnis, P.; Sun-Mack, S.; Young, D. F.; Heck, P. W.; Garber, D. P.; Chen, Y.; Spangenberg, D. A.; Arduini, R. F.; Trepte, Q. Z.; Smith, W. L., et al. CERES edition-2 cloud property retrievals using trmm virs and terra and aqua modis data—part i: Algorithms. *IEEE Trans. Geosci. Remote Sens.*, 49(11):4374–4400, 2011. (p. 49).

Mlawer, E. J.; Payne, V. H.; Moncet, J.; Delamere, J. S.; Alvarado, M. J., and Tobin, D. C. Development and recent evaluation of the MT_CKD model of continuum absorption. *Philosophical Transactions of the Royal Society A: Mathematical, Physical and Engineering Sciences*, 370 (1968):2520–2556, 2012. (p. 25).

Moroney, C.; Davies, R., and Muller, J. P. Operational retrieval of cloud-top heights using MISR data. *IEEE Trans. Geosci. Remote Sens.*, 40(7):1532–1540, 2002. (p. 91).

Muller, J. P.; Preusker, R.; Fischer, J.; Zuhlke, M.; Brockmann, C., and Regner, P. ALBEDOMAP: MERIS land surface albedo retrieval using data fusion with MODIS BRDF and its validation using contemporaneous EO and in situ data products. In *Geoscience and Remote Sensing Symposium, 2007. IGARSS 2007. IEEE International*, pages 2404–2407, 2007. (p. 58).

Nakajima, T. and King, M. D. Determination of the optical thickness and effective particle radius of clouds from reflected solar radiation measurements. part i: Theory. *J. Atmos. Sci.*, 47(15):1878–1893, 1990. (pp. 10, 52, 110).

Nakajima, T. Y. and Nakajma, T. Wide-area determination of cloud microphysical properties from noaa avhrr measurements for fire and astex regions. *J. Atmos. Sci.*, 52(23):4043–4059, 1995. (p. 52).

NASA. Modis ceres science team, 2014a. http://ceres.larc.nasa.gov. (p. 48).

NASA. Modis science team, atmosphere, cloud, 2014b. http://modis-atmos.gsfc.nasa.gov/MOD06_L2/index.html. (p. 48).

Sioux FallsNASA Land Processes Distributed Active Archive Center (LP DAAC), South Dakota USA. MODIS/Terra+Aqua Albedo 16-Day L3 Global 0.05Deg CMG, Version 5. [2007-2009], 2014. Online resource: https://lpdaac.usgs.gov/. (p. 58).

Naud, C. M.; Muller, J. P.; Clothiaux, E. E.; Baum, B. A.; Menzel, W. P., et al. Intercomparison of multiple years of MODIS, MISR and radar cloud-top heights. In *Annales Geophysicae*, volume 23, pages 2415–2424, 2005. (p. 91).

Naud, C. M.; Del Genio, A. D.; Bauer, M., and Kovari, W. Cloud vertical distribution across warm and cold fronts in CloudSat-CALIPSO data and a general circulation model. *J. Climate*, 23 (12):3397–3415, 2010. (p. 91).

O'Dell, C. W.; Wentz, F. J., and Bennartz, R. Cloud liquid water path from satellite-based passive microwave observations: A new climatology over the global oceans. *J. Climate*, 21(8): 1721–1739, 2008. (p. 83).

PATMOS-x. Patmos-x, 2014. http://cimss.ssec.wisc.edu/patmosx/overview.html. (p. 48).

Pavolonis, M. J. and Heidinger, A. K. Daytime cloud overlap detection from AVHRR and VIIRS. *J. Appl. Meteorol.*, 43(5):762–778, 2004. (p. 99).

Pawlowska, H. and Brenguier, J. Microphysical properties of stratocumulus clouds during ACE-2. *Tellus B*, 52(2):868–887, 2000. (p. 75).

Petty, G. W. *A first course in atmospheric radiation*. Sundog Pub, 2006. (pp. 14, 17, 25).

Pincus, R. and Baker, M. B. Effect of precipitation on the albedo susceptibility of clouds in the marine boundary layer. *Nature*, 372(6503):250–252, 1994. (p. 5).

Plass, G. N.; Kattawar, G. W., and Catchings, F. E. Matrix operator theory of radiative transfer. 1: Rayleigh scattering. *Appl. Opt.*, 12(2):314–329, 1973. (p. 23).

Polonsky, I. N.; Labonnote, L. C., and Cooper, S. Level 2 cloud optical depth product process description and interface control document. *CloudSat Project, NASA Earth System Science Pathfinder Mission*, 2008. (pp. 35, 95).

Potter, G. L. and Cess, R. D. Testing the impact of clouds on the radiation budgets of 19 atmospheric general circulation models. *J. Geophys. Res.: Atmospheres (1984–2012)*, 109(D2), 2004. (p. 6).

Preusker, R. and Lindstrot, R. Remote sensing of cloud-top pressure using moderately resolved measurements within the oxygen A band-a sensitivity study. *J. Appl. Meteor. Climatol.*, 48 (8):1562–1574, 2009. (pp. 34, 40, 40, 57, 92).

Pruppacher, H. R. and Klett, J. D. *Microphysics of Clouds and Precipitation, 2nd rev*. Kluwer Academic Publishers, 1997. (p. 55).

Ramanathan, V.; Cess, R. D.; Harrison, E. F.; Minnis, P.; Barkstrom, B. R.; Ahmad, E., and Hartmann, D. Cloud-radiative forcing and climate: Results from the Earth Radiation Budget Experiment. *Science*, 243(4887):57–63, 1989. (p. 2).

Randall, D.; Khairoutdinov, M.; Arakawa, A., and Grabowski, W. Breaking the cloud parameterization deadlock. *Bull. Amer. Meteor. Soc.*, 84(11):1547–1564, 2003. (p. 5).

Rasool, S. I. Cloud heights and nighttime cloud cover from TIROS radiation data. *J. Atmos. Sci.*, 21(2):152–156, 1964. (p. 7).

Rast, M.; Bezy, J. L., and Bruzzi, S. The ESA medium resolution imaging spectrometer meris a review of the instrument and its mission. *Int. J. Rem. Sens.*, 20(9):1681–1702, 1999. (pp. 21, 22, 50, 145).

Rodgers, C. D. *Inverse methods for atmospheric sounding: Theory and Practice, Series on Atmospheric, Oceanic and Planetary Physics–Vol. 2*. 2000. (pp. 28, 29, 61).

Roebeling, R.; Baum, B.; Bennartz, R.; Hamann, U.; Heidinger, A.; Thoss, A., and Walther, A. Evaluating and improving cloud parameter retrievals. *Bull. Amer. Meteor. Soc.,* 94(4): ES41–ES44, 2013. (p. 49).

Roebeling, R. A.; Feijt, A. J., and Stammes, P. Cloud property retrievals for climate monitoring: Implications of differences between spinning enhanced visible and infrared imager (seviri) on meteosat-8 and advanced very high resolution radiometer (avhrr) on noaa-17. *J. Geophys. Res.: Atmospheres (1984–2012)*, 111(D20), 2006. (pp. 49, 52).

Rossow, W. B. and Schiffer, R. A. ISCCP cloud data products. *Bull. Amer. Meteor. Soc.*, 72(1): 2–20, 1991. (p. 8, 8).

Rossow, W. B. and Schiffer, R. A. Advances in understanding clouds from ISCCP. *Bull. Amer. Meteor. Soc.*, 80(11):2261–2287, 1999. (pp. 36, 36, 92, 95, 140).

Rothman, L. S.; Gordon, I. E.; Barbe, A.; Benner, D. C.; Bernath, P. F.; Birk, M.; Boudon, V.; Brown, L. R.; Campargue, A.; Champion, J.P., et al. The hitran 2008 molecular spectroscopic database. *J. Quant. Spectrosc. Radiat. Transf.*, 110(9):533–572, 2009. (pp. 25, 57, 95).

Rothman, L. S.; Gordon, I. E.; Babikov, Y.; Barbe, A.; Benner, D. C.; Bernath, P. F.; Birk, M.; Bizzocchi, L.; Boudon, V.; Brown, L. R., et al. The HITRAN2012 molecular spectroscopic database. *J. Quant. Spectrosc. Radiat. Transf.*, 130:4–50, 2013. (p. 25).

Rozanov, V. V. and Kokhanovsky, A. A. Semianalytical cloud retrieval algorithm as applied to the cloud top altitude and the cloud geometrical thickness determination from top-of-atmosphere reflectance measurements in the oxygen A band. *J. Geophys. Res.: Atmospheres (1984–2012)*, 109(D5), 2004. (p. 92, 92).

Saiedy, F.; Hilleary, D. T., and Morgan, W. A. Cloud-top altitude measurements from satellites. *Appl. Opt.*, 4(4):495–500, 1965. (pp. 32, 34).

Saiedy, F.; Jacobowitz, H., and Wark, D. Q. On cloud-top determination from Gemini-5. *J. Atmos. Sci.*, 24(1):63–69, 1967. (pp. 32, 92).

Sassen, K.; Wang, Z., and Liu, D. Global distribution of cirrus clouds from CloudSat/Cloud-Aerosol lidar and infrared pathfinder satellite observations (CALIPSO) measurements. *J. Geophys. Res.: Atmospheres (1984–2012)*, 113(D8), 2008. (p. 91).

Saunders, R.; Matricardi, M., and Geer, A. RTTOV-9 Users Guide, NWP SAF Rep. NWPSAF-MO-UD-016. User guide, Met Office, 2010. (p. 57).

Saunders, R. W. and Kriebel, K. T. An improved method for detecting clear sky and cloudy radiances from avhrr data. *Int. J. Rem. Sens.*, 9(1):123–150, 1988. (p. 55).

Sayer, A. M.; Poulsen, C. A.; Arnold, C.; Campmany, E.; Dean, S.; Ewen, G. B. L.; Grainger, R. G.; Lawrence, B. N.; Siddans, R.; Thomas, G. E., and Watts, P. D. Global retrieval of ATSR cloud parameters and evaluation (GRAPE): dataset assessment. *Atmos. Chem. Phys.*, 11(8): 3913–3936, 2011. URL http://www.atmos-chem-phys.net/11/3913/2011/. (pp. 29, 48).

Schmetz, J.; Pili, P.; Tjemkes, S.; Just, D.; Kerkmann, J.; Rota, S., and Ratier, A. An introduction to meteosat second generation (MSG). *Bull. Amer. Meteor. Soc.*, 83(7):977–992, 2002. (p. 8).

Seemann, S. W.; Borbas, E. E.; Knuteson, R. O.; Stephenson, G. R., and Huang, H. Development of a global infrared land surface emissivity database for application to clear sky sounding retrievals from multispectral satellite radiance measurements. *J. Appl. Meteor. Climatol.*, 47(1):108–123, 2008. (p. 58).

Seethala, C. and Horváth, Á. Global assessment of AMSR-E and MODIS cloud liquid water path retrievals in warm oceanic clouds. *J. Geophys. Res.: Atmospheres (1984–2012)*, 115(D13), 2010. (pp. 84, 85).

Sherwood, S. C.; Chae, J.; Minnis, P., and McGill, M. Underestimation of deep convective cloud tops by thermal imagery. *Geophys. Res. Lett.*, 31(11), 2004. (pp. 77, 98).

Smith, D. Empirical nonlinearity correction for 12um channel. Technical report, RAL Space AATSR Technical note, Doc No: PO-TN-RAL-AT-0562, Issue: 1.1, 2014. (p. 99).

Smith, D.L.; Poulsen, C.A., and Latter, B. Calibration status of the aatsr reflectance channels. In *Proceedings of the MERIS/AATSR Workshop*, 2008. (p. 51).

Stephens, G. L. Cloud feedbacks in the climate system: A critical review. *J. Climate*, 18(2): 237–273, 2005. (p. 6).

Stephens, G. L.; Vane, D. G.; Boain, R. J.; Mace, G. G.; Sassen, K.; Wang, Z.; Illingworth, A. J.; O'Connor, E. J.; Rossow, W. B.; Durden, S. L., et al. The CloudSat mission and the A-Train: A new dimension of space-based observations of clouds and precipitation. *Bull. Amer. Meteor. Soc.*, 83(12):1771–1790, 2002. (pp. 9, 91).

Stubenrauch, C. J.; Rossow, W. B.; Kinne, S.; Ackerman, S.; Cesana, G.; Chepfer, H., and Di, L. Assessment of global cloud datasets from satellites. *A Project of the World Climate Research Programme Global Energy and Water Cycle Experiment (GEWEX) Radiation Panel*, 2012. (p. 1).

Stubenrauch, C. J.; Rossow, W. B.; Kinne, S.; Ackerman, S.; Cesana, G.; Chepfer, H.; Di Girolamo, L.; Getzewich, B.; Guignard, A.; Heidinger, A., et al. Assessment of global cloud datasets from satellites: Project and database initiated by the gewex radiation panel. *Bull. Amer. Meteor. Soc.*, 94(7):1031–1049, 2013. (p. 48, 48).

Twomey, S. The influence of pollution on the shortwave albedo of clouds. *J. Atmos. Sci.*, 34 (7):1149–1152, 1977. (p. 5).

Van de Hulst, H. C. Multiple light scattering. *Multiple light scattering. New York, NY (USA): Academic Press, 739 p.*, 1, 1980. (p. 23).

Vanbauce, C.; Buriez, J.; Parol, F.; Bonnel, B.; Seze, G., and Couvert, P. Apparent pressure derived from ADEOS-POLDER observations in the oxygen A-band over ocean. *Geophys. Res. Lett.*, 25(16):3159–3162, 1998. (pp. 33, 92).

Vanbauce, C.; Cadet, B., and Marchand, R. T. Comparison of POLDER apparent and corrected oxygen pressure to ARM/MMCR cloud boundary pressures. *Geophys. Res. Lett.*, 30(5), 2003. (pp. 33, 93).

124

Walther, A. and Heidinger, A. K. Implementation of the daytime cloud optical and microphysical properties algorithm (DCOMP) in PATMOS-x. *J. Appl. Meteor. Climatol.*, 51(7):1371–1390, 2012. (pp. 10, 49, 51, 52).

Wang, J. and Rossow, W. B. Effects of cloud vertical structure on atmospheric circulation in the GISS GCM. *J. Climate*, 11(11):3010–3029, 1998. (p. 90).

Wang, M. and King, M. D. Correction of rayleigh scattering effects in cloud optical thickness retrievals. *J. Geophys. Res.*, 102(D22):25915–25, 1997. (p. 53, 53).

Wang, P.; Stammes, P.; Pinardi, G.; Roozendael, M. van, et al. FRESCO+: an improved O2 A-band cloud retrieval algorithm for tropospheric trace gas retrievals. *Atmos. Chem. Phys.*, 8(21):6565–6576, 2008. (p. 92).

Webb, M.; Senior, C.; Bony, S., and Morcrette, J. Combining ERBE and ISCCP data to assess clouds in the Hadley Centre, ECMWF and LMD atmospheric climate models. *Clim. Dynam.*, 17(12):905–922, 2001. (p. 7).

Weisz, E.; Li, J.; Menzel, W. P.; Heidinger, A. K.; Kahn, B. H., and Liu, C. Comparison of AIRS, MODIS, CloudSat and CALIPSO cloud top height retrievals. *Geophys. Res. Lett.*, 34(17), 2007. (p. 91).

Wielicki, B. A.; Barkstrom, B. R.; Harrison, E. F.; Lee III, R. B.; Louis Smith, G., and Cooper, J. E. Clouds and the earth's radiant energy system (CERES): An earth observing system experiment. *Bull. Amer. Meteor. Soc.*, 77(5):853–868, 1996. (p. 1).

Winker, D. M.; Pelon, J. R., and McCormick, M. P. The CALIPSO mission: Spaceborne lidar for observation of aerosols and clouds. In *Third International Asia-Pacific Environmental Remote Sensing Remote Sensing of the Atmosphere, Ocean, Environment, and Space*, pages 1–11. International Society for Optics and Photonics, 2003. (pp. 10, 91).

Wiscombe, W. J. Improved mie scattering algorithms. *Appl. Opt.*, 19(9):1505–1509, 1980. (pp. 20, 37, 54, 95).

Wu, D. L.; Ackerman, S. A.; Davies, R.; Diner, D. J.; Garay, M. J.; Kahn, B. H.; Maddux, B. C.; Moroney, C. M.; Stephens, G. L.; Veefkind, J. P., et al. Vertical distributions and relationships of cloud occurrence frequency as observed by MISR, AIRS, MODIS, OMI, CALIPSO, and CloudSat. *Geophys. Res. Lett.*, 36(9), 2009. (p. 91).

Wu, M. C. Remote sensing of cloud-top pressure using reflected solar radiation in the oxygen A-band. *J. Climate and applied meteorology*, 24(6):539–546, 1985. (p. 34).

Yamamoto, G. and Wark, D. Q. Discussion of the letter by RA Hanel,"Determination of cloud altitude from a satellite". *J. Geophys. Res.*, 66(10):3596–3596, 1961. (pp. 32, 91).

Yin, W. and Zhai, W. Observational characteristics of cloud vertical profiles over the continent of East Asia from the CloudSat data. *Acta Meteorologica Sinica*, 27(1):26–39, 2013. (p. 90).

Yuan, J.; Houze Jr, R. A., and Heymsfield, A. J. Vertical structures of anvil clouds of tropical mesoscale convective systems observed by CloudSat. *J. Atmos. Sci.*, 68(8):1653–1674, 2011. (p. 90).

Zelinka, M. D. and Hartmann, D. L. Why is longwave cloud feedback positive? *J. Geophys. Res.: Atmospheres (1984–2012)*, 115(D16), 2010. (p. 4).

Zhang, Z.; Ackerman, A. S.; Feingold, G.; Platnick, S.; Pincus, R., and Xue, H. Effects of cloud horizontal inhomogeneity and drizzle on remote sensing of cloud droplet effective radius: Case studies based on large-eddy simulations. *J. Geophys. Res.: Atmospheres (1984–2012)*, 117(D19), 2012. (p. 75).

Summary

Clouds interact with solar and thermal radiation and affect the Earth's energy budget. The interaction between clouds and radiation occurs differently for different cloud types. They also play a major role in the hydrological cycle. Inadequate representations of cloud processes and cloud-climate interactions in climate models form the largest uncertainty in climate change projections. Remote sensing of cloud properties using satellite observations offers the potential for monitoring climate change on a global scale, the evaluation of climate models and improving climate projections.

In this work a set of cloud properties is retrieved from satellite observations on a global scale and for multi-annual time series. The synergy of two multi-spectral imaging radiometers onboard the polar-orbiting satellite Envisat is exploited to retrieve the following macro-physical, optical and micro-physical cloud properties:

- cloud cover

- cloud thermodynamic phase

- cloud optical thickness

- cloud effective radius

- cloud water path

- cloud top temperature

- cloud top pressure

- cloud top height

The synergistic approach allows for an improved characterization of clouds and comprises the collocation of AATSR and MERIS measurements and the

use of the combined spectral information from both instruments for cloud detection and subsequent cloud property retrievals. The pixel-based daytime FAME-C algorithm as well as the evaluation of its outcome for selected regions and years is presented. Radiative transfer simulations performed with the radiative transfer model MOMO serve as a basis for the forward models. Optimal estimation is used as the inversion method, which provides uncertainty estimates for each cloud property on a pixel basis.

Of particular interest in this work is the MERIS cloud top pressure retrieval using MERIS measurements in the oxygen-A absorption band. It provides an additional independent source of information on cloud height next to the cloud top temperature. It was shown that MERIS-CTP retrieval depends on the assumed vertical extinction profile of the cloud, while AATSR-CTT is less affected. For several cloud types, based on a combination of cloud optical thickness and cloud top pressure, inhomogeneous vertical extinction profiles were derived from combined CloudSat CPR and MODIS data and used in the retrievals. The difference in sensitivity of both independent cloud height retrievals to cloud vertical extinction profile was exploited to analyze the relationship between difference in retrieved cloud heights and cloud vertical extent. This additional parameter can be used to further characterize cloudy scenes.

To assess the performance of the newly developed algorithm, the processed FAME-C dataset was compared to well-established datasets from ground-based observations as well as satellites datasets. The evaluation was performed using datasets from both passive and active instruments and for selected regions on a pixel-basis as well as spatially gridded and temporally averaged data sets on a global scale. For the pixel-based optical and micro-physical cloud property retrievals, best agreements were found for marine Stratocumulus regions. As anticipated from previous sensitivity studies, the performance of MERIS-CTH is better for low-level clouds, while it is better for high level clouds for AATSR-CTH. First indications were found for the influence of aerosol layers on the cloud property retrievals in a particular marine Stratocumulus region. On a global scale and for a temporal average, spatial patterns of the cloud properties generally look very similar. In the polar regions, differences can become very large.

This work has shown that the synergistic use of AATSR and MERIS measurements is suitable for the retrieval of a set of cloud properties on a global scale. Through several evaluation exercises, the strengths and weaknesses of the retrievals under varying conditions were identified. An improved cloud property retrieval is expected from, amongst others, an improved cloud phase detection and more accurate auxiliary data. In addition,

this work will contribute to successfully exploiting the synergistic measurements of SLSTR and OLCI onboard Sentinel-3, and to be launched in 2015, for the purpose of cloud-climate studies, since the FAME-C algorithm can be easily adapted to the synergy of these measurements.

Zusammenfassung

Durch die Wechselwirkung von Wolken mit solarer und thermischer Strahlung, haben diese einen erheblichen Einfluss auf die Strahlungsbilanz der Erde. Die Wechselwirkung zwischen Wolken und Strahlung passiert auf unterschiedliche Weise für verschiedene Wolkentypen. Des Weiteren spielen sie eine wichtige Rolle im hydrologischen Zyklus. Die unzureichende Darstellung von Wolkenprozessen und Wechselwirkungen zwischen Wolken und Klima in Klimamodellen bilden den größten Unsicherheitsfaktor in Klimaprognosen. Die Satellitenfernerkundung von Wolkeneigenschaften bietet das Potenzial für die Überwachung des Klimawandels, der Validierung von Klimamodellen und von verbesserten Klimaprognosen.

In dieser Arbeit wird eine Reihe von Wolkenparametern aus satellitengestützten Beobachtungen in einem globalen Umfang und für mehrjährige Zeitreihen abgeleitet. Die Synergie der zwei abbildenden Multispektral-Radiometern AATSR und MERIS auf dem polarumlaufenden Satelliten Envisat wurde genutzt, um die folgenden mikro- und makrophysikalischen und optischen Wolkenparameter abzuleiten:

- Wolkenbedeckungsgrad

- Thermodynamische Wolkenphase

- Optische Dicke der Wolke

- Effektiver Radius der Wolkentröpfchen

- Integriertes Flüssigwassergehalt

- Temperatur der Wolkenoberkannte

- Druck der Wolkenoberkannte

- Höhe der Wolkenoberkannte

Der synergistische Ansatz bietet die Möglichkeit für eine verbesserte Beschreibung von Wolkeneigenschaften gegenüber der Anwendung eines einzelnen Sensors durch die Verwendung der spektralen Information beider Instrumente. Er besteht aus der Kollokation der AATSR und MERIS Messungen und der Ableitung der Wolkeneigenschaften. Der pixelbasierte, tageszeitliche FAME-C Algorithmus und seine Auswertung für ausgewählte Regionen und Jahre wurde vorgestellt. Strahlungstransportsimulationen wurden mit dem Strahlungstransportmodel MOMO durchgeführt und dienen als Basis für die Vorwärtsmodellierung. Die sogenannte Optimal-Estimation-Methode dient als Inversionsmethode und liefert eine Abschätzung der Unsicherheit für jeden Wolkenparameter auf Pixelbasis.

Von besonderem Interesse in dieser Arbeit ist die Ableitung des Wolkenoberkantendrucks mithilfe der MERIS-Messungen in der Sauerstoff-Absorptionsbande. Er bietet eine zusätzliche unabhängige Informationsquelle für die Wolkenhöhe neben der Ableitung der Wolkenoberkantentemperatur. Es wurde gezeigt, dass der abgeleitete MERIS Wolkenoberkantendruck vom angenommenen vertikal Extinktionsprofil der Wolke abhängt, während die abgeleitete AATSR Wolkenoberkantentemperatur weniger davon betroffen ist. Für mehrere Wolkentypen, basierend auf einer Kombination der optischen Dicke der Wolke und Wolkenoberkantendruck, wurden inhomogene vertikale Extinktionsprofile aus kombinierten Daten von CloudSat CPR und MODIS abgeleitet und auf die Ableitungen angewendet. Die Differenz der Sensitivität der beiden unabhängigen Wolkenhöhenableitungen zum vertikalen Extinktionsprofil der Wolke wurde genutzt, um die Beziehung der Differenz zwischen den beiden Wolkenhöhenparametern zum vertikalen Ausmaß der Wolke auszuwerten. Dieser zusätzliche Parameter kann für eine erweiterte Charakterisierung einer Wolkenszene verwendet werden.

Um die Leistungsfähigkeit des neu entwickelten Algorithmus abzuschätzen, wurde der erzeugte FAME-C Datensatz mit etablierten Datensätzen verglichen, welche sowohl aus bodengestützten als auch aus satellitengestützten Beobachtungen hervorgegangen sind. Die Auswertung wurde für ausgewählte Regionen auf Pixelbasis sowie für einen zeitlich gemittelten globalen Datensatz durchgeführt, der auf ein reguläres Gitter gebracht wurde, erzeugt aus Beobachtung von passiven und aktiven Instrumenten. Für pixelbasierte optische und mikrophysikalische Wolkenparameter wurde die beste Übereinstimmung für eine marine Region mit Stratokumuluswolken gefunden. Wie aus vorherigen Studien erwartet, schneidet der MERIS Wolkenoberkantendruck besser für niedrige Wolken ab, während die AATSR Wolkenoberkantentemperatur besser für höhere Wolken abschneidet. Es wurden erste Hinweise für einen Einfluss von

Aerosolschichten auf die abgeleiteten optischen und mikro-physikalischen Wolkenparameter in einer bestimmten marinen Stratokumulusregion gefunden. Im globalen Umfang und für zeitlich gemittelte Wolkenparameter sehen räumliche Muster der Wolkenparameter im Allgemeinen sehr ähnlich aus. In den Polarregionen können die Unterschiede sehr groß sein.

Diese Arbeit zeigt, dass die synergistische Nutzung der AATSR- und MERIS-Messungen für die Ableitung einer Reihe von Wolkenparameter im globalen Umfang geeignet ist. Durch Mittel von Auswertungen mithilfe von verschiedenen etablierten Datensätzen wurden die Stärken und Schwächen der Ableitungen unter verschiedenen Bedingungen festgestellt. Eine verbesserte Ableitung der Wolkenparameter kann wegen, unter anderem, einer verbesserten Bestimmung der Wolkenphase und genauerer Hilfsdatensätze erwartet werden. Des Weiteren trägt diese Arbeit zu einer erfolgreichen Ausnutzung der synergistischen Messungen von SLSTR und OLCI auf dem Sentinel-3 Satellit bei, welcher 2015 starten soll. Wolken-Klima Studien können dann, durch eine einfache Anpassung des FAME-C Algorithmus auf diese Messungen fortgesetzt werden.

Abbreviations and acronyms

AATSR	Advanced Along Track Scanning Radiometer
ARM	Atmospheric Radiation Measurement
BT	Brightness Temperature
CC	Cloud Cover
CCI	Climate Change Initiative
CCT	Cloud Top Temperature
CF	Cloud Fraction
CGT	Cloud Geometrical Thickness
CPR	Cloud Profiling Radar
CM	Cloud Mask
COT	Cloud Optical Thickness
CPH	Cloud Thermodynamic Phase
CTP	Cloud Pressure Thickness
CVE	Cloud Vertical Extent
CWC	Cloud Water Content
CWP	Cloud Water Path
CWVL	Central Wavelength
DCHP	Daytime Cloud Height Properties

DCOMP	Daytime Cloud Optical and Micro-physical Properties
Envisat	Environmental Satellite
ESA	European Space Agency
FAME-C	Freie Universität Berlin AATSR MERIS Cloud
HOM	Homogeneous
ISCCP	International Satellite Cloud Climatology Project
IPCC	Intergovernmental Panel on Climate Change
IR	Infrared
IWC	Ice Water Content
IWP	Ice Water Path
LUT	Look-Up Table
LWC	Liquid Water Content
LWP	Liquid Water Path
MERIS	Medium Resolution Imaging Spectrometer
MODIS	Moderate Resolution Imaging Spectroradiometer
MOMO	Matrix Operator Model
MWR	Microwave Radiometer
NIR	Near-Infrared
NWP	Numerical Weather Prediction
OLCI	Ocean and Land Colour Instrument
POLDER	Polarization and Directionality of the Earth's Reflectances
REFF	Effective Radius
RAA	Relative Azimuth Angle
RMSD	Root Mean Square Deviation

RTM   Radiative Transfer Model

RTTOV   Radiative Transfer for TOVS

SLSTR   Sea and Land Surface Temperature Radiometer

SVA   Satellite Zenith Angle

SZA   Solar Zenith Angle

TIR   Thermal Infrared

TOA   Top Of Atmosphere

VIS   Visible

List of Figures

List of Tables

146

Curriculum Vitae

For reasons of data protection, the curriculum vitae is not included in the online version.

Publications

First author

Carbajal Henken, C. K., M. J. Schmeits, H. Deneke, and R. A. Roebeling. 2011, Using MSG-SEVIRI cloud physical properties and weather radar observations for the detection of Cb/TCu clouds, *J. of App. Met. and Clim.*, 50 (7), 1587-1600

Henken, C. C., R. Lindstrot, F. Filipitsch, A. Walther, R. Preusker, and J. Fischer. 2013, FAME-C: Retrieval of cloud top pressure with vertically inhomogeneous cloud profiles, *AIP Conference Proceedings*,1531, 412-415

Carbajal Henken, C. K., R. Lindstrot, R. Preusker, J. Fischer. 2014, FAME-C: cloud property retrieval using synergistic AATSR and MERIS observations, *Atmos. Meas. Tech.*, 7 (11), 3873-3890, doi:10.1117/12.465995

Carbajal Henken, C. K., L. Doppler, R. Lindstrot, R. Preusker, J. Fischer. 2014, Exploiting the sensitivity of two satellite cloud height retrievals to cloud vertical distribution, *Atmos. Meas. Tech. Discuss.*, 8 (3), 2623-2655, doi:10.5194/amtd-8-2623-2015

Co-author

Doppler, L., C. Carbajal Henken, J. Pelon, F. Ravetta and J. Fischer. 2014, Extension of radiative transfer code MOMO, matrix-operator model to the thermal infrared–Clear air validation by comparison to RTTOV and application to CALIPSO-IIR, *JQSRT*, 144, 49-67

Hollstein, A., J. Fischer, C. Carbajal Henken, R. Preusker. 2014, Bayesian cloud detection for MERIS, AATSR, and their combination, *Atmos. Meas. Tech. Diss.*, 7, 11045-11085

Danksagung/Dankwoord

Als erstes möchte ich Prof. Dr. Jürgen Fischer herzlich danken für die Möglichkeit, die Promotion an dem Institut für Weltraumwissenschaften zu machen und für die angenehme Zusammenarbeit. Prof. Dr. Ralf Bennartz danke ich herzlich für die Übernahme des Zweitgutachtens und für die Möglichkeit, mehrere Wochen in seiner Gruppe an der University of Wisconsin zu verbringen.

Ich möchte alle (alt-) Kollegen danken für eine angenehme Arbeitsatmosphäre am WeW und nette Aktivitäten außerhalb der Arbeitszeit. Jenny, es hat mich gefreut dich als Zimmerkameradin gehabt zu haben. Jonas, zum Glück bist du auch öfter mal bis spät im Büro. Rasmus, Rene, Lionel, Andre, Hannes und Florian danke ich für die gute Zusammenarbeit in Rahmen von Projekten und Publikationen. Im Laufe meiner Zeit am WeW sind so einige Kollegen gegangen (insbesondere zum DWD oder GFZ) und bin ich innerhalb von 4,5 Jahren vom Newbie zum Alteingesessen verwandelt. Ich freue mich aber sehr wenn wir uns treffen bei Projekttreffen, Konferenzen oder auch bei anderen Gelegenheiten. Vielen Dank an die Kollegen, die Teile meiner Arbeit gelesen und korrigiert haben.

I would like to thank the colleagues from the ESA Cloud CCI project and the HD(CP)^2 project for fruitful cooperations.

Aan Rob Roebeling heb ik het te danken dat ik in het vakgebied van de Satellietenmeteorologie terecht ben gekomen en erin ben blijven hangen. Door zijn enthousiasme en de collegiale sfeer en goede samenwerking op het KNMI, niet in het minst ook te danken aan Maurice, Erwin en Niels, kon ik mij een verdere loopbaan aan een onderzoeksinstituut goed voorstellen.

Lieve vrienden, ik heb een erg leuke en gezellige schooltijd en studententijd gehad en ben jullie daar dankbaar voor. Ook al zien wij elkaar soms minder vaak dan we zouden willen, als we samen zijn voelt het als vanouds. Een bijzondere plek in mijn hart hebben alle reizen die we samen gemaakt hebben. Om een paar te noemen; Europa Interrail na het schoolexamen

met Saskia en Saskia; Swansea met David, Saskia, Saskia, en Chantal; Een studiereis naar Boedapest waar Luc en ik de enigen waren die niet in deze studie zaten; Een Amerikaanse roadtrip met Ward, Jan, Tim en Hans; Europa Interrail met Tim, Ward en Hans; en nog heel recent onze Noorderlicht-poolexpeditie in Tromsö met Ward en Anna-Carolina. Ik ben blij dat velen van jullie met enige regelmaat mij en Hans komen opzoeken in Berlijn. Tim, opnieuw heel erg bedankt voor je TₑX-hulp.

Liebe Berliner Freunde, ich freue mich sehr die schönen Dinge, welche die Stadt Berlin zu bieten hat, mit euch zu erleben. Auch haben wir schon einige tolle Reisen zusammen gemacht, wie die schönen Tagen in La Provence mit Katrin und Antoine und unsere abenteuerliche Mexikoreise mit Nicole und Oscar dazu.

Ik ben mijn familie heel dankbaar voor jullie onvoorwaardelijke vertrouwen in mij en dat ik altijd bij jullie terecht kan. Ik ben blij dat we regelmatig bellen of skypen, zodat, ook al wonen we in verschillende steden, landen en zelfs continenten, we van elkaars leven goed op de hoogte zijn. Lieve mam, ik ben jou dankbaar voor al je ondersteuning en interesse in mijn opleiding en werk door de jaren heen. Lieber papa, mein Interesse für die Wissenschaft habe ich dir zu danken und ich freue mich über eine baldige Zusammenarbeit. Ich habe auch schon wieder Lust auf eine Reise nach Mexiko. Lieve Kerstin, ik ben trots op jouw doorzettingsvermogen. Dankzij opa en oma hebben we vele leuke familiebijeenkomsten gehad, ik hoop dat ondanks dat ze er niet meer zijn, we nog weleens vaker allemaal bij elkaar komen. Ik geniet erg van het samenzijn met familie in Zoetermeer en Groningen tijdens de kerstvakantie en in het bijzonder dit jaar, na het inleveren van de eerste versie van mijn thesis, heeft het mij goed gedaan.

Lieve Hans, dankjewel voor al je liefde en steun. Als ik aan het stressen ben blijf jij rustig en zorgt er zo voor dat het natuurlijk allemaal goed komt. Heel soms is het andersom. Wij hebben in onze twaalf jaar samen al heel wat meegemaakt en ik kan niet wachten op de avonturen die nog gaan komen.